

Stress and Structure Evolution during Cu/Au(111) - $(22 \times \sqrt{3})$ Heteroepitaxy:

An *In-Situ* Study with UHV-STM

(Ultra High Vacuum Scanning Tunneling Microscopy)

by

Jungwoo Nah

A Dissertation Presented in Partial Fulfillment
of the Requirements for the Degree
Doctor of Philosophy

Approved February 2012 by the
Graduate Supervisory Committee:

Cody Friesen, Chair
Peter Bennett
Karl Sieradzki

ARIZONA STATE UNIVERSITY

May 2012

ABSTRACT

This research focuses on the stress and structure evolution observed *in-situ* during the earliest stages of thin film growth in Cu/Au(111)-($22 \times \sqrt{3}$) system. For the research, an ultra high vacuum-scanning tunneling microscopy (UHV-STM) system was modified to have the additional capabilities of *in-situ* deposition and *in-situ* stress evolution monitoring. The design and fabrication processes for the modifications are explained in detail. The deposition source enabled imaging during the deposition of Cu thin films, while also being columnar enough to avoid negatively impacting the function of the microscope. It was found that the stress-induced changes in piezo voltage occurred over a substantially longer time scale and larger piezo scale than used during imaging, allowing for the deconvolution of the two sources of piezo voltage change.

The intrinsic stress evolution observed at the onset of Cu growth was tensile in character and reached a maximum of 0.19 N/m at approximately 0.8ML, with an average tensile slope of 1.0GPa. As the film thickness increased beyond 0.8 ML, the stress became less tensile as the observation of disordered stripe and trigon patterns of misfit dislocations began to appear. The transport of atoms from the surface of enlarged Cu islands into the strained layer played an important role in this stage, because they effectively reduce the activation barrier for the formation of the observed surface structures. A rich array of structures were observed in the work presented here including stripe, disordered stripe and trigon patterns co-existing in a single Cu layer. Heteroepitaxial systems in existing literature showed a uniform structure in the single layer. The non-uniform

structures in the single layer of this work may be attributed to the room temperature Cu growth, which can kinetically limit uniform pattern formation. The development of the UHV-STM system with additional capabilities for this work is expected to contribute to research for the stress and structure relationships of many other heteroepitaxial systems.

ACKNOWLEDGMENTS

I would like to give my sincere thanks to my advisor, Professor Friesen. He has provided me with his scientific insight and encouragement with which I could continuously work research goals and success. Moreover, his optimism and enthusiasm served as the foundation for my motivation and patience to build up experimental systems and complete my research assignments. I am grateful for Professor Sieradzki as he gave me valuable suggestions that guided me to find a proper path for research, and provided important equipment that was crucial to my research project. I would like to express my gratitude to Professor Bennett, who provided significant experimental viewpoints and generously allowed me to use his lab facilities. I want to thank Friesen Research Group members who supplied a creative and thorough work environment. Also, I appreciate Susan Baldi's warm and friendly support.

I acknowledge the National Science Foundation career award (DMR-0543666) for Professor Friesen that has funded this work.

From the bottom of my heart I thank my lovely wife, Chanmi, who has endured every difficult step with me. My life has been more joyful and valuable since we were married. Chanmi, you are my love and the best! I thank my cuties, Suah and Yeonah, who are my joy. I thank my parents and parents in law. It is impossible to forget their love, prayers support and encouragement.

I give thanks to Pastor Yoo and Pastor Bob, who mentored me while I was discouraged. I would like to thank my friend, Dr. Han, who has shared good and

bad moments as well as Korean food with me. I deeply appreciate the great amount of prayers from Pastor Park, Pastor Song, Pastor Woo, my friendly neighbor Joseph's family, and church members.

Lastly, I give thanks to my father God, the creator of all things, who is in control.

TABLE OF CONTENTS

	Page
LIST OF TABLES.....	viii
LIST OF FIGURES.....	ix
CHAPTER	
1 INTRODUCTION.....	1
Section 1.1 Stress and Structure in Heteroepitaxial Systems.....	1
Section 1.2 Synopsis.....	4
2 SURFACE STRUCTURES.....	7
Section 2.1 Surface Reconstruction	10
Section 2.2 Growth Kinetics for Surface Structure Formation	16
Section 2.3 Surface Structures Formed by Strain Relaxation in Ultra Thin Metal Films.....	18
Section 2.3.1 Cu/Ru(0001).....	19
Section 2.3.2 Ag/Ru(0001).....	21
Section 2.3.3 Ag/Pt(111).....	25
Section 2.3.4 Cu/Au(111).....	27
3 SURFACE AND INTERFACE.....	30
Section 3.1 Surface Free Energy and Surface Stress.....	30
Section 3.2 Interfacial Free Energy and Interface Stress	31
Section 3.3 Stress in Ultrathin Films Associated with Misfit Strain.....	33

CHAPTER	Page	
4	SCANNING TUNNELING MICROSCOPY FOR STRESS MEASUREMENTS	35
	Section 4.1 Scanning Tunneling Microscopy (STM).....	35
	Section 4.1.1 Tunneling Current	36
	Section 4.1.2 STM Topography	41
	Section 4.2 Deflection of Cantilever	42
	Section 4.3 Stress Measurements by STM	45
5	EXPERIMENTAL PROCEDURE.....	47
	Section 5.1 Equipment Setup	47
	Section 5.1.1 Heating Element	47
	Section 5.1.2 Design for the Small Deposition Source	48
	Section 5.1.3 STM System (RHK Technology)	52
	Section 5.1.4 UHV Chambers	54
	Section 5.2 Experimental Details	56
	Section 5.2.1 Tip Preparation	56
	Section 5.2.2 Sample Preparation	58
	Section 5.2.2.1 Au on SiN Membrane.....	58
	Section 5.2.2.2 Au on Glass Cantilever.....	59
	Section 5.2.2.3 Au on Mica Cantilever	59
	Section 5.2.3 STM Imaging.....	60
	Section 5.2.4 <i>In-Situ</i> Cu Deposition.....	62
	Section 5.2.5 Stress Measurements	65

CHAPTER	Page
Section 5.2.6 Verification of <i>In-Situ</i> Cu Deposition for STM Imaging and Stress Measurements.....	66
Section 5.2.7 Problems with SiN Membrane Substrates....	69
Section 5.2.8 Thermal Effects	73
Section 5.2.9 Validity of the Glass Cantilever for Stress Measurements	76
Section 5.2.10 Resonance Frequency of Mica Cantilever...	78
6 RESULTS AND DISCUSSION.....	82
Section 6.1 Surface Structure Evolution	82
Section 6.2 Discussion of Surface Structure Evolution.....	88
Section 6.3 Stress Evolution.....	91
Section 6.3.1 Thermal Effect Removal	91
Section 6.3.2 Stress Evolution in Cu/Au(111)- $(22 \times \sqrt{3})$..	94
Section 6.4 Stress and Structure Evolution	96
Section 6.5 Discussion of Stress and Structure Evolution.....	102
7 SUMMARY AND FUTURE WORK.....	107
REFERENCES	112
APPENDIX	
A ORIGINAL STRESS-THICKNESS PLOT WITH A FULL SET OF STM IMAGES FOR FIG. 6.9.....	117
B COPYRIGHT PERMISSIONS	123

LIST OF TABLES

Table	Page
5.1 The Dimensions of Parameters in Eq. 5.1 and Eq. 5.2 (unit: mm).....	50
6.1 Summary for Stress Relaxation and Corresponding Surface Structure Development.....	97
6.2 Summary for Strain Energy vs. Surface Free Energy for Strain Relief Surface Structure Change.....	104

LIST OF FIGURES

Figure	Page
<p>2.1 Wood's notation on different surfaces of FCC structure (a) (100) surface: $b_1/a_1:b_2/a_2 \rightarrow (3 \times 1)$ structure, (b) (110) surface: $b_1/a_1: b_2/a_2 \rightarrow (2 \times 1)$ structure, (c) (111) surface: $b_1/a_1:b_2/a_2 \rightarrow (\sqrt{3} \times \sqrt{3})$ R30 structure (the unit cell of surface is rotated by 30° with respect to the substrate unit cell, which is indicated by R30).....</p>	8
<p>2.2 STM images for surface reconstruction of (a) Si(100)-(2×1) (120nm×120nm) [33], (b) Si(111)-(7×7) (19nm×19nm) [34] and (c) Au(111)-(22 × √3) (150nm×150nm) [35] structures</p>	9
<p>2.3 Dimer Adatom Stacking Fault (DAS) model for Si(111)-(7×7) reconstruction [36].....</p>	11
<p>2.4 STM image of quasi-hexagonal structure of Pt(100)-(6×30) reconstruction (20nm×20nm). The thirteen unit cells are highlighted by the white lines [37]</p>	13

- 2.5 STM images of Au(111)-($22 \times \sqrt{3}$) reconstruction. (a) STM image for herringbone structure with the ball model for the unit cell (marked with the rectangle in the image) [38]. The unfaulted and faulted regions are separated by the corrugation lines, which are indicated by “BRIDGING” in the figure. The stacking sequence of the faulted and unfaulted regions is described by the ball model. The “BRIDGING” area is composed of the open balls in the model.
- (b) STM image (170nm×170nm) [39] the pair-wise corrugation lines of herringbone structure. The edge dislocations are described in the highlighted inset. 15
- 2.6 The surface structures of Ag/Pt(111) resulted from two different growth conditions. (a) STM image of Ag dendrites, grown at 110K [1,41]. (b) STM image of misfit dislocation networks formed in 2ML of Ag, resulting from a 400~500K growth and a subsequent 800K annealing processes. The 20nm-scale bars are located at bottom right corner of each STM image [42] 17
- 2.7 STM images of Cu/Ru(0001) [43] (a) 1st Cu layer with pseudomorphic structure (7.7nm×40nm), (b) 2nd Cu layer with stripe pattern (top), 3rd Cu Layer with triangular pattern (middle) and 4th Cu layer with moiré pattern (lower right corner) (193nm×115nm). 20

Figure	Page
<p>2.8 Herringbone structure of Ag/Ru(0001) [45] (a) STM image of short period herringbone structure at the coverage of sub-monolayer of Ag. The unit cell is marked with the red box. (b) Cartoon model for short period herringbone structure. The box with the dotted Line corresponds to the red box in fig 2.8(a). The arrows correspond to the burgers vectors of Shockley partial dislocation. The threading edge dislocations are located at the ‘elbows’ marked with “T”. (c) STM image of long period herringbone structure at full monolayer</p>	22
<p>2.9 STM image of 2ML Ag/Ru(0001) and a cartoon model for the complicated networks of dislocations [44]. (a) The unit cell is highlighted by the red diamond shape. The three fold symmetry feature is shown in green lines. Each black line corresponds to the location of edge threading dislocation. Inset shows the height modulation of EAM calculation for the trigonal structure. (b) The cartoon model for the trigonal structure describes the complicated network of Shockley partial dislocations and edge dislocations. The curbed lines represent the Shockley partial dislocations at Two interfaces of 2nd layer Ag / 1st layer Ag and 1st layer Ag / Ru. Edge dislocation is displayed by the vertical segment. The complicated network resulted from the interweaving of three sets of equivalent</p>	

Figure	Page
2.9 dislocation networks, which are shown in three different colors, yellow, magenta and cyan	24
2.10 STM images 1.5ML Ag/Pt(111) (52nm×52nm) [42] (a) Stripe pattern in the second layer and pseudomorphic structure in the first layer (lower left) (b) Trigonal pattern in the second layer resulted from a subsequent annealing.....	26
2.11 Evolution of stress and surface structure in Cu/Au(111) system [48]. (a) Stress evolution during Cu growth on Au(111). Line 1 corresponds to the pseudomorphic structure, and line 2 is result of formation of a Shockley partial dislocation. (b) The trigon structure, which is composed of a Shockley partial dislocation, is observed by MD simulation. (c) MD results show the island on the first layer at the coverage of greater than 1/2ML. The enlarged image shows the island. (d) The Cu adlayer of on Au(111) shows additional ledge injection of dislocations at 500K, which is enabled by overcoming the activation energy at the high temperature.....	28

- 4.1 The exponential relation between tunneling current (I) and tip-sample separation (d) is expressed by the curve and the corresponding inset tunneling current equation [54]. On the left hand side of the vertically dotted line, the tunneling current (I) is extremely sensitive to the tip-sample separation (d). Only very slight changes in “ d ”, in a sub-nanometer range, result in a significant change of “ I ”. Thus, the tunneling current can resolve a single atom in the sample..... 36
- 4.2 The simple structure of the tip for the spherical-tip approximation suggested by Tersoff and Hamann [58] (R : the radius of curvature, \mathbf{r}_0 : the vector for center location, d : the separation between tip and the sample)..... 39
- 4.3 A cartoon model to show the tunneling current results from the combination of the sample topography and the density of state of the sample surface. The electrons tunnel into the empty state of the sample, which is positively biased. The sample has a foreign atom and an atomic step. The trace of the probe tip (black line) goes down at the foreign atom due to the different density of state even though the sample height does not change. The trace goes up at the step where the sample surface height increases 40

Figure	Page
4.4 Cantilever bending results in deflection, u_z . The left hand side of the cantilever is clamped. t_s and L are the thickness and the length of the cantilever, respectively.....	43
4.5 Schematic of experiment setup [64]. The cantilever is clamped at side A. The free end of the cantilever is positioned between capacitance electrodes B and B'. One of the electrodes acts as a reference. The STM tip is engaged at the area marked with 'C' where the (7×7) structure is formed.....	46
5.1 Schematics of heating elements for elevated temperatures growth. (a) The ring type tungsten filament (red color) is enclosed in the Macor disks. (b) The cross-sectional view of the sample holder with the heating filament. In the drawing, the coil type tungsten filament (red color) is located behind the sample (blue color).....	48
5.2 The deposition source is inserted in the cylinder type enclosure made of stainless steel. Two titanium foils with center holes are located in front of the source material	49
5.3 (a) Initial attachment of source material (in a ribbon shape) to the tungsten filament. (b) Ball shape of the source material after resistive heating the tungsten filament	51

Figure	Page
5.4	A cylinder type enclosure of the deposition source is aiming to the center of the STM stage. The deposition source unit is inserted into the back side of the enclosure. The STM sample holder is not shown in the picture 52
5.5	The completed setup of STM system for the advanced capabilities that are used to measure the stress evolution and obtain the STM topographies of sample surfaces during the deposition of the films... 53
5.6	The UHV chambers are composed of the preparation chamber for cleaning and depositing of samples and the STM chamber that is involved in surface imaging and measuring stress during film growth. The two chambers are separated by the gate valve so that the prepared sample can be transferred by the load arm to the STM chamber without exposing the sample to the atmosphere. The load lock system, on the left hand side of the figure, protects the preparation chamber from an atmospheric contamination when the sample is inserted from outside 55
5.7	Optical microscope images for STM probe tips on two different substrates, SiN membrane and glass cantilever (magnification: $\sim 10\times$). (a) The tip is located at the center of the SiN membrane substrate. (b) The tip is located at $\frac{3}{4}$ of the cantilever length from the clamp..... 61

Figure	Page
5.8 STM images (100nm x 100nm) of 0.3ML Cu/Au(111)- ($22 \times \sqrt{3}$) obtained at two different locations. (a) STM image of the original location, obtained during <i>in-situ</i> Cu deposition. (b) The probe tip was moved from the original location after Cu deposition and re-engaged at a different location.....	63
5.9 STM images (100nm×100nm) of 1.0ML Cu/Au(111)- ($22 \times \sqrt{3}$) obtained at two different locations (in the same way as Fig. 5.8) of (a) the original location and (b) a different location	64
5.10 Change of STM probe tip height in response to the stress in the film on the membrane substrate. The probe tip extends (retracts) for the tensile (compressive) stress	65
5.11 (a) Stress evolution during Cu deposition with a stationary STM probe tip, no surface imaging. (b) STM image of 0.9ML Cu obtained with a bulk mica substrate (100nm×100nm). (c) The stress evolution during Cu deposition while STM imaging. (d) One of the STM images (Cu coverage: 0.9ML) obtained during in-situ stress measurement and imaging of (c) (80nm×80nm).....	67
5.12 Stress and structure evolution with SiN membrane substrate. The stress measurements were conducted during STM imaging. The repeating segment in the plot corresponds to each STM image (100nm×100nm).....	70

- 5.13 Optical microscope images ($\times 80$) of Au(111) on SiN membrane.
 (a) The cantilever (0.14mm \times 0.45mm) is shown on the right hand side of the picture. (b) The cantilever and the two other rectangles were curled up due to the subsequent Au(111) growth..... 71
- 5.14 (a) Stress evolution during Cu deposition with simultaneous STM imaging. (b) Bare surface of Au(111)-($22 \times \sqrt{3}$) (100nm \times 100nm). (c)~(e) Cu coverages for each image are 0.1ML, 0.5ML and 1.1ML, respectively 72
- 5.15 The change in the probe tip height according to Cu deposition out of the membrane (blue), resistive heat of filament only (red), external light (orange) and Cu deposition on the membrane (black)..... 74
- 5.16 Schematics of experiments to screen the thermal effect on glass cantilever. (a) The cantilever deflects due to heat only without deposition source. (b) The cantilever deflects by stress evolution associated with Cu deposition from the deposition source and the heat effect 76
- 5.17 The two curves, corresponding to Eq. 5.3, represent 10% error boundaries in substrate curvature calculation with the Stoney relation for any values of h_f/h_s and M_f/M_s . The region bounded by the two curves and the coordinate axes, therefore, has less than 10% error in the Stoney relation [7] 77

5.18	The height of the probe tip vs. time for resonance frequency measurements. The peak at 10 sec corresponds to the physical impact on the STM system to enhance the resonance frequency of the cantilever. The time scale for every data point is 10 nano-seconds....	79
5.19	The peak at 4kHz may correspond to the resonance frequency of the mica cantilever.....	80
6.1	STM images of clean Au(111)-($22 \times \sqrt{3}$) surfaces with magnifications (a) 85nm \times 70nm and (b) 20nm \times 11nm	82
6.2	(a) STM image of 0.4 ML of Cu on Au(111)-($22 \times \sqrt{3}$) (140nm \times 45nm). (b) Line profile along the black arrow (The step height is about 0.15nm).....	83
6.3	(a) STM image of 0.4 ML of Cu on Au(111)-($22 \times \sqrt{3}$) (80nm \times 40nm). (b) Line profile along the black arrow (The step height is about 0.20nm).....	84
6.4	STM images, focused on image quality, (a) 0.1ML Cu on Au(111)-($22 \times \sqrt{3}$) (100nm \times 100nm). (b) 0.5ML Cu on Au(111)-($22 \times \sqrt{3}$) (100nm \times 100nm). (c) The stripe pattern in Cu adlayer on Au (111))- ($\sqrt{3} \times 22$) with long corrugation lines. (d) 0.8ML Cu on Au(111)- ($\sqrt{3} \times 22$) (60nm \times 80nm)	86

Figure	Page
6.5	The series STM images (100nm×50nm) of Cu on Au(111)- ($22 \times \sqrt{3}$) showing the process of trigon pattern formation from stripe pattern. The pattern alteration process is shown at two locations in the two locations in the Cu adlayer indicated by the white arrows..... 87
6.6	(a) Results of thermal calibration on three different locations (two curves in a group per the probe tip location, blue 1.7mm, red 2.2mm and gray & black 3.0mm from the clamp) (b) Stress evolution plot on the corresponding location of 2.2mm from the clamp. 92
6.7	Stress-thickness (N/m) vs. thickness plots after thermal effect correction 93
6.8	(a) Stress evolution plot according to Cu thickness after thermal effect correction. This work was done with glass cantilever. (b) STM image of Au(111)- ($22 \times \sqrt{3}$), 100nm×100nm, (c)~(e) STM images of Cu on Au(111)- ($22 \times \sqrt{3}$) (80nm×80nm). Cu coverage: (c) 0.2ML, (d) 0.5ML, (e) 1.0ML..... 95

6.9 Results of simultaneous stress measurement and surface imaging. The abrupt transition in the STM images resulted from shifting the position of the STM probe tip during imaging process. For instance, the STM image “(f)” has a repeating area because the STM probe tip scanned again the same area after the position shifting. (a) Stress-Thickness (N/m) vs. thickness plot. Line 1 and Line 2 correspond to the slopes of the first segment and the second through the fourth repeating segments, respectively. 10% error bar is located at the peak. (b) Cu island nucleation at the step edge of Au surface. (c) Stripe pattern starts to form. (d) “U” shape ending of stripe pattern is observed. Some of stripe pattern are bent. (e) Disordered lines (marked by the white arrow) and trigon pattern are observed. (f) ~ (k) Trigon pattern becomes dominant as Cu coverage increases. The stable second layer islands are clearly observed in (j) and (k). The size of all STM images is 80nm×80nm, and the scale bar located at the right bottom is 10nm 98

A.1 (a) Stress-Thickness (N/m) vs. thickness plot. Line 1 and Line 2 correspond to the slopes of the first segment and the second through the fourth repeating segments, respectively. 10% error bar is located at the peak. (b)~(t) corresponding STM images showing Cu coverage increase and surface structure development 118

CHAPTER 1: INTRODUCTION

1.1 Stress and Structure in Heteroepitaxial Systems

Nanostructures are often found to have superior electronic, magnetic or mechanical properties compared to bulk structures. This attracts growing research interests due to the possibility of creating a new era of technology in sensors, catalysts, biomedical applications, nanoelectronics, optoelectronics, flexible electronics and the next generation of electronic devices [1-7]. The fabrication of many types of nanostructures involves growth processes for thin films in which growth stresses or intrinsic stresses are developed [8]. The evolution of intrinsic stress is closely related to structural changes in thin films. Others have investigated the effects of stress on structure in numerous thin and ultrathin films [9-15]. Identifying a mechanism that correctly defines the relationship between stress and structure can lead to more efficient fabrication of nanostructures with desired properties.

Excess stress in thin films can cause material failure by generating defects, resulting in deformation and fracture. However, the careful control of stress can result in proper structures with greater device performance. The strained metal oxide semiconductor field effect transistor (MOSFET), for example, benefited from stress-enhanced hole and electron mobilities that were first demonstrated by Bell Laboratories in 1954 [16, 17]. In May 2011, Intel announced a new type of nanoscale transistor, called three dimensional tri-gate transistors, which utilized the beneficial effects of increased carrier mobility by the control of stress [18].

Wong et al. summarized the stress effects on the carrier mobility that depends on the type of stress (i.e., tensile or compressive) [17]. The type of stress determines whether the conduction and valence bands will shift. If the conduction (valence) band that has light electrons (holes) shifts down (up), the effective mobility of the respective carrier is increased. As an example of carrier mobility enhancement by compressive stress, the mobility of holes in strained SiGe-pMOSFET was improved by 200% [19]. Ko et. al. fabricated an ultrathin compound semiconductor composed of indium arsenide (InAs) to use as a nanoscale transistor [4]. This research was motivated to find alternative ways to overcome the scaling limitation of Si-based devices. In the nanoscale devices that are fabricated based on ultrathin films of heteroepitaxial systems, one of the main sources of stress is from misfit strain at the interface. Understanding the relationship between stress evolution and the corresponding strained structure is of key importance for further research in such nanoscale devices.

Stress has significant effects on the reliability of interconnects [20, 21]. Electromigration builds a stress gradient that is associated with a flux of atoms driven by electron flow in interconnects. In the tensile region, voids are formed, causing an open circuit due to depletion of atoms. Hillocks form in the compressive region due to excess atoms and can incite a short circuit. Electromigration also sets up a gradient in vacancy concentration as the concentration of vacancies tends to be highly stress dependent [21]. Due to the vacancy concentration gradient, atoms migrate from the compressive to the tensile region of the interconnects, resulting in a steady state stress [20, 21]. This failure

mode can be prevented if the structure of the interconnects is made to sustain a steady state stress [20].

Graphene is another example of an ultrathin film whose properties can be affected by stress. Graphene has been an active research area since the successful isolation of the monolayer from graphite using scotch tape [22]. In order for electronic devices to benefit from its properties, it is necessary to find methods for large-scale pattern growth [3]. Graphene can be epitaxially grown on crystalline substrates such as SiC and Ru [23, 24]. By means of a growth and transfer method, Kim et. al. synthesized a large-scale patterned graphene layer [3]. This synthesis method produced a material with good optical, electrical and mechanical properties for flexible and stretchable electrodes. The structure of graphene can be affected by substrate crystallinity when the synthesis involves heteroepitaxial growth. The lattice mismatch between graphene and the crystalline substrate results in a strained heteroepitaxial structure that is associated with stress development in graphene. Therefore, the understanding of stress-structure relationships in graphene is expected to be important for large scale synthesis of graphene-based devices.

Finally, metastable structures are found in ultrathin metallic films that are heteroepitaxially grown [25]. Magnetic materials that adopt a metastable structure in ultrathin films have different magnetic properties than their bulk counterparts [25-27]. In the case of magnetic recording devices, as the density of data storage in ferromagnetic domains is increased, higher magnetic anisotropy energy is required. Spontaneous changes in magnetization direction can be prevented in

magnetic materials with higher magnetic anisotropy energy [1]. In the case of submonolayer Co on Pt(111), the magnetic anisotropy energy is remarkably improved, up to two orders of magnitude, as the dimension decreases to an atomic layer [1]. Metastable structures in ultrathin films result from intrinsic stress that develops during heteroepitaxial growth. It is important to understand stress evolution in ultrathin metallic films for the research of metastable structures and other effects that can be produced in devices through stress engineering.

1.2 Synopsis

It is evident from literatures [28-30] that combined methods of *in-situ* stress and electron diffraction technology can detect changes in the average surface structure but not local changes that are associated with stress evolution. The value of STM is that it provides direct observations of local details of surface structures. Combining STM with *in-situ* stress measurement makes it possible to study stress evolution and local surface structure development during growth of ultrathin films.

The work reported here concentrates on ultrathin metal films that have a high atomic mobility on the surface. Thus, STM images of the surface structure at multiple locations are sufficient to be representative of the overall surface. In order to combine the imaging process with stress measurements in a STM system, a custom designed small deposition source was installed in the limited space of the STM stage. The design and modification processes are explained in Chapter 5. It was necessary to align the deposition source perfectly with the center of the

STM stage while simultaneously ensuring an appropriate deposition angle with respect to the STM head. If this painstakingly perfect alignment had not been performed, the deposition flux would have contaminated the STM system and caused it to malfunction. The sample holder was also modified to accept samples with two different geometries: membranes and cantilevers.

The STM imaging process had to be done in extremely stable environments with minimal temperature variation and electrical or mechanical noise. The temperature requirement can be easily broken during deposition owing to heat generation in the deposition source. The bulk type substrate for STM imaging was replaced with membranes or cantilevers that can deflect during film growth. The deflection capability is another factor that negatively affects stabilization for the imaging process. To overcome these challenges, it was necessary to find suitable experimental conditions, including the proper dimension of the cantilever or membrane, an appropriate power setting for the small deposition source, and suitable STM scanning parameters such as scanning speed, time constant and tunneling current gain.

The modified STM system was used to study the Cu/Au(111)- $(22 \times \sqrt{3})$ system. The result of this work shows correlations between stress evolution and strain-relief surface structure development in ultrathin Cu film. The results and discussion of stress and structure evolution for the current system are provided in Chapter 6. The results, also, allow for visualization of the development of a nano-scale misfit dislocation network, which forms upon deposition of a monolayer of Cu on Au(111)- $(22 \times \sqrt{3})$. Finally, Chapter 7 covers

the summary and future work that propose an extended study for the Cu/Au(111)
- $(22 \times \sqrt{3})$ system as well as further investigations for other heteroepitaxial
systems using the modified STM system.

CHAPTER 2: SURFACE STRUCTURES

At the surface of solids, the translational periodicity of bulk material terminates in the direction normal to the surface (z direction). The lateral periodicity along the x and y directions can be either maintained or changed at the surface. The surface structure is formed by the native bulk materials or adsorbates. According to Wood's notation for surface structure definition, each side of the surface mesh is compared with that of bulk mesh in lateral directions. The notation for the surface structure is built by the ratio of each side of surface mesh to that of the bulk. For example, if the surface has adsorbates, the periodicity of the adsorbate's mesh may differ from the bulk material's. Then, the surface structure is named according to the ratio as shown in Fig. 2.1. In other cases, the periodicity of surface changes from that of the bulk material by a rearrangement of surface atoms, or via so-called surface reconstruction. Surface reconstruction occurs in clean solid surfaces or is manifested by the presence of adsorbates on the surface [7, 31]. While reconstruction is shown in surfaces of a few transition metals, most semiconductors display surface reconstruction [31, 32]. Fig. 2.2 shows several examples of reconstructed surfaces, Si(100)-(2×1) [33], Si(111)-(7×7) [34] and Au(111)-(22 × √3) [35].

Strain relief patterns are another surface structure found on the surface of heteroepitaxial films. The heteroepitaxial film is grown on a substrate with similar symmetry but different lattice parameter. When the film is enough to maintain the

epitaxial condition at the film-substrate interface, the thin film follows the lateral periodicity of the substrate. In this case, the surface structure of the thin film is called a (1×1) pseudomorphic structure

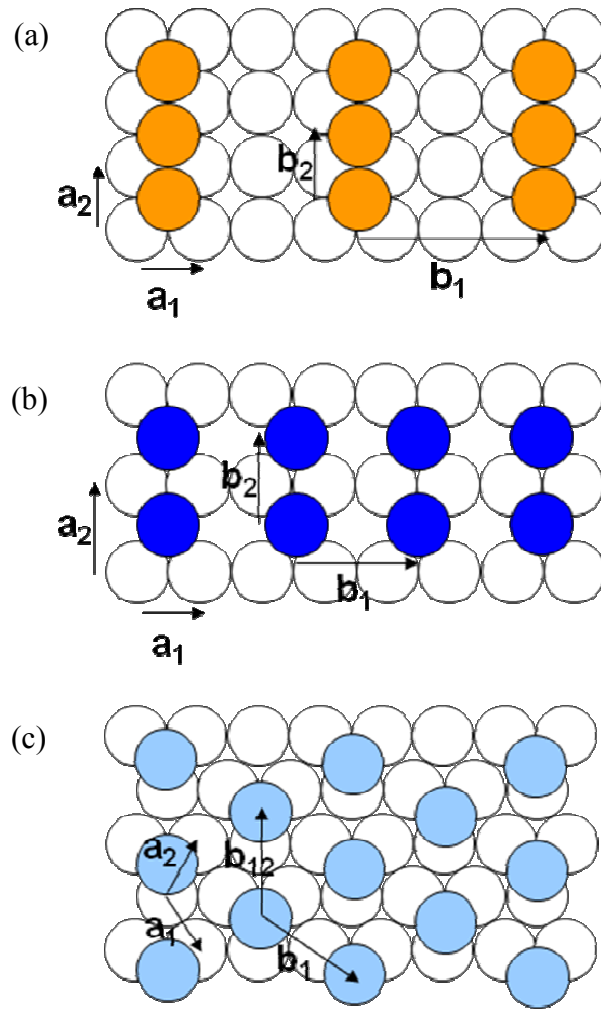


Fig. 2.1 Wood's notation on different surfaces of FCC structure (a) (100) surface: $b_1/a_1 : b_2/a_2 \rightarrow (3 \times 1)$ structure, (b) (110) surface: $b_1/a_1 : b_2/a_2 \rightarrow (2 \times 1)$ structure, (c) (111) surface: $b_1/a_1 : b_2/a_2 \rightarrow (\sqrt{3} \times \sqrt{3})$ R30 structure (the unit cell of surface is rotated by 30° with respect to the substrate unit cell, which is indicated by R30).

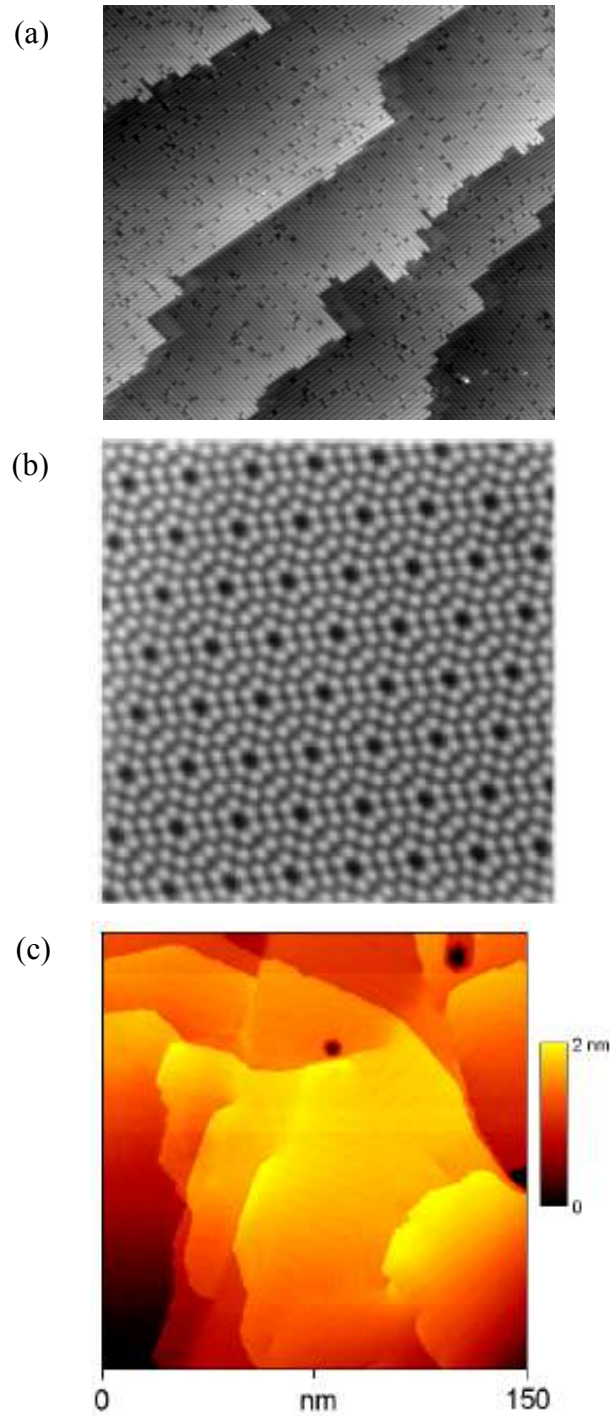


Fig. 2.2 STM images for surface reconstruction of (a) Si(100)-(2×1) (120nm×120nm) [33], (b) Si(111)-(7×7) (19nm×19nm) [34] and (c) Au(111)-(22×√3) (150nm×150nm) [35] structures.

The lattice mismatch between the film and the substrate creates a condition of epitaxial strain. At a certain thickness, the epitaxial condition begins to erode, introducing misfit dislocations due to the lattice mismatch at the interface. The lines and networks of these misfit dislocations form distinct patterns with structures that differ from both the substrate and the bulk material of the film. These are called strain relief surface structures, because the strain is released as the bonding is disconnected at the interface.

2.1 Surface Reconstruction

When the surface is formed from the bulk in ultra high vacuum conditions, the surface atoms have less electron density and fewer bonds compared to the bulk. Surface reconstruction involves the rearrangement of surface atoms to compensate for the reduced electron density and atomic bonds. As a result, the structure of the reconstructed surface has different symmetry and periodicity from those of the bulk. Surface reconstruction of Si(100) and Si(111) reduces the density of “dangling” bonds. Each atom in unreconstructed Si(100) surface has two disconnected covalent bonds. Since Si is a diamond cubic structure, the dangling bonds are rotated 90° with respect to the covalent bonds below. Owing to this feature of the diamond cubic structure, each dangling bond links an adjacent dangling bond in either the $[110]$ or the $[\bar{1}10]$ direction. The linking of the adjacent two dangling bonds forms “dimers,” whose row looks like a line in STM topography in Fig. 2(a). The group of lines forms domains that are separated by atomic steps. As two orientations of dangling bonds exist, two domain

orientations, $[\bar{1}10]$ and $[110]$, are found in reconstructed surfaces of Si(100). Crossing the steps up or downward, the two domain orientations repeat each other. The ‘dimer’ formation results in reduction of the density of dangling bonds during the reconstruction process [7].

Si(111)-(7x7) is often described by the DAS model [36]. This model shows a diamond shaped unit cell with 12 adatoms. Fig. 2.3 illustrates the model.

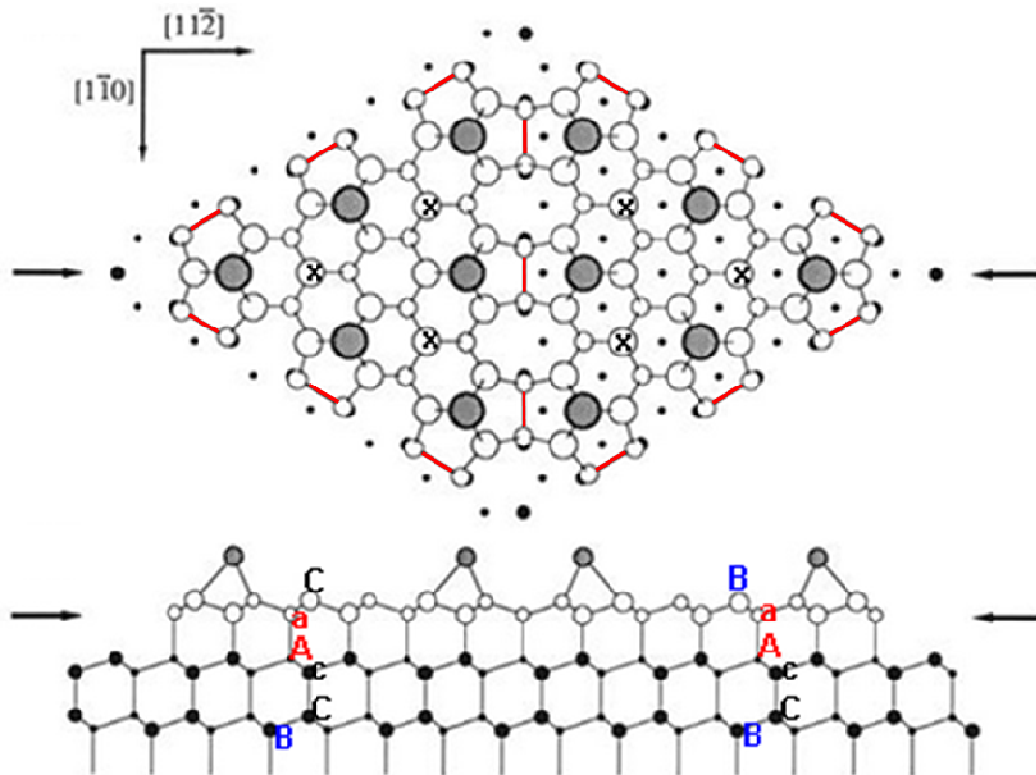


Fig. 2.3 Dimer Adatom Stacking Fault (DAS) model for Si(111)-(7x7) reconstruction [36].

The stacking sequence of the left sub-unit cell shows a C/a fault, while the normal sequence of B/a is found in the right sub-unit cell. The unit cell is thus a combination of faulted and unfaulted regions. The number of total dangling bonds in the unit cell is 49, which is reduced to 19 by dimer formation of dangling bonds. The dangling bonds involving the dimer formation are marked with red solid lines. The remaining dangling bonds are located at 12 adatoms (solid circles), six rest atoms (marked with x) and four corner atoms. Because the corner atoms are shared with adjacent unit cells (so, $4 \times \frac{1}{4} = 1$), the total number of remaining dangling bonds is $12 + 6 + 1 = 19$. This reduction of dangling bonds by dimer formation works as the driving force for the reconstruction of the Si(111) surface.

The reconstruction mechanism for the metal surface is explained differently. Atomic density increase is involved in the reconstruction of transition metals such as, Ir(100), Pt(100), Au(100), Au(111) and Pt(111) [31, 32]. The loss of neighboring atoms causes the decrease in electron density of atoms at the surface. In order to compensate for the deficiency of electron density, surface atoms try to reduce the spacing of nearest neighbors. This induces tensile stress on the surface. The tensile stress can be reduced by compression associated with the increase of atomic density on the surface. However, the contraction involved in reconstruction requires an energy cost for the registry change between surface and bulk lattices. Fig. 2.4 shows a reconstructed Pt(100)-(6×30) surface [37]. The FCC(100) surface is a loosely packed structure compared to the FCC(111)

surface. The structure changes into a close-packed quasi-hexagonal structure by reconstruction, relaxing the large tensile stress of the unreconstructed surface.

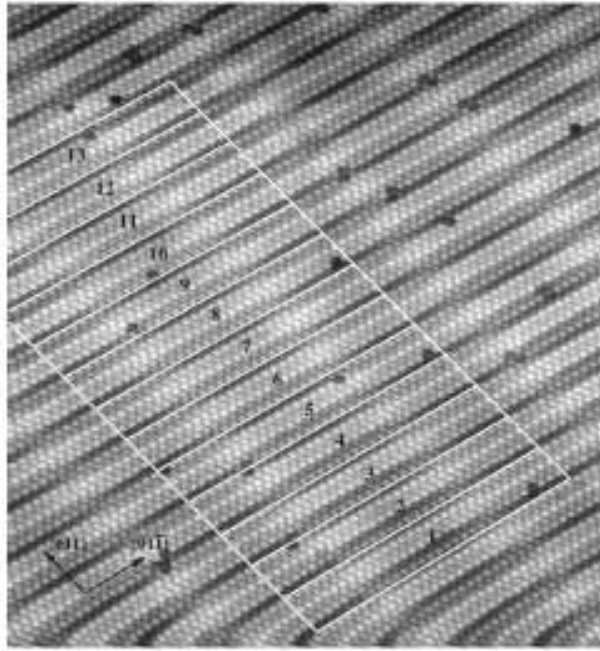


Fig. 2.4 STM image of quasi-hexagonal structure of Pt(100)-(6×30) reconstruction (20nm×20nm). The thirteen unit cells are highlighted by the white lines [37].

A long-range modulation is observed in the direction of [011]. The reconstructed surface is 3.3% contracted with respect to the bulk, increasing the atomic density [37].

The reconstructed surface of Au(111) shows a unique structure, called $(22 \times \sqrt{3})$ structure (Fig.2.5) [38, 39]. This structure cannot be found in the bulk of Au. The reconstruction of Au(111) involves periodic transitions of two stacking regions, FCC and HCP, which are separated by corrugation lines. The corrugation

lines are incommensurate to the bulk lattice. The unit cell structure of reconstructed surface is in a rectangular shape. The reconstruction makes 23 surface atoms in registry with 22 underlying bulk atoms. This results in a uniaxial contraction of $\sim 4.3\%$ along $\langle 1\bar{1}0 \rangle$ directions. As shown in the ball model in Fig. 2.5(a), along the compression direction in the unit cell, the stacking regions vary from the FCC to the HCP region and to another FCC region. The corrugation lines are in a pair and contain Shockley partial dislocations. The Shockley partial dislocations are running along $\langle \bar{1}21 \rangle$ directions. The corrugation lines are periodically bent in a chevron shape. Edge dislocations are located at each elbow of the chevron, which is shown in the highlighted inset of Fig. 2.5(b). Due to this shape, the reconstruction of Au(111) is often called a herringbone structure. The STM topography of the reconstructed Au(111) surface shows that the FCC region is wider than the HCP region, implying that FCC stacking is energetically more favorable than HCP stacking [40]. The reconstructed surface is composed of three different rotational domains [40]. At the transitional region between domains, the parallel corrugation lines are bent by 120° as shown on the lower left in Fig 2.5(b). Therefore, the reconstructed Au(111) surface is compressed by an effective isotropic contraction in a large scale, combining locally favorable uniaxial contractions.

Trimble et. al. described the driving force for Au(111) reconstruction by a thermodynamic model, which is reduction of surface free energy [31]. As the surface contraction of Au(111) reconstruction increases the electron density of

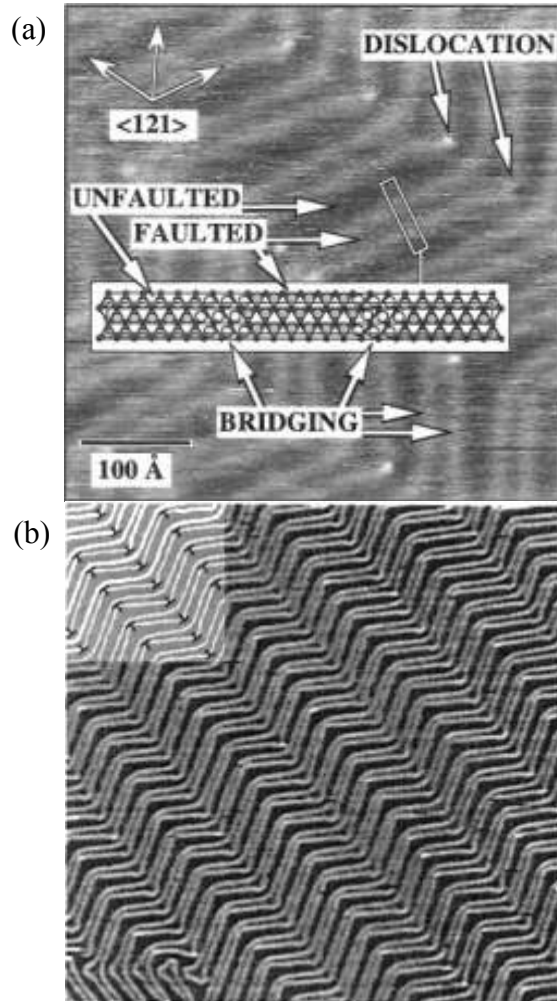


Fig. 2.5 STM images of Au(111)- $(22 \times \sqrt{3})$ reconstruction. (a) STM image for herringbone structure with the ball model for the unit cell (marked with the rectangle in the image) [38]. The unfaulted and faulted regions are separated by the corrugation lines, which are indicated by “BRIDGING” in the figure. The stacking sequence of the faulted and unfaulted regions is described by the ball model. The “BRIDGING” area is composed of the open balls in the model. (b) STM image (170nm×170nm) [39] shows the pair-wise corrugation lines of herringbone structure. The edge dislocations are described in the highlighted inset.

surface atoms, the surface free energy is reduced. However, the formation of Shockley partial dislocations results in energy expense due to disregistry between the surface and the underlying bulk lattice as well as to elastic energy of the uppermost Au layer, which is compressively strained.

2.2 Growth Kinetics for Surface Structure Formation

Once the depositing atoms arrive on the surface, they become surface adatoms and participate in surface diffusion on the surface lattice of the substrate. The surface adatoms travel along terrace ledges or “cross the steps”, overcoming the corresponding diffusion barrier. Each adatom has a distinct lifetime for surface diffusion, which is called adatom life time. The square root of the product of adatom life time and surface diffusivity results in the mean diffusion length that determines the fate of surface adatoms [7]. When surface adatoms encounter nucleation sites or existing islands within the diffusion length, they can contribute to surface structure formation. Moreover, the competition between surface diffusion and deposition rate significantly affects surface structure formation. If the deposition rate is faster than the surface diffusion, the kinetically limited structures result. Conversely, if surface diffusion occurs more quickly than deposition, the traveling adatoms on the potential energy surface have a greater probability of finding minimal energy sites. This condition can produce a thermodynamically favorable structure compared to the previous case. Fig. 2.6 shows the results of two growth conditions explained above. The Ag dendrites in Fig. 2.6(a) result from the kinetically limited growth condition at 110K [1, 41].

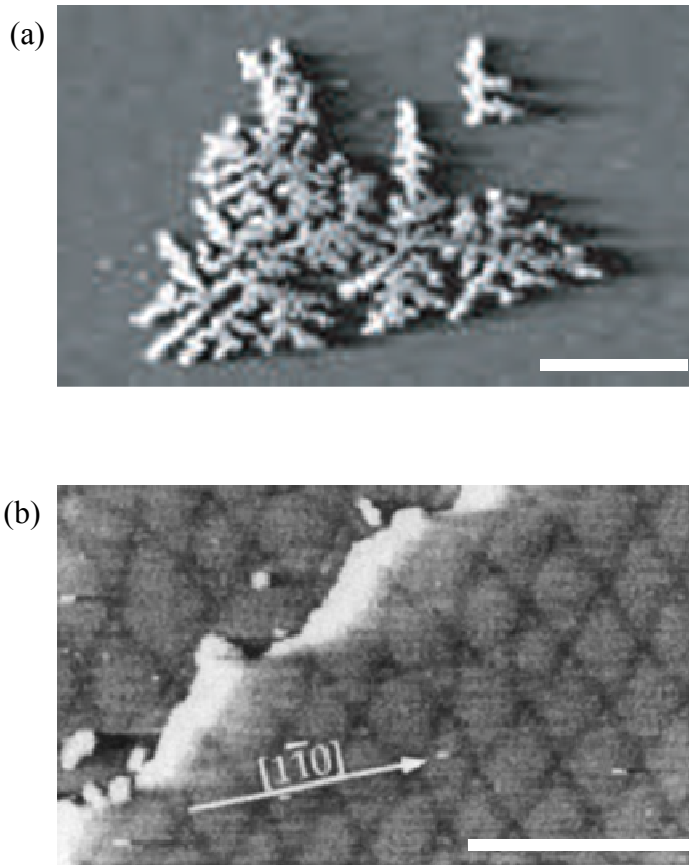


Fig. 2.6 The surface structures of Ag/Pt(111) resulted from two different growth conditions. (a) STM image of Ag dendrites, grown at 110K [1,41]. (b) STM image of misfit dislocation networks formed in 2ML of Ag, resulting from a 400~500K growth and a subsequent 800K annealing processes [42]. The 20nm-scale bars are located at bottom right corner of each STM image.

Because surface diffusion is a thermally activated process and surface diffusivity obeys Arrhenius' law, if the growth temperature increases while fixing the deposition rate, the surface diffusion becomes dominant. The same system of Ag/Pt(111), grown and annealed at higher temperature, is shown in Fig. 2.6(b) [42]. This system belongs to the second growth condition with dominant surface diffusion.

2.3 Surface Structures Formed by Strain Relaxation in Ultrathin Metal Films

A commonly observed sequence in the growth of heteroepitaxial systems that show strain relief structure development is (1) pseudomorphic, (2) stripe, (3) triangle shape or trigonal, and (4) moiré patterns [2, 43-45]. These structures generally all develop, but the coverage range in which they exist is specific to the system. There are two competing potential energies involved in the strain relief structure development in ultrathin films [42, 46]. One is a substrate based potential energy accounting for the effects of the substrate on the film atoms. The other is an interatomic potential energy between the nearest neighboring atoms in the film. These two potentials consist of the Frenkel-Kontorova (FK) model that was used to describe the commensurate-incommensurate transition of metal surfaces [42, 46, 47]. If the former is dominating the latter term, the commensurate phase will form in the film. As a result, the film will have a pseudomorphic structure. If it goes in the opposite way, the incommensurate phase will result, forming a moiré pattern in the film. If the two factors are in a certain balance, the film will display intermediate structures such as the stripe or

triangular pattern. Moreover, a kinetic limitation in the growth processes of films can affect the development of strain relief structures. Some of the structures may be missed or a mixed type of intermediate structure can be displayed.

2.3.1 Cu/Ru(0001) [43]

The Cu/Ru(0001) system displays four different strain relief structures in the stacking sequence of Cu layers [43]. As shown in Fig. 2.7, the first layer displays a fully strained pseudomorphic structure. In the 2 ML and 3 ML of Ag, partially relaxed structures - stripe pattern and triangular shape, respectively - are formed. The last structure is the moiré pattern in 4 ML of Ag. The strain induced by 6% misfit between Cu and Ru lattices is gradually relaxed in the series of the structure. These structures are thermodynamically favorable phases that are formed without kinetic limitations in the growth condition of the Cu layer [43].

The stripe pattern in the second layer is similar to the reconstructed surface of Au(111)- $(22 \times \sqrt{3})$ except for the chevron-like shape. The stacking regions of FCC and HCP are separated by the corrugation lines. Three types of rotational domain are also found in 2ML of Cu as in Au(111) reconstruction. Additionally, the combinational mode of stress relaxation, the overall isotropic mode combining local uniaxial mode, is similar to that of the reconstructed surface of Au(111), explained in the previous chapter.

In the third layer of Cu, the corresponding strain relief structure is an isotropic pattern, where corrugation lines are formed in a triangular shape.

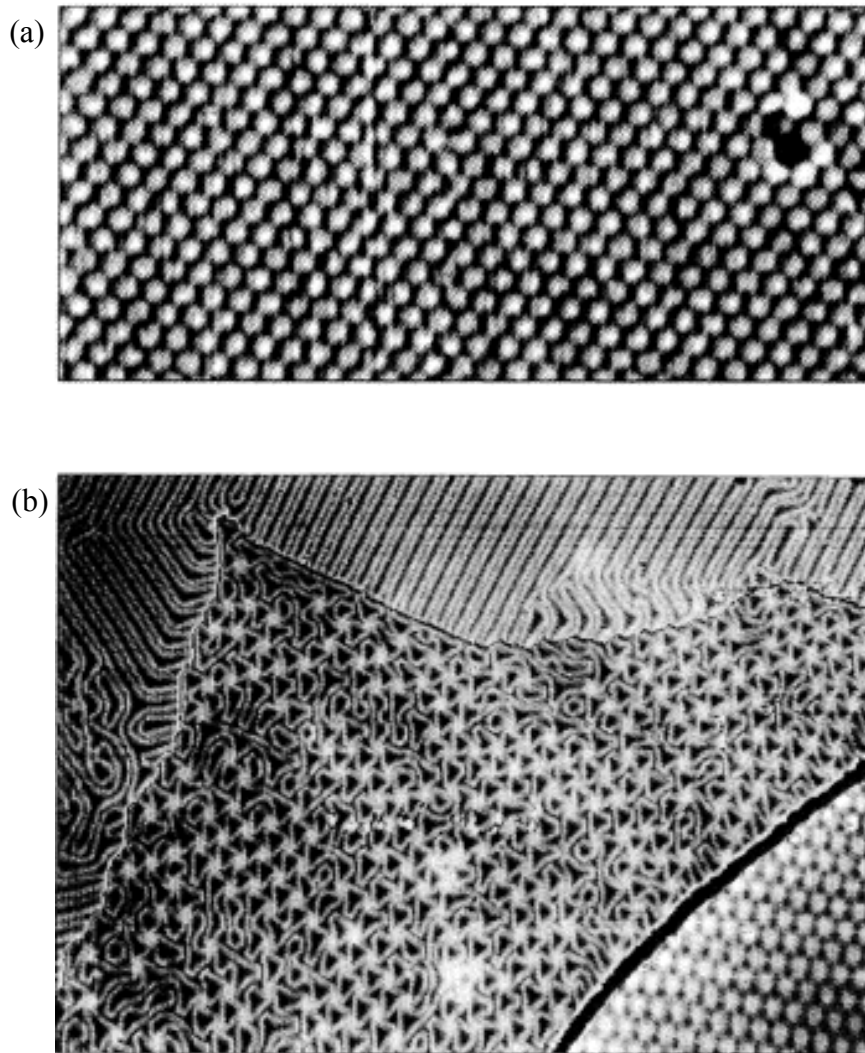


Fig. 2.7 STM images of Cu/Ru(0001) [43] (a) 1st Cu layer with pseudomorphic structure (7.7nm×40nm), (b) 2nd Cu layer with stripe pattern (top), 3rd Cu layer with triangular pattern (middle) and 4th Cu layer with moiré pattern (lower right corner) (193nm×115nm).

The important fact for 3 ML of Cu is that the isotropic pattern cannot be stacked on the uniaxial pattern in 2 ML of Cu [43]. This implies that the formation of the triangular shape in 3 ML of Cu involves rearrangement and mass transport of atoms between successive underlying layers.

2.3.2 Ag/Ru(0001) [45]

A pseudomorphic structure is not observed in the Ag/Ru(0001) system. The compressive misfit strain, 7% is partially relaxed, forming a herringbone structure in 1ML of Ag, which is similar to the Au(111) reconstruction. Further relaxation occurs in 2ML of Ag, forming a complicated network of trigonal structures. The herringbone structure of 1ML Ag/Ru(0001) has two different phases, short period and long period herringbone structures, as shown in Fig. 2.8. The sub-monolayer of Ag displays short period herringbone, in which elbows of the chevron shape are located in every 5.4nm. A longer period, ~20nm, between elbows is found in the full monolayer of Ag. The herringbone structure with a long periodicity especially shows first order transition to short period herringbone at 205°C [45]. The temperature-driven transition of the herringbone structure is a reversible process. Also, the transition decreases the atomic density in the unit cell of the herringbone structure, from 0.928 (of Ru atomic density) for long period herringbone to 0.915 for short period herringbone. While Au(111) reconstruction shows a wider FCC than HCP region, the width of FCC and HCP regions in the stripe pattern of Ag/Ru(0001) [45] is almost equivalent.

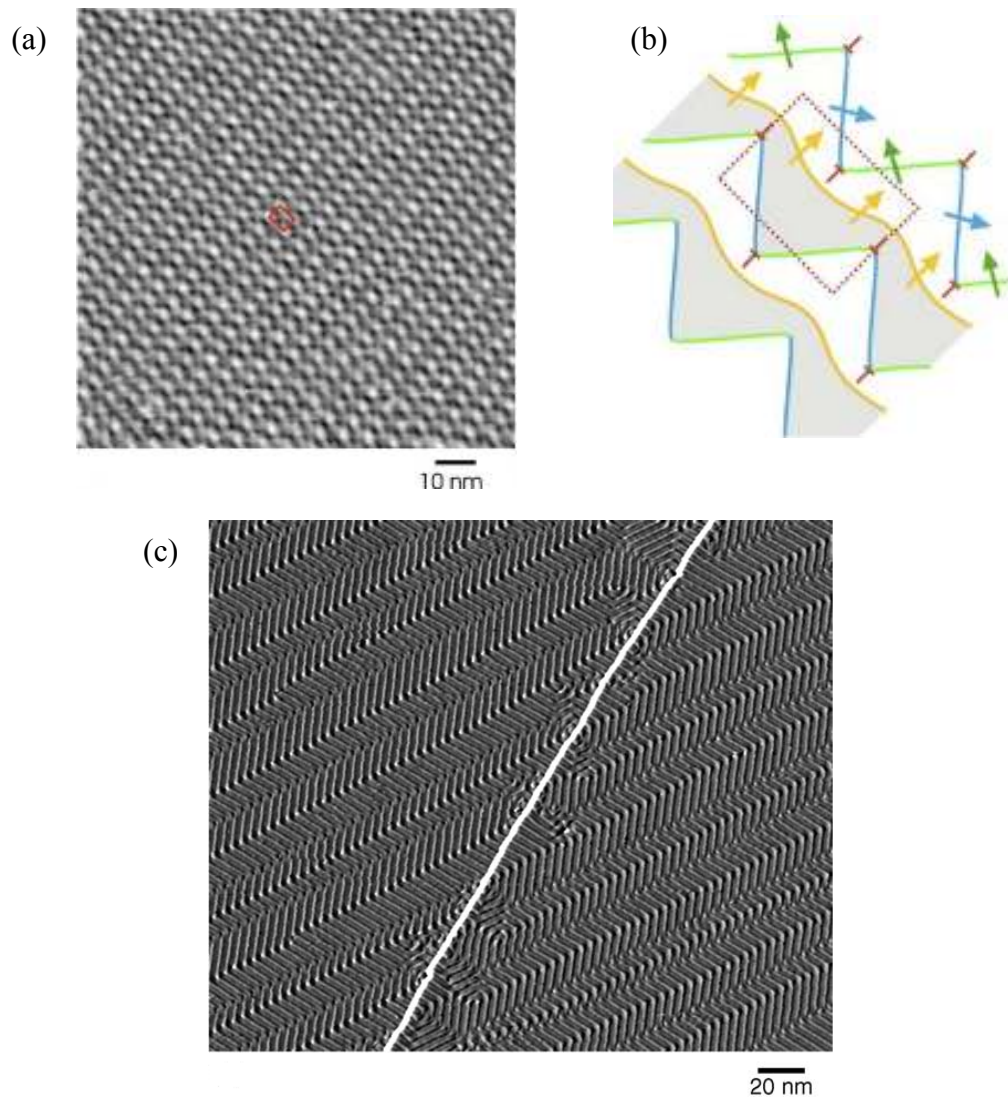


Fig. 2.8 Herringbone structure of Ag/Ru(0001) [45] (a) STM image of short period herringbone structure at the coverage of sub-monolayer of Ag. The unit cell is marked with the red box. (b) Cartoon model for short period herringbone structure. The box with the dotted line corresponds to the red box in Fig 2.8(a). The arrows correspond to the Burgers vectors of Shockley partial dislocation. The threading edge dislocations are located at the ‘elbows’ marked with “T”. (c) STM image of long period herringbone structure at full monolayer.

According to first principle calculations, the energy of FCC sites is almost the same as that of HCP sites for Ag on Ru(0001) [45]. The formation of the trigonal structure in 2ML Ag on Ru(0001) involves the restructuring of Ag atoms in 1ML.

Ling et.al. explained, with STM topography and a schematic diagram showing the stacking sequence of Ag layers (Fig. 2.9), that the trigonal structure is constructed by interwoven dislocation networks[44, 45]. The interwoven network is composed of edge dislocations and Shockley partial dislocations. Shockley partial dislocations form networks of the trigonal pattern in the two interfaces, the second/first Ag layer and the first Ag layer/Ru(0001). The Shockley partial dislocations are confined in the first Ag layer. As shown in the cartoon model, no dislocations are extended into the second Ag layer [44]. The edge dislocation of which location appears as a ‘black line’ in the STM image connects each ‘trigon’ in two different interfaces. As opposed to the STM image of the herringbone structure in Fig. 2.8, the lines of dislocations appear darker in the STM topography of 2ML Ag/Ru(0001) as shown in Fig. 2.9. The authors explained that the second layer of Ag buried the networks of Shockley partial dislocation and edge dislocation. The contrast of the “black line” is possibly resulted from the electronic effect of dislocation structure in the underlying layer [44]. In the first layer, the trigonal structure with HCP stacking is surrounded by FCC-stacked regions. The second layer of Ag has a nearly hexagonal structure without dislocations threaded from the underlying layer. Thereby, the first layer of Ag works as an intermediate for the Ru layer and the second Ag layer, which

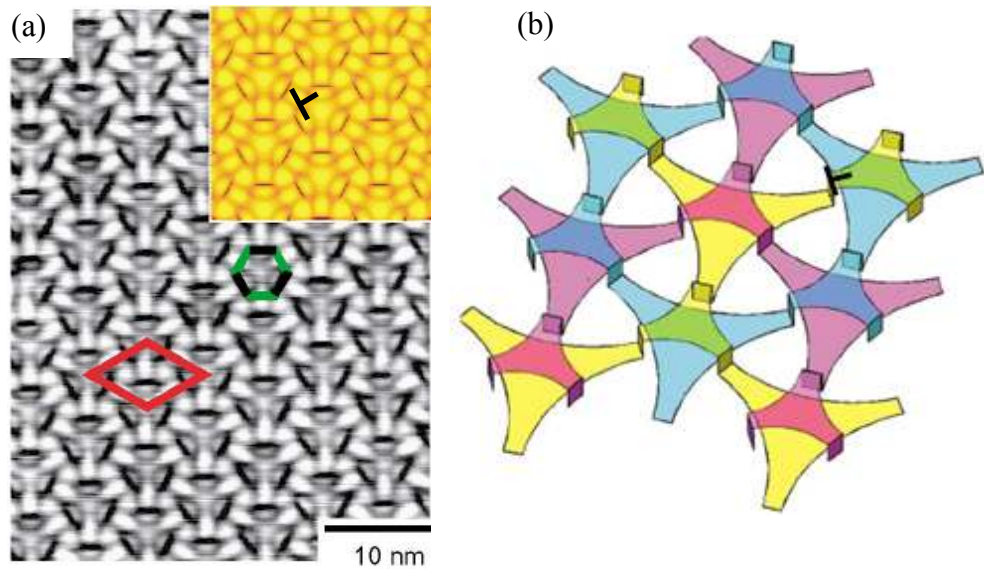


Fig. 2.9 STM image of 2ML Ag/Ru(0001) and a cartoon model for the complicated networks of dislocations [44]. (a) The unit cell is highlighted by the red diamond shape. The three fold symmetry feature is shown in green lines. Each black line corresponds to the location of edge threading dislocation. Inset shows the height modulation of EAM calculation for the trigonal structure. (b) The cartoon model for the trigonal structure describes the complicated network of Shockley partial dislocations and edge dislocations. The curved lines represent the Shockley partial dislocations at two interfaces of 2nd layer Ag / 1st layer Ag and 1st layer Ag / Ru. Edge dislocation is displayed by the vertical segment. The complicated network resulted from the interweaving of three sets of equivalent dislocation networks, which are shown in three different colors, yellow, magenta and cyan.

have different lattice coefficients. The atomic density of the first Ag layer is also in an intermediate value between the densities of the Ru layer and the second Ag layer ($Ru > 1^{st} \text{ Ag layer} > 2^{nd} \text{ Ag layer}$) [44].

2.3.3 Ag/Pt(111) [42]

The STM topography of Fig. 2.10 shows the surface structures of 1.5ML Ag/Pt(111). The first layer displays a pseudomorphic structure. The stripe pattern is formed in the second layer. Those structures resulted from Ag deposition at 300~340K. By a subsequent annealing process at 800K, the stripe pattern in the second layer changes into a trigonal pattern in which the crossing of domain walls forms a triangular shape of networks. The pseudomorphic Ag layer is attached to Pt(111) with a compressive misfit strain of 4.3%. The formation of the stripe pattern is associated with the relaxation of the compressive misfit strain in uniaxial directions along $\langle 1 \bar{1} 0 \rangle$. The pair-wise corrugation lines run along $\langle \bar{1} 2 \bar{1} \rangle$ directions and work as domain walls, separating the FCC and HCP stacking regions. As in the case of Au(111) reconstruction, the FCC regions appear wider than HCP regions. In contrast to Cu/Ru(0001), the stripe pattern of Ag/Pt(111) is not a thermodynamically stable structure. The annealing process changes the stripe pattern into a trigonal structure in the existing second layer of Ag. In this way, the uniaxial relaxation of compressive strain turns to an isotropic mode. The unit cell is composed of two triangles and one hexagon shape. The domain walls that form each shape are oriented along $\langle 1 \bar{1} 0 \rangle$ directions.

The hexagon consists of three long and three short domain walls. The two types of domain walls are alternatively located, connecting each other's ends.

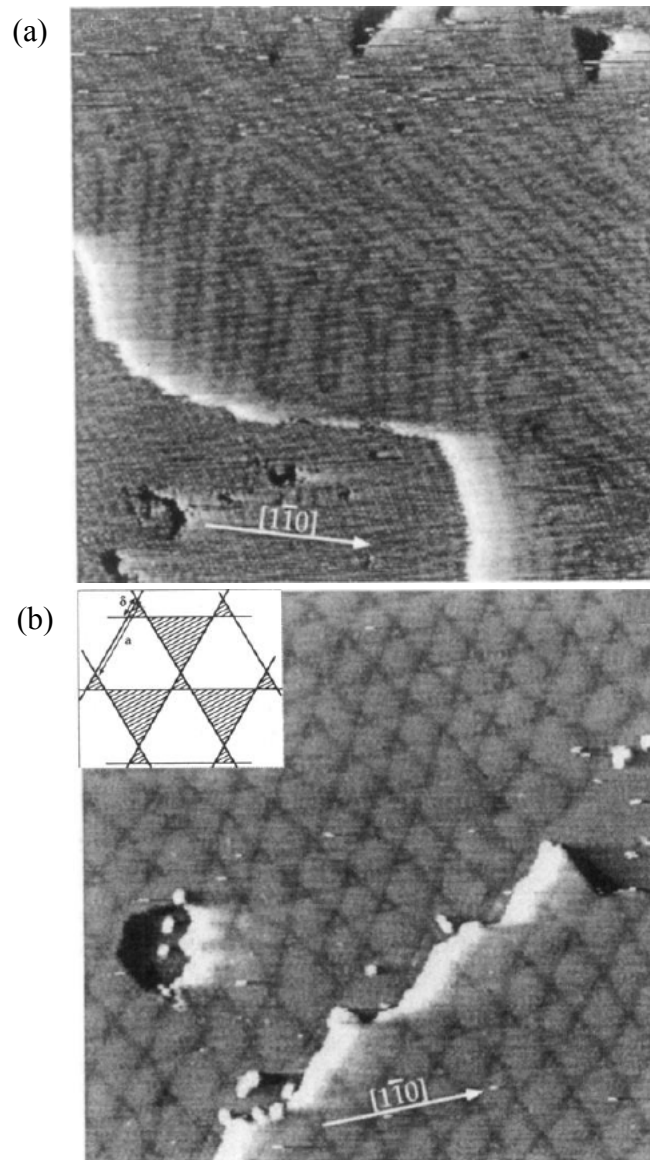


Fig. 2.10 STM images 1.5ML Ag/Pt(111) (52nm×52nm) [42] (a) Stripe pattern in the second layer and pseudomorphic structure in the first layer (lower left) (b) Trigonal pattern in the second layer resulted from a subsequent annealing.

The two triangles, one large and one small, share one vertex together. Also, the two triangles share each one of their domain walls with the hexagon. While the hexagon has the FCC stacking, the triangles have the HCP stacking sequence. The expansion associated with the transition of surface structure reduces the atomic density of Ag. According to Brune et. al.'s atomic model, the atomic densities of the stripe pattern and the trigonal pattern are reduced by 7.1% and 7.0%, respectively, compared to the pseudomorphic first layer [42].

2.3.4 Cu/Au(111) [48]

Trimble et. al. carried out molecular dynamic (MD) simulations to investigate the change of surface structure and the corresponding stress relaxation in Cu/Au(111) [48]. The MD simulations performed Cu growth on the bulk terminated surface of Au(111). The misfit strain of the system is 12%, imposing a tensile stress in the heteroepitaxial layer of Cu on Au(111). As Cu islands grow, a trigon structure is formed in the Cu adlayer, which is associated with the tensile stress relaxation. The MD results of stress evolution are in agreement with experimental results obtained by other research groups [48]. Fig.2.11 shows results of surface structure change and stress evolution of the Cu/Au(111) system. According to the MD simulations, a pseudomorphic structure is formed in a small island, in which the shape is hexagonal. The dimension of one of the hexagon island's sides is up to eight nearest-neighbor spacings. The tensile stress is partially relaxed as Shockley partial dislocations are injected from "A" steps of

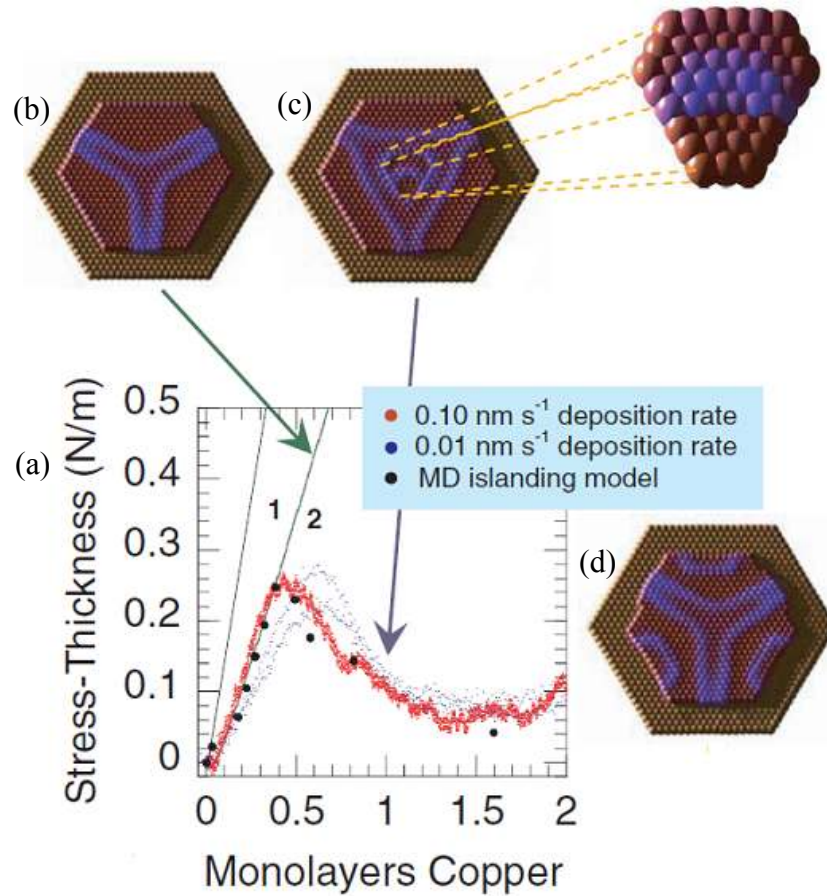


Fig. 2.11 Evolution of stress and surface structure in Cu/Au(111) system [48].

(a) Stress evolution during Cu growth on Au(111). Line 1 corresponds to the pseudomorphic structure, and line 2 is a result of formation of a Shockley partial dislocation. (b) The trigon structure, which is composed of a Shockley partial dislocation, is observed by MD simulations (c) MD results show the island on the first layer at the coverage of greater than 1/2ML. The enlarged image shows the island. (d) The Cu adlayer of on Au(111) shows additional ledge injection of dislocations at 500K, which is enabled by overcoming the activation energy at the high temperature.

the island. The Shockley partial dislocations form the trigonal structure in the growing islands. A further relaxation follows as the Cu coverage reaches 0.5ML. Around this coverage, the second layer islands start to nucleate on top of the first adlayer. The second layer islands play an important role in strain-relief in this stage, providing a source for interlayer transport of atoms. The atoms inside of the top islands funnel into the strained underlying layer. They participate in forming misfit dislocations in the bottom islands. Due to this 'funneling' process, the density of misfit dislocations increases more effectively, resulting in slope-change of the stress evolution plot, into the compressive direction. As the growing islands coalesce each other, the slope changes into the positive tensile direction again at around 1.5ML of Cu, resulted from a tensile stress increase.

CHAPTER 3: SURFACE AND INTERFACE

3.1 Surface Free Energy and Surface Stress

When the surface is created from the solid bulk, there is an energy cost to separate bulk atoms to expose them to the surface (i.e. breaking the bonds of atoms). The reversible work required to create a new surface is called surface free energy (γ) [49]. Once the atoms are exposed to vacuum, they have a lower electron density and fewer bonds compared to the bulk. In order to compensate for the loss of bonding and increase the electron density at the surface, surface atoms try to reduce the nearest neighbor spacing. This requires an elastic energy to adjust the lattice spacing at the surface. Thus, surface stress (f) is defined as a reversible work involved in the elastic deformation at the existing surface [49]. Both of the two reversible works are considered with respect to the unit area. The typical units of the surface stress (N/m) and the surface free energy (J/m²) are the same. The relation between surface free energy and surface stress is described by the Shuttleworth equation [49, 50],

$$f_{ij} = \gamma \delta_{ij} + \frac{\partial \gamma}{\partial \varepsilon_{ij}}, \quad \text{Eq. 3.1}$$

where f_{ij} is surface stress tensor, δ_{ij} is the Kronecker delta, and ε_{ij} is surface elastic tensor for elastic deformation of a solid surface. For surface symmetries greater than three-fold, the surface stress can be considered as a scalar. In this case, the Shuttleworth equation can be expressed in scalar form,

$$f = \gamma + \frac{\partial \gamma}{\partial \varepsilon}. \quad \text{Eq. 3.2}$$

3.2 Interfacial Free Energy and Interface Stress

The interface of film and substrate is formed at the boundary where those two phases adhere to each other. The interfacial free energy σ is the reversible work required to form the interface. An interface, for example, can be formed by attaching two clean crystal surfaces with the same crystal structure that are composed of an identical material after rotating one with respect to the other. The interfacial free energy increases as the rotation reduces the coherency between two phases. It is the same way in the case of the clean surface, as less coordinated surfaces have higher surface free energy. Interface stress is a reversible work per unit area to elastically deform the existing interface. The elastic deformation can be considered as stretching of the interface in two ways [49]. One is to stretch the film relative to the substrate. Its corresponding strain is denoted by e_{ij} . This method consists of stretching only the film while fixing the original dimension of substrate, resulting in a change in the density of misfit dislocations at the film-substrate interface. The other method is to stretch both the film and the substrate, inducing a strain denoted by ε_{ij} . Therefore, two different methods of elastic deformation lead to two types of interface stress. The first interface stress is g_{ij} and corresponds to the strain e_{ij} . The second one is h_{ij} , corresponding to the strain ε_{ij} . The relation between the interfacial free energy and each surface stress

can be described in the analogous way for surface free energy and surface stress [49].

$$g_{ij} = \sigma \delta_{ij} + \frac{\partial \sigma}{\partial e_{ij}} \quad \text{Eq. 3.3}$$

$$h_{ij} = \sigma \delta_{ij} + \frac{\partial \sigma}{\partial \varepsilon_{ij}} \quad \text{Eq. 3.4}$$

For the interface that displays higher than three-fold symmetry, the equations can be expressed in scalar terms.

$$g_{ij} = \sigma + \frac{\partial \sigma}{\partial e} \quad \text{Eq. 3.5}$$

$$h_{ij} = \sigma + \frac{\partial \sigma}{\partial \varepsilon} \quad \text{Eq. 3.6}$$

When the surface structure of the heteroepitaxial film is changed by introducing misfit dislocations at the interface, the interfacial free energy σ is described by the coherency strain e . As this paper continues to discuss the strain relief mechanism of misfit dislocation formation, only e is to be considered from this point on. Cammarata et. al. expressed σ as in Eq. 7, assuming that the major source for σ is formation of misfit dislocation at the interface [49].

$$\sigma = \sigma_0 |1 - (e_{11} + e_{22})/2m| \quad \text{Eq. 3.7}$$

The in-plane strain components, e_{11} and e_{22} , are equal to the coherency strain e . m is the misfit strain between film and substrate, $m = (a_s - a_f)/a_f$, where a_s is the lattice parameter of the substrate and a_f is that of film. Eq. 8 explains $\sigma(0)$, the interfacial free energy for the fully relaxed film, $e = 0$.

$$\sigma(0) = \alpha Mb, \quad \text{Eq. 3.8}$$

In this equation, b is the magnitude of the Burgers vector, M is an effective elastic modulus that is equal to $1/2 \left[(1-\nu_f)/\mu_f + (1-\nu_s)/\mu_s \right]^{-1}$, and α is $[\ln(R/b) + 1] |m - e| / 2\pi$. In those sub equations, μ_f and μ_s are the shear moduli of the film and the substrate, ν_f and ν_s are Poisson's ratios of the film and the substrate, and R is an effective dislocation stress-field radius [49, 51]. According to eq. 3.8, when $e = m$ for the coherent film, $\sigma(m)$ is equal to zero, resulting from ignoring chemical differences between two phases that contribute to the interfacial free energy, which is nonzero. However, the chemical contribution is expected to be significantly small compared to the contribution of misfit dislocation to interface energy [49]. Therefore, the change of interfacial free energy for a fully relaxed interface is

$$\sigma(0) - \sigma(m) \cong \sigma(0) = \alpha Mb. \quad \text{Eq. 3.9}$$

3.3 Stress in Ultrathin Film associated with the Misfit Strain

While the film is growing on the substrate, stress in films is developed by several mechanisms such as surface stress, interface stress, grain growth, vacancy annihilation and so on [8]. The major source for stress in the heteroepitaxial system is misfit strain, owing to epitaxy at the interface. The misfit stress (σ_m , σ was used as interfacial free energy in the previous chapter but not in this chapter) is associated with the misfit strain. In the case of the isotropic stress in the perfectly coherent film [8], the misfit stress is

$$\sigma_m = M_f m, \quad \text{Eq. 3.10}$$

where M_f is biaxial modulus of film. If the misfit strain is positive (or negative), a tensile (or compressive) stress is induced in the film. According to the type of stress in the film, atoms attract or repulse each other. When the atoms in the film tend to attract each other, the film is in tensile stress. On the other hand, when the atoms are repulsive to each other, the film is in compressive stress. The elastic energy in the strained film that is associated with the misfit stress is [8, 51]

$$\sigma_m \times m \times t = M_f m^2 t, \quad \text{Eq. 3.11}$$

where t is the thickness of the film. This elastic energy is reduced as the ultrathin film becomes less strained during commensurate – incommensurate transition in the film. If the misfit stress is multiplied by the thickness of the film, the value corresponds to f , isotropic ‘stress-thickness’ or ‘membrane force’ at the thickness. The membrane force is a force acting on the film in the lateral directions [8]. Its physical dimensions are force/length (N/m), which is the same as that of the surface stress.

Chapter 4: SCANNING TUNNELING MICROSCOPY FOR STRESS MEASUREMENTS

4.1 Scanning Tunneling Microscopy (STM)

Since STM imaged the Si(111)-(7x7) structure for the first time in 1983 [52], various surfaces of semiconductors and metals have been revealed in nano or atomic scale images of STM topography. STM is a powerful tool for visualization of individual atoms in real space. Its imaging process is nondestructive for the sample, because the STM topography is obtained by a probe tip that maintains a very small distance from the surface as it scans the sample surface. The principle of STM resides in the quantum tunneling effect that occurs in the “tiny” distance between two electrically conducting materials.

The quantum tunneling effect enables electrical current to flow through a forbidden region of a potential barrier, through which no particles can pass by means of classical physics. STM utilizes the tunneling current between a metallic probe tip and electrically conductive samples.

The tunneling current of STM is exponentially varied with the distance between the probe tip and sample, which is the key feature to obtain atomic resolution in STM images. As long as the probe tip is sharp enough, STM can provide images in atomic resolution. For example, if the tip radius is less than 10nm, the lateral and the vertical resolutions can be up to 0.1nm and 0.01nm, respectively [53].

4.1.1 Tunneling Current

Fig. 4.1 shows the exponential relation of the tunneling current (I) and the distance between the probe tip and sample (d) [54]. Although the inset equation in Fig 4.1 effectively explains the basic concept of STM, it does not clearly show that the tunneling current is related to not only the separation but also the density of state (DOS) of the substrate, a central feature of the technique.

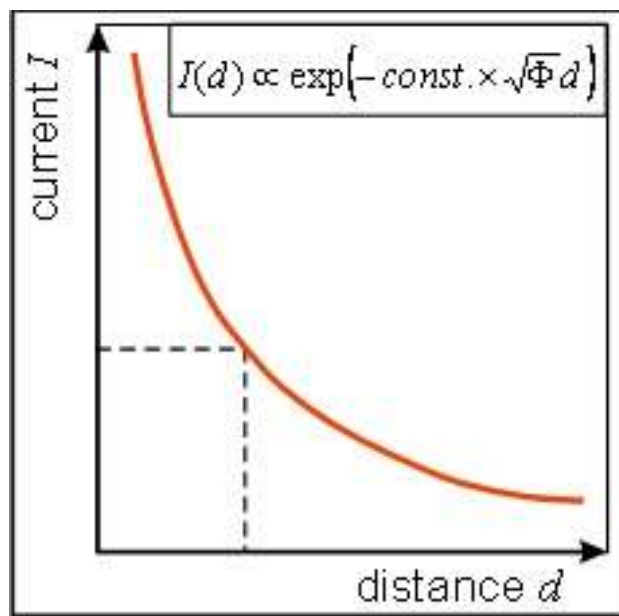


Fig. 4.1 The exponential relation between tunneling current (I) and tip-sample separation (d) is expressed by the curve and the corresponding inset tunneling current equation [54]. On the left hand side of the vertically dotted line, the tunneling current (I) is extremely sensitive to the tip-sample separation (d). Only very slight changes in “ d ”, in a sub-nanometer range, result in a significant change of “ I ”. Thus, the tunneling current can resolve a single atom in the sample.

Binnig and Rohrer [55] explained the tunneling current in terms of tunnel barrier height and the separation between tip and sample of Eq. 4.1,

$$I = f(V) \exp(-\sqrt{\bar{\Phi}} \times s) , \quad \text{Eq. 4.1}$$

where $f(V)$ is the joint local density of states of the tip and the sample, $\bar{\Phi}$ is the averaged-potential barrier height in eV, and s is the separation between two metals. In the equation, $f(V)$ represents the central relation of the tunneling current and the sample DOS. Thus, the tunneling current is determined by applied bias, local density of states of the tip and the sample, and the Fermi function, as well as tip-sample distance. The tunnel barrier is a forbidden region between tip and sample in ultra high vacuum (UHV), where the current cannot flow in the way of classical physics. To express STM's characteristic more exactly, it is necessary to access several approaches in the field of quantum physics, i.e. Bardeen's formalism, Fermi's golden rule and WKB [56]. The major terms in specific tunneling current equations are the probability that the state of each side is empty or occupied and a matrix element between states of tip and sample. Wiesendanger [56] derived the tunneling current within the Bardeen's formalism as shown below,

$$I = \frac{2\pi e}{\hbar} \sum_{\mu,\nu} \{f(E_\mu)[1 - f(E_\nu + eV)] - f(E_\nu + eV)[1 - f(E_\mu)]\} |M_{\mu\nu}|^2 \delta(E_\nu - E_\mu)$$

Eq. 4.2

where $f(E)$, V , and $M_{\mu\nu}$ are Fermi function, applied voltage, and a tunneling matrix element between the unperturbed electronic states of the tip (Ψ_μ) and the sample surface (Ψ_ν) respectively. Also, E_μ and E_ν are the energy of state Ψ_μ and the

energy of state Ψ_ν . In order to obtain tunneling current information from Eq. 4.2, the tunneling matrix element $M_{\mu\nu}$ should be solved. The evaluated form of $M_{\mu\nu}$ is given below [56-58],

$$M_{\mu\nu} = \frac{\hbar^2}{2m} \int dS \cdot (\Psi_\mu^* \nabla \Psi_\nu - \Psi_\nu \nabla \Psi_\mu^*) \quad \text{Eq. 4.3}$$

where dS , Ψ_μ and Ψ_ν are unit area in the surface, the electronic state of the tip, and the electronic state of the sample, respectively. The integral term is to be calculated over tip and sample surfaces. The current density results from calculation of $(\Psi_\mu^* \nabla \Psi_\nu - \Psi_\nu \nabla \Psi_\mu^*)$ in Eq. 4.3. Once Ψ_μ is solved, the DOS for sample can be calculated. The tip structure should be clarified in order to solve the tip state wave function Ψ_μ .

Tersoff and Hamann suggested a tip model as shown in Fig. 4.2. After expanding the tip wave function, they expressed Eq. 4.1 in terms of the sample wave function [58],

$$I = 32\pi^3 \hbar^{-1} e^2 V \phi^2 D_t(E_F) R^2 \kappa^{-4} e^{2\kappa R} \cdot \sum_\nu |\Psi_\nu(\mathbf{r}_0)|^2 \delta(E_\nu - E_F) \quad \text{Eq. 4.4}$$

where Φ , D_t , R , and \mathbf{r}_0 , are the work function, density of states per unit volume of the tip, the tip radius of curvature, and the vector at the center of the tip,

respectively. Also, $\kappa = \sqrt{\frac{2m\phi}{\hbar}}$, and $\sum_\nu |\Psi_\nu(\mathbf{r}_0)|^2 \delta(E_\nu - E_F)$ is equivalent to the

local density of state for sample surface at the point \mathbf{r}_0 , which is $\rho(\mathbf{r}_0, E_F)$ at E_F .

Eq. 4.4 stands on assumptions of low applied bias and temperature, homogeneous density of states at the tip, consideration of only the s wave function (s-wave

approximation), and equal tip and sample work functions [58, 59]. Tersoff and Hamann calculated $\rho(\mathbf{r}_0, E)$ for (2×1) and (3×1) structures of Au(110). The results were consistent with Binnig's high resolution STM measurements [58].

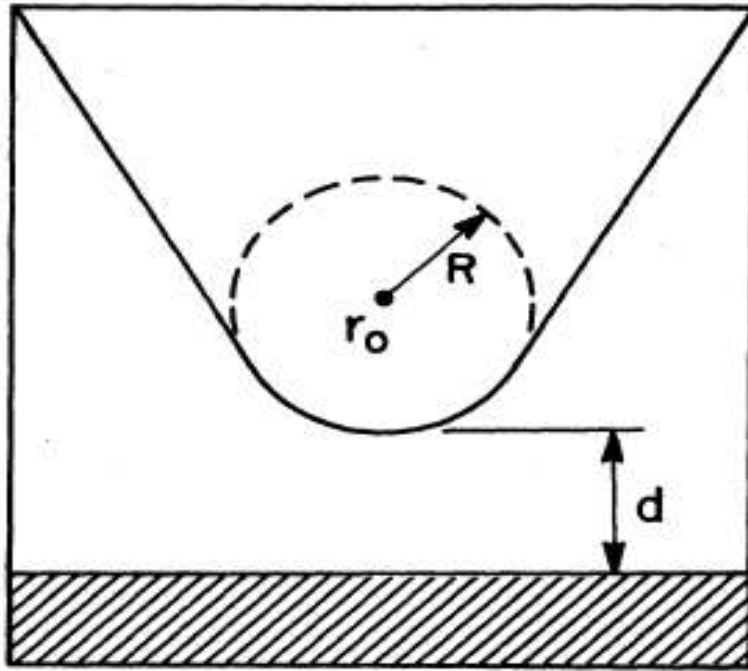


Fig. 4.2 The simple structure of the tip for the spherical-tip approximation suggested by Tersoff and Hamann [58] (R : the radius of curvature, \mathbf{r}_0 : the vector for center location, d : the separation between tip and the sample).

The tunneling current equations explain that the scanned STM image contains mixed information about both local DOS of surface and surface topography. The image does not always represent real features of the surface. For example, Fig. 4.3 shows how the probe tip responds to the foreign atom which is

surrounded by native atoms . In order to reveal the actual surface features, the density of states of the sample structure needs to be clarified.

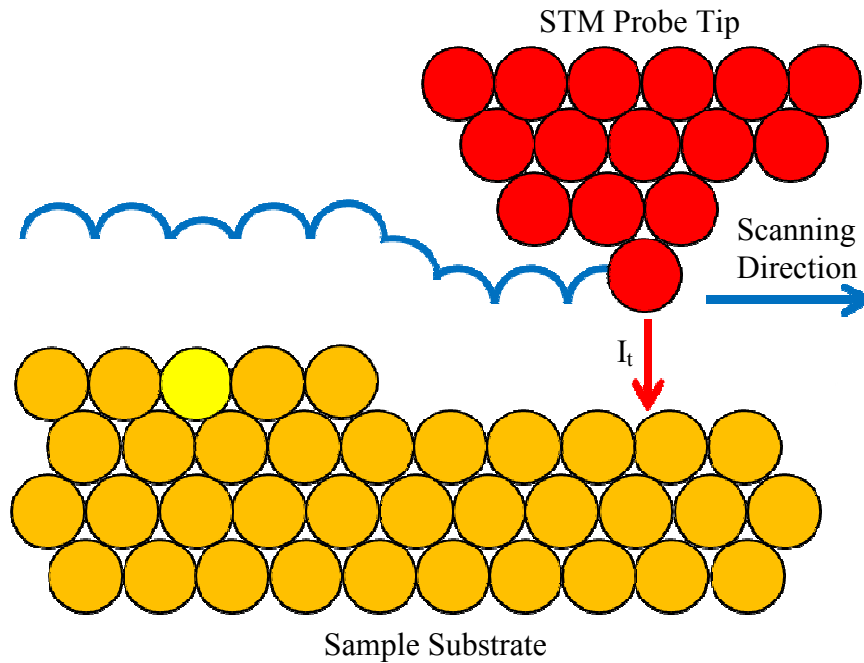


Fig. 4.3 A cartoon model to show the tunneling current (I_t) results from the combination of the sample topography and the density of state of the sample surface. The electrons tunnel into the empty state of the sample, which is positively biased. The sample has a foreign atom and an atomic step. The trace of the probe tip (blue line) goes down at the foreign atom due to the different density of state even though the sample height does not change. The trace goes down again at the step where the sample surface height decreases.

Therefore, STM images of surface structures composed of misfit dislocation lines, as explained in Chapter 2, result from combination of the local DOS and the misfit dislocation height. The STM topography expresses the lower (higher) parts of the sample surface with the darker (lighter) colors, providing a fine contrast for surface features. However, the local DOS of the sample may make the topography unclear as is the case at the “black line” of the edge dislocation in 2ML Ag/Ru(0001) (Fig. 2.9).

4.1.2 STM Topography

The probe tip is attached to a scanning tube that consists of piezoelectric materials. Three dimensional tip motion is driven by x, y and z components of piezoelectric materials in the scanning tube. The dimensions of the piezoelectric materials change according to an applied voltage and range from a few to hundreds picometers per volt [53]. Thereby, the probe tip can move along the sample surface in three dimensions and distinguish each atom on the surface. A bias voltage, applied on the sample for the tunneling process, is typically between 1mV and 4V [56]. Depending on the polarity of the sample bias, + or -, electrons tunnel into the empty state of the sample or into the tip from the occupied state of the sample. When the tip approaches the sample surface, the process typically involves two steps, a coarse approach and a fine approach. In the coarse approach, the tip is brought to the sample within a millimeter range, which may be monitored through an optical microscope. In the fine approach, an electric feedback system monitors the tip approach to prevent the probe tip from crashing into

the sample. The electric feed-back loop contains a current amplifier that converts the tunneling current into voltage with a gain of $10^6 \sim 10^9$ V/A [56]. Comparing the voltage with the reference, the fine approach continues until the designated tunneling current is obtained, i.e. typically between 10pA and 10nA [56].

Two scanning modes are generally used for the STM imaging process. One is constant current mode. The electric feed-back loop adjusts the tip height to maintain the designated value of the tunneling current. In this mode, the tip moves up and down according to the topography of the sample surface. The change of the applied voltage on the z piezoelement is used to produce the surface topographical image. The scan speed and the data acquisition in the constant current mode are limited by the finite response time of the feed-back loop to control the tip height. The second scanning mode is constant height mode, where the electric feed-back loop only monitors the variation of tunneling current without changing the tip height. The change of the tunneling current is used to produce the surface topographical image. In this way, scanning can be accomplished much more quickly than in the constant current mode. Because the tip moves without changing its height, the sample surface must be atomically flat in order to prevent crashing the tip into steps or other defects higher than atomic step height in constant height mode.

4.2 Deflection of Cantilever [60]

Consider a cantilever with one side clamped. Now, the cantilever is deflected by biaxial bending as shown in Fig. 4.4. The curvature of the cantilever,

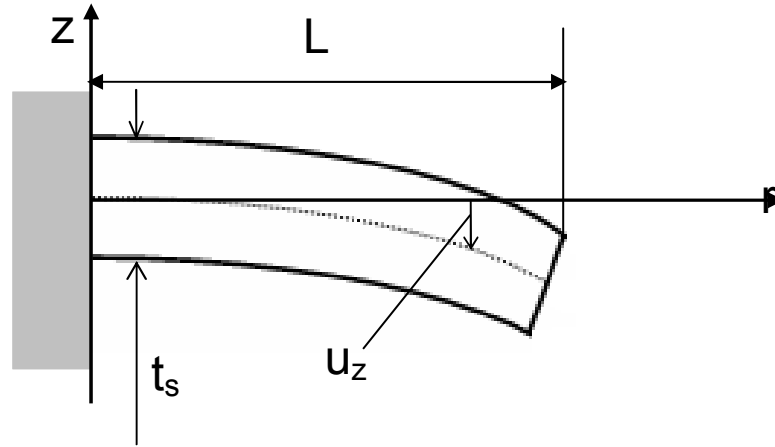


Fig. 4.4 Cantilever bending results in deflection, u_z . The left hand side of the cantilever is clamped. t_s and L are the thickness and the length of the cantilever, respectively.

K , can be taken as equal to $\frac{d^2 u_z}{dr^2}$ [61]. The bending of the cantilever due to the

biaxial bending moment (M) is [60]

$$\frac{d^2 u_z}{dr^2} = K = -\frac{(1-\nu) 12M}{E t^3} \quad \text{Eq. 4.2}$$

Integrating with respect to r gives

$$\frac{du_z}{dr} = Kr + C_1 \quad \text{Eq. 4.3}$$

Since $\frac{du_z}{dr}$ is equal to 0 at $r = 0$, C_1 is equivalent to 0. Further integration gives

$$u_z = \frac{Kr^2}{2} + C_2 \quad \text{Eq. 4.4}$$

Again, according to the boundary condition, u_z is equal to 0 at $r = 0$, making

C_2 equal to 0. As a result, the deflection equation becomes

$$u_z = \frac{Kr^2}{2} = -\frac{(1-\nu)}{E} \frac{6Mr^2}{t_s^3} \quad \text{Eq. 4.5}$$

Now, if the biaxial bending is associated with stress evolution during film growth on the cantilever, the biaxial bending moment along edge is

$$M = -\sigma_f t_f \frac{t_s}{2}, \quad \text{Eq. 4.6}$$

where σ_f is stress in the film and t_f is the film thickness. Finally, the deflection equation at $r=L$ is

$$u_z(r=L) = \frac{(1-\nu)}{E} \frac{3L^2}{t_s^2} \sigma_f t_f \quad \text{Eq. 4.7}$$

or

$$\sigma_f(r=L) = \frac{E}{(1-\nu)} \frac{t_s^2}{3L^2 t_f} u_z \quad \text{Eq. 4.8}$$

Based on the relation between u_z and σ_f in the equation, if the deflection u_z can be measured and other variables are known, the value of stress in the film can be calculated. The assumption in this relation is that the cantilever bends into the shape of a spherical shell [60]. To use this relation, the cantilever's length is at least more than three times of its width. Also, the thickness of the cantilever is significantly smaller than either dimension and also is less than substrate thickness.

4.3 Stress Measurements by STM

If the cantilever is used as the substrate for STM work, the height of the probe tip is affected by the deflection of the cantilever due to stress evolution in the film. Moreover, the vertical resolution of STM is good enough to detect cantilever deflection on a nanometer scale, giving the STM the capability of measuring stress evolution in the film while simultaneously visualizing changes in surface structure. The estimated resolution for the surface stress measurement is $0.1 \sim 0.01\text{N/m}$ due to natural oscillation of the cantilever [62], although the vertical resolution is $\sim 0.01\text{nm}$. In the case of the capacitance sensor, the resolution of displacement measurement is less than 1nm . This corresponds to a surface stress resolution of order 0.001N/m [28, 63].

Recently, Kinahan et. al. investigated oxidation of Si(111)-(7×7) surface using in-situ STM and surface stress measurement [64]. The cantilever of n-type Si (111) single crystal ($60 \times 5 \times 0.3\text{mm}^3$) was used as a substrate. With the aid of the capacitance sensor equipped in the STM system, they were able to show the change of (7×7) structure and the stress evolution during oxidation. Fig. 4.5 depicts the experimental setup with the cantilever and the capacitance sensor. Only one side of the cantilever was polished. This was to ensure the stress contribution on the unpolished side was negligible compared to the polished side [64]. The oxidation relaxes the tensile stress on the surface of Si(111)-(7×7). The results specifically explain that the oxidation at faulted subcells of the (7×7) structure relax the tensile stress to a greater extent than at unfaulted subcells.

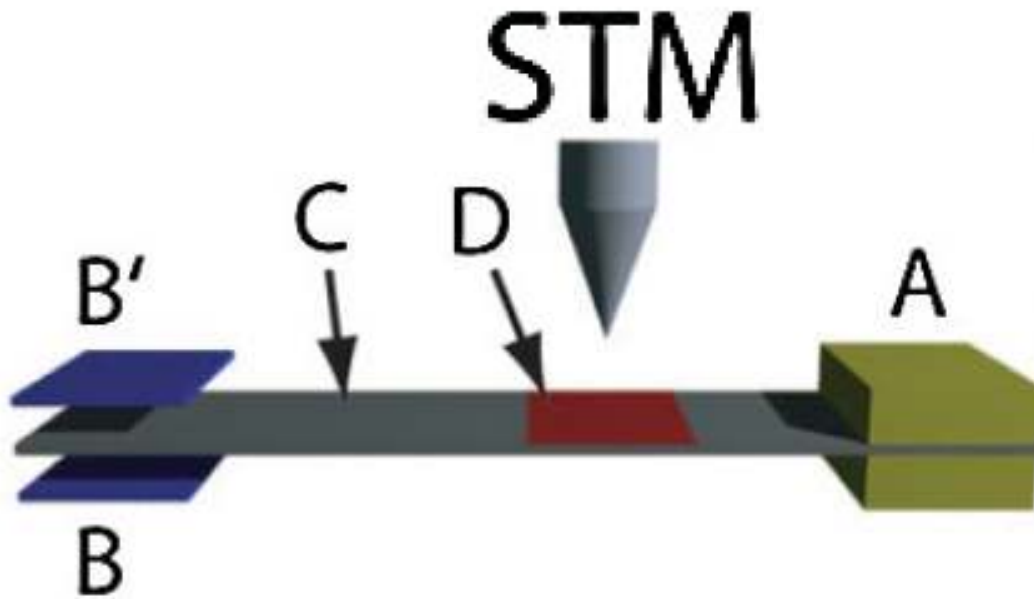


Fig. 4.5 Schematic of experiment setup [64]. The cantilever is clamped at side A. The free end of the cantilever is positioned between capacitance electrodes B and B'. One of the electrodes acts as a reference. The STM tip is engaged at the area marked with 'D' where the (7×7) structure is formed.

Chapter 5: EXPERIMENTAL PROCEDURE

5.1 Equipment Setup

5.1.1 Heating element

Both ring and coil type heating elements were designed for film growth at elevated temperatures as shown in Fig. 5.1. The temperature increase was better performed by the coil type element. In the ring design, the heating element consists of a tungsten filament wound in a ring shape and enclosed in two donut-shaped machineable glass-ceramic (MACOR) disks. These MACOR disks take on two roles. One role is to mechanically secure the tungsten filament; the other role is to occlude the ramp area of the STM sample holder from deposition.

The ramp area must remain clean because the ramp surface is used for the probe tip approach to the sample surface. Occlusion is achieved by allowing only the deposition flux to pass through the open area of the MACOR disks.

However, the amount of heat produced in this design is not enough to increase the sample temperature up to 400°C due to the spacing between the sample surface and the disk.

The second design incorporates a tungsten wire inside the sample holder as shown in Fig. 5.1(b). In this design, the filament's location just behind the sample permits effective heat transfer, thereby allowing the substrate to reach temperatures in excess of 400°C. However, this design cannot protect the ramp surface of the STM sample holder.

The deposited material should be removed from the ramp surface whenever the STM sample holder is removed from the chambers.

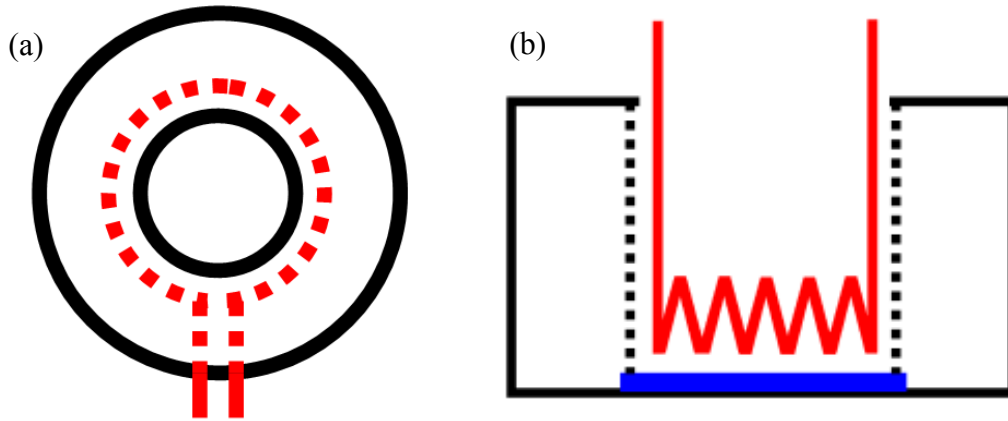


Fig. 5.1 Schematics of heating elements for elevated temperatures growth. (a) The ring type tungsten filament (red color) is enclosed in the Macor disks. (b) The cross-sectional view of the sample holder with the heating filament. In the drawing, the coil type tungsten filament (red color) is located behind the sample (blue color).

5.1.2 Design for the Small Deposition Source

Fig. 5.2 shows a schematic of the small deposition source and the range of deposition coverage on the substrate. The source material is attached to a tungsten filament. A deposition flux is generated by applying power to the filament, heating the source and causing it to evaporate. The deposition flux passes through two front pinholes made in the titanium foils, whose diameters are r_1 and r_2 . Assuming that the deposition flux comes from a point source behind the

hole r_1 , the areal coverage of deposition on the sample surface (related to R_1 and R_2) is manipulated by adjusting the parameters, r_1 , r_2 , d and D [7]. D and d are the distances from the first pinhole (r_1) to the sample surface, and from the first pinhole (r_1) to the second pinhole (r_2), respectively. R_1 corresponds to the area of the uniform deposition. R_2 is the radius of the maximum coverage. R_1 and R_2 are defined by Eq. 5.1 and 5.2, respectively [7].

$$R_1 = (r_1 \times D) / d + r_1 \quad \text{Eq. 5.1}$$

$$R_2 = [(r_1 + r_2) \times D] / d - r_1 \quad \text{Eq. 5.2}$$

R_1 must cover the entire surface area of the sample. The size of R_2 must be limited in order to avoid depositing on important functioning parts of the STM such as electrical wires, the piezo legs, and the center piezo tube that holds the probe tip.

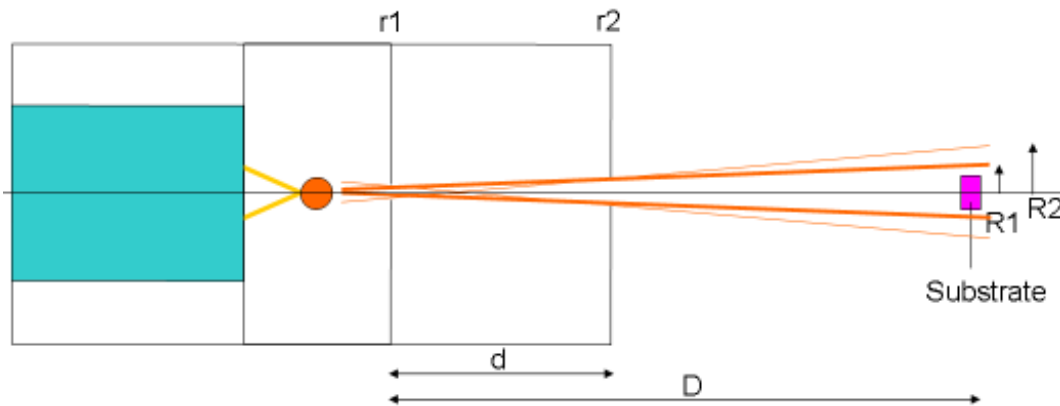


Fig. 5.2 The deposition source is inserted in the cylinder type enclosure made of stainless steel. Two titanium foils with center holes are located in front of the source material.

The second pinhole (r_2) has an oval shape that is elongated in the x direction to give the deposition flux a large area in the lateral direction of the cantilever and a small area in the vertical direction. The oval shape satisfies geometrical constraints, allowing the deposition to cover both cantilever and membrane substrates in lateral directions without spreading the flux too widely in the vertical direction, thereby protecting the STM's functioning parts. Because the deposition source is diagonally installed at an angle of 22.5° with respect to the stage, the projected deposition flux can cover the entire surface of the sample, even though the size of r_2 in the y direction is small. The determined parameters are explained in Table 5.1.

Table 5.1 The dimensions of parameters in Eq. 5.1 and Eq. 5.2 (unit: mm)

r_1	r_2		d	D	R_1		R_2	
	x	y			x	y	x	y
0.33	1.52	0.38	29.97	46.48	2.17	1.07	2.52	2.02

The source material is initially attached to the filament by bending a wire around the filament into a ribbon shape as seen in Fig. 5.3(a). The source is more securely attached by resistively heating the tungsten wire, melting the source material so that it forms a ball (Fig. 5.3(b)).

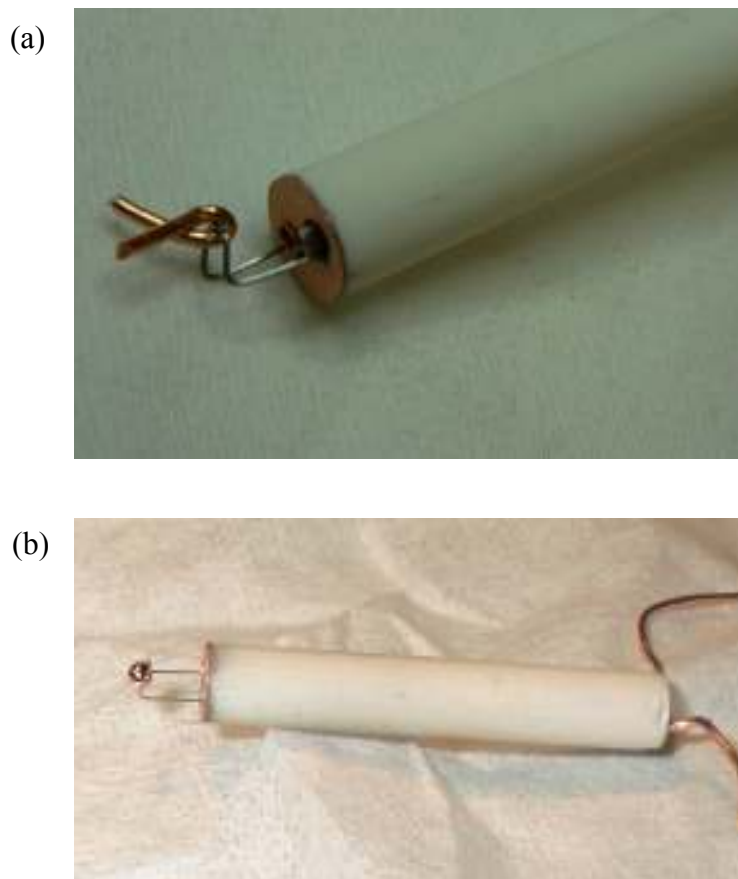


Fig. 5.3 (a) Initial attachment of source material (in a ribbon shape) to the tungsten filament. (b) Ball shape of the source material after resistive heating the tungsten filament.

As shown in Fig. 5.4, the deposition source was inserted into a cylinder type enclosure. The enclosure was aligned to target the center of the STM with the use of a laser. For the alignment process, the laser was attached to the back side of the enclosure instead of the deposition source unit.



Fig. 5.4 A cylinder type enclosure of the deposition source is aiming to the center of the STM stage. The deposition source unit is inserted into the back side of the enclosure. The STM sample holder is not shown in the picture.

5.1.3 STM system (RHK Technology)

The STM stage consists of a STM head and sample holder from RHK technology and was modified to perform advanced capabilities of in-situ deposition, a shuttering system for “on/off” switching of the deposition flux as well as stress measurement. Fig. 5.5 shows the modified STM system. The Beetle type STM head (top) and sample holder (down) are shown on the right hand side of the picture. The STM head has a center piezoelectric tube that holds the probe

tip and three piezoelectric legs with sapphire spears at the ends. The piezoelectric legs can “walk” along the ramp surface of the sample holder. The “walking” process is realized by bending and straightening of the piezoelectric legs, which results in shifting their positions due to the moment of inertia of the STM head. By “walking” the legs in a rotational mode, the center piezoelectric tube can approach the sample or retreat from it. The sample is located in the center of the sample holder. The cylinder type enclosure of the small deposition source is shown in the upper middle of the picture.

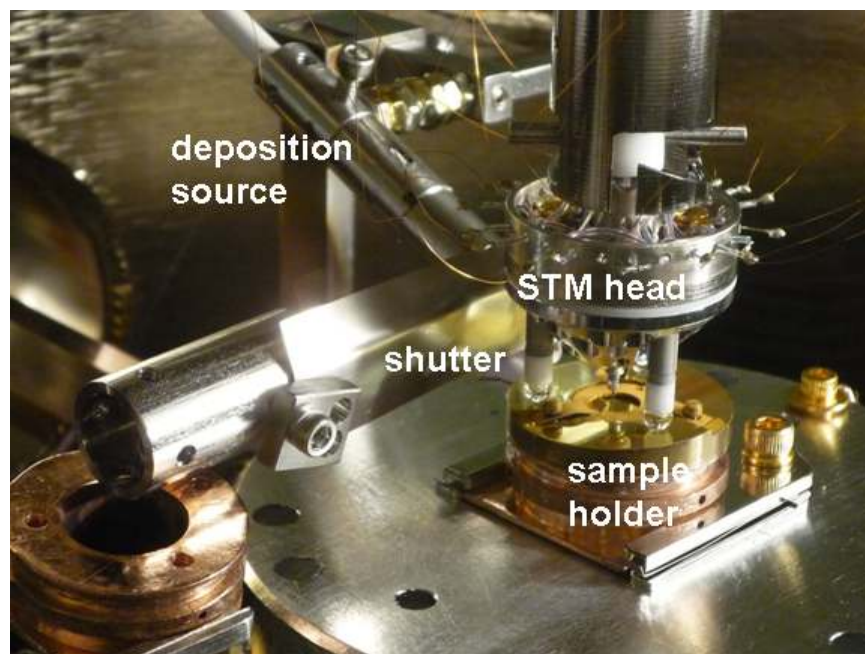


Fig. 5.5 The completed setup of STM system for the advanced capabilities that are used to measure the stress evolution and obtain the STM topographies of sample surfaces during the deposition of the films.

The deposition flux shutter is located between the deposition source and the STM stage, which is shown in the center of Fig. 5.5. The shutter is made of 0.05mm thick Ti foil and slides in (out) to stop (start) the deposition flux. During the deposition, the shutter also serves to minimize the amount of heat transferred from the deposition source to the sample. This was accomplished via an oval shaped hole made in the center. Deposition starts when the hole is aligned with the deposition flux while radiative heating from the deposition source is minimized.

5.1.4 UHV Chambers

As described in Fig. 5.6, two main chambers, the preparation chamber and the STM chamber, are connected as one experimental system. In order to isolate the STM system from mechanical vibration, miniature sleeve style air springs support both UHV chambers. The chambers are always maintained in ultra high vacuum conditions except for during occasional maintenances. They are equipped with commercially available apparatuses as well as various custom designed experimental tools. A load lock system was installed next to the preparation chamber. Once the load lock system accepts a sample, a mechanical pump brings the load lock to a high vacuum condition of 2×10^3 torr. The load arm transfers the sample from the load lock system through the preparation chamber to the STM chamber. The sample and probe tip transfer mechanism relies on the use of a fork-style transfer unit attached to the end of the load arm so that holders of either the

sample or the probe tip can be transferred at the same time. The UHV condition of $\sim 6 \times 10^{-9}$ torr in the preparation chamber is obtained by a turbo molecular pump (Pfeiffer Vacuum). The e-gun system (Thermionics Vacuum Products, 3kW) provides the deposition flux of thermally evaporated source material that is contained in a graphite crucible (1.5cc).

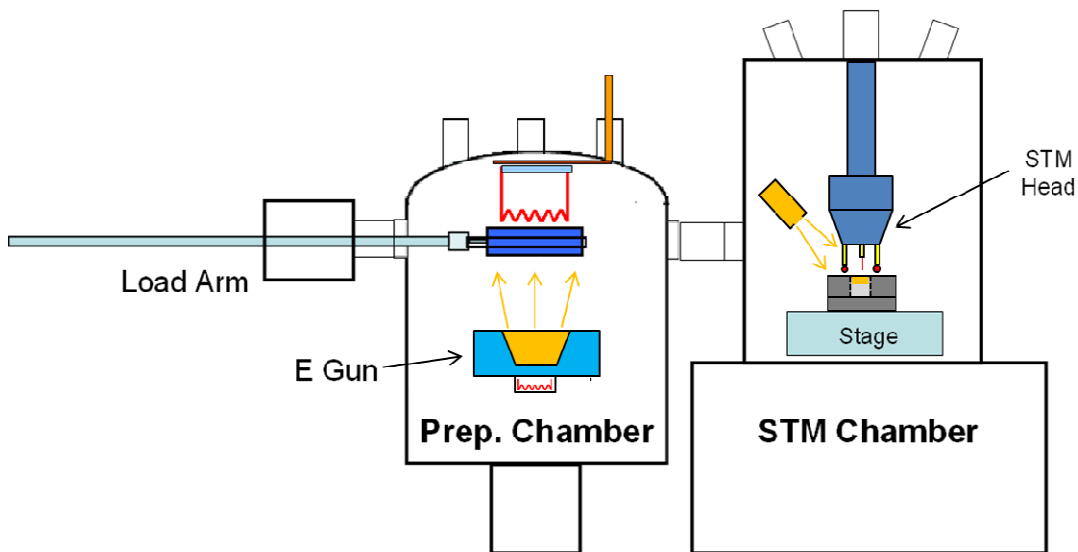


Fig. 5.6 The UHV chambers are composed of the preparation chamber for cleaning and depositing of samples and the STM chamber that is involved in surface imaging and measuring stress during film growth. The two chambers are separated by the gate valve so that the prepared sample can be transferred by the load arm to the STM chamber without exposing the sample to the atmosphere. The load lock system, on the left hand side of the figure, protects the preparation chamber from an atmospheric contamination when the sample is inserted from outside.

The heating filament is made of the 0.006" tungsten wire and connected to the electrical feedthrough system (MDC vacuum). The filament is attached to a linear motion feedthrough (MDC vacuum) so that the filament can be either lowered and located behind the sample for film growth or raised up to allow the load arm to transfer the sample.

The STM chamber has a combined titanium sublimation pump and ion pump which can maintain a base pressure of 5×10^{-10} torr. The remaining gas species were monitored by the residual gas analyzer (RGA) system (Stanford Research Systems, RGA200). A wobble stick was installed in the STM chamber to transfer the sample or the probe tip from the load arm to the STM stage. The wobble stick has a duplicate of the fork style transfer units that are attached to the load arm. Extra samples or probe tips can be stored in a carousel type storage which was custom designed and located near the STM stage. The sample and the probe tip can either be used immediately or stored in the carousel which is capable of holding up to five sample or probe tip holders.

5.2 Experimental Details

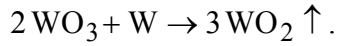
5.2.1 Tip Preparation

0.01" tungsten (W) or platinum-iridium (PtIr) wires are generally used to make probe tips. Both kinds of wire are electrochemically etched to obtain atomically sharp tip ends. The W wire is 2~3mm dipped into 1M NaOH aqueous solution. Adding 150 μ l of ethanol to 80ml of NaOH solution increases the quality of the tip. A stainless steel wire is used as the counter electrode. The W wire itself

act as the working electrode. An AC $\sim 6.5\text{V}$ potential is applied to the circuit. The electrical circuit opens when etching is completed. The PtIr tip is made in a similar way using a diluted CaCl_2 solution with applied AC potential of $\sim 19\text{V}$. The diluted CaCl_2 solution is prepared by mixing a saturated solution of CaCl_2 with water in a ratio of 1:2.

The surface of the W tip has a naturally formed oxide layer (WO_3) that should be removed to acquire atomic resolution STM images. A “flash annealing” process, involving resistive heating by a W filament, is used to remove the oxide layer. The tip is spot welded on a W filament that is connected to two electrodes. A metal plate is located in front of the tip, where the spacing between the tip and the plate is $\sim 5\text{mm}$. After the flash anneal, a high voltage ($200 \sim 900\text{ V}$) is applied between the tip and the plate. If the current between them is 20nA in the $200\sim 300\text{V}$ range, the tip condition is estimated to be sufficient for atomic resolution STM images. The oxide removing system is put into a high vacuum condition up to 1×10^6 torr. A DC power is applied to increase the temperature of the tip to around 800°C . If the temperature is too low, the oxide layer is not completely removed. On the other hand, if the temperature is too high, the tip becomes blunt. Because of this, the time for applying power to the tip needs to be carefully controlled. The tip annealing time is around several seconds. Once the oxide layer is completely removed, the tip is removed from the vacuum chamber and detached from the W filament. The oxide-free tip must be quickly transferred to the UHV- STM system in $\sim 20\text{min}$ to prevent oxide layer regeneration. At room

temperature, WO_3 is thermodynamically stable. However, at higher temperatures (more than 725°C) the following reaction occurs [53]:



Since WO_2 sublimates at about 800°C [53], “flash annealing” at high temperatures leaves an oxide free W surface.

5.2.2 Sample Preparation

Reconstruction of the Au(111) surface occurs during Au growth carried out at elevated temperatures of $250\sim 430^\circ\text{C}$. The Au films were grown on three types of deflectable substrates: SiN membrane, glass cantilever and mica cantilever.

5.2.2.1 Au on SiN Membrane

The dimensions of a commercial SiN substrate (Norcada) are $5\text{mm}\times 5\text{mm}$, with a $1\text{mm}\times 1\text{mm}$ square window in the center. The thickness of the SiN membrane is $100\mu\text{m}$. The Au growth process consisted of seed layer growth (20nm) at room temperature followed by the first main layer deposition (130nm) and the second main layer (150nm) deposition at 430°C . The deposition rate for all of the Au growth processes was $1.0\text{\AA}/\text{s}$. After the first main layer growth, the sample is removed from the chamber to build an electrical contact between the STM sample holder and the grown Au surface. This step is necessary for the STM system to obtain the tunneling current between the probe tip and the sample surface in the STM sample holder. The deposit thickness was monitored by a

quartz crystal microbalance (QCM) that is calibrated via atomic force microscopy (AFM).

5.2.2.2 Au on Glass Cantilever

A 30 μm -thick borosilicate glass (SCHOTT D 263TM T) was used as the cantilever substrate. The glass slides were cut into the cantilever with a diamond-tipped scribe (Lunzer, Inc. Omniscrite). The dimensions of the cut-out glass cantilever were approximately 0.5mm \times 4mm. The Au(111)-(22 \times $\sqrt{3}$) film was grown on the clean glass cantilever that was clamped in the STM sample holder. The grown film layer was composed of a Cr adhesion layer (10nm), a Au seed layer (50nm), the first Au (200nm) and the second Au main (200nm) layers. The deposition rate for every growth process was 1.0 \AA /s. The Cr adhesion layer and the Au seed layer are grown at room temperature, while the two main layers are grown at $\sim 250^\circ\text{C}$. Before growing the second Au main layer, the cantilever was slid into the clamping area by 2mm to build the electrical contact between the cantilever and the STM sample holder.

5.2.2.3 Au on Mica Cantilever

The mica cantilevers were cut out from SPI Supplies' muscovite mica substrate (grade V-5) after cleaving to obtain a clean surface. The dimensions of the mica cantilever were 4mm \times 0.8mm \times 0.04mm. Due to the limited area of the stage of the STM system, the width of the cantilever must be smaller than 1mm. A simple cutting method, such as scissors, cannot form a mica cantilever that is

sufficiently narrow in width because the width of the deformed area associated with scissor cutting is around 1mm. In order to minimize the deformed area, an alternative press cutting method was used. A sharp razor blade was perpendicularly placed on the cleaved mica substrate. Impacting the back side of the razor blade separated the narrow cantilever from the mica substrate resulting in a deformed width less than 0.2mm. The mica cantilever was clamped in the STM sample holder in the same way as the glass cantilever. The Au growth consisted of a seed layer growth (5nm) with a deposition rate of 0.1Å/s followed by the first main layer deposition (145nm) and the second main layer (100nm) with an increased deposition rate of 0.2Å/s. The growth temperature for every growth process was 300°C. The electrical contact between the cantilever and the STM sample holder was established in the same way as the glass cantilever (by sliding the cantilever into the clamp before the second main layer growth).

5.2.3 STM Imaging

The location of the probe tip on two different substrates of SiN membrane and miniature cantilever was observed through a microscope as shown in Fig. 5.7. The lateral movements of the piezoelectric legs could precisely manipulate the position of the probe tip on the small membrane area (1mm×1mm) and the narrow width of the miniature cantilever (~0.8mm). The sample was positively biased allowing the electron to enter the empty states of the sample from the probe tip.

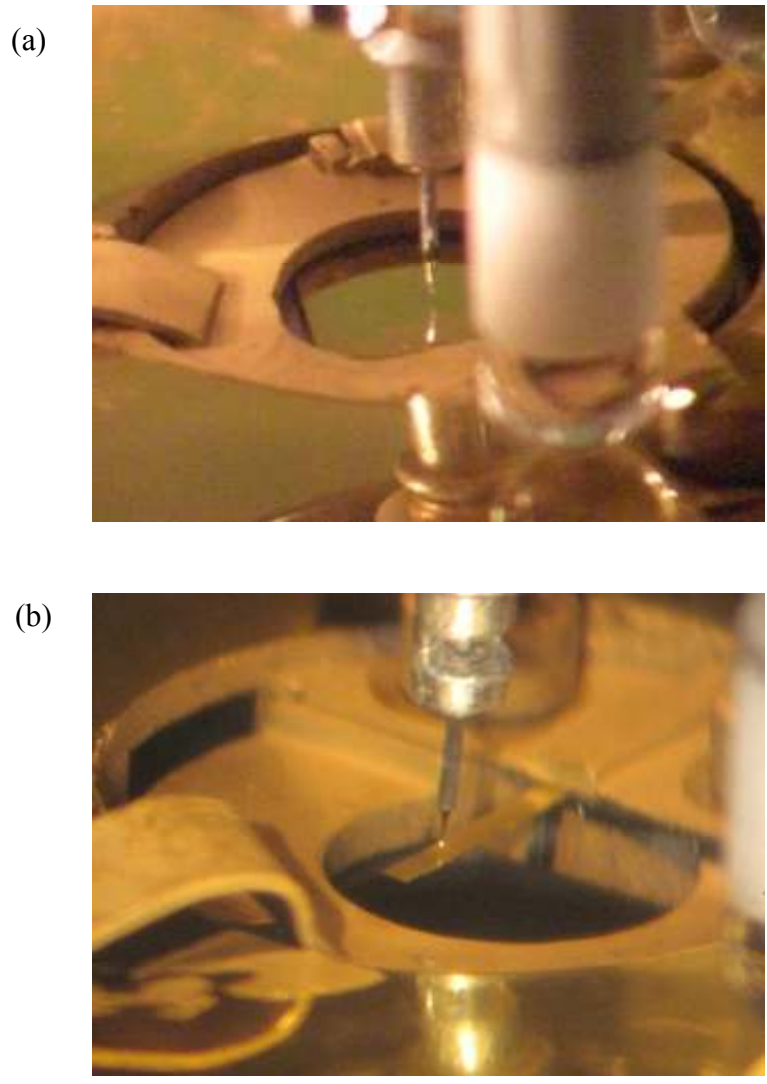


Fig. 5.7 Optical microscope images for STM probe tips on two different substrates, SiN membrane and glass cantilever (magnification: $\sim 10\times$). (a) The tip is located at the center of the SiN membrane substrate. (b) The tip is located at $\frac{3}{4}$ of the cantilever length from the clamp.

In typical scanning parameters, the tunneling current is 0.2~ 0.5nA, and the bias is +0.5V.

5.2.4 *In-Situ* Cu Deposition

Ultrathin Cu films were deposited on Au(111)- $(22 \times \sqrt{3})$ at room temperature using the small evaporative source in the STM chamber. The Cu coverage was estimated using STM images after Cu growth was completed. Two different groups of STM images were used for coverage estimation. The first group of the STM images was originally obtained where the probe tip was engaged during *in-situ* Cu deposition. The second group was obtained after Cu deposition at several different locations at least 1mm away from the original location. This method was used to see if the probe tip causes any variation in the Cu coverage along the sample surface.

As a result, the coverage difference between the initial area and other locations was estimated to be less than 0.1ML. The coverage difference resulted from a “shadowing” effect of the STM probe tip against the deposition flux [65]. The “shadowing” effect was minimized by increasing the incident angle (67.5°) of the deposition flux as much as possible so that it could pass near the apex of the probe tip. The general Cu deposition rate was 0.03~0.25 ML/min. Figs. 5.8 and 5.9 show the STM images of the Cu adlayer, obtained at two different locations, which are the original location during *in-situ* Cu deposition and a different location after Cu deposition.

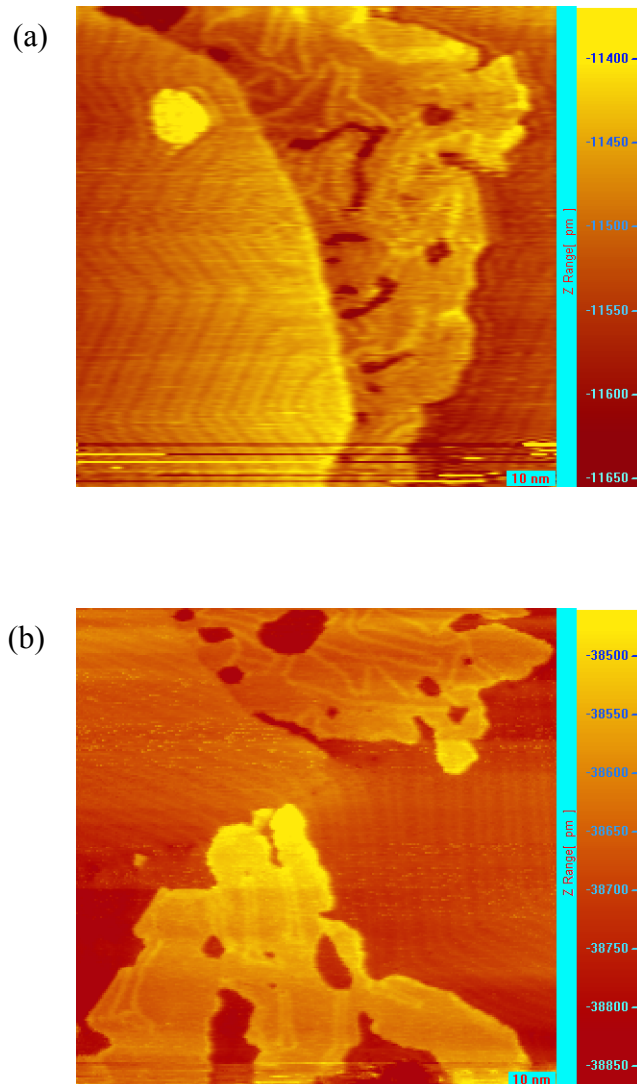


Fig. 5.8 STM images ($100\text{nm}\times 100\text{nm}$) of $0.3\text{ML Cu/Au}(111)-(22\times\sqrt{3})$ obtained at two different locations. (a) STM image of the original location, obtained during *in-situ* Cu deposition. (b) The probe tip was moved from the original location after Cu deposition and re-engaged at a different location.

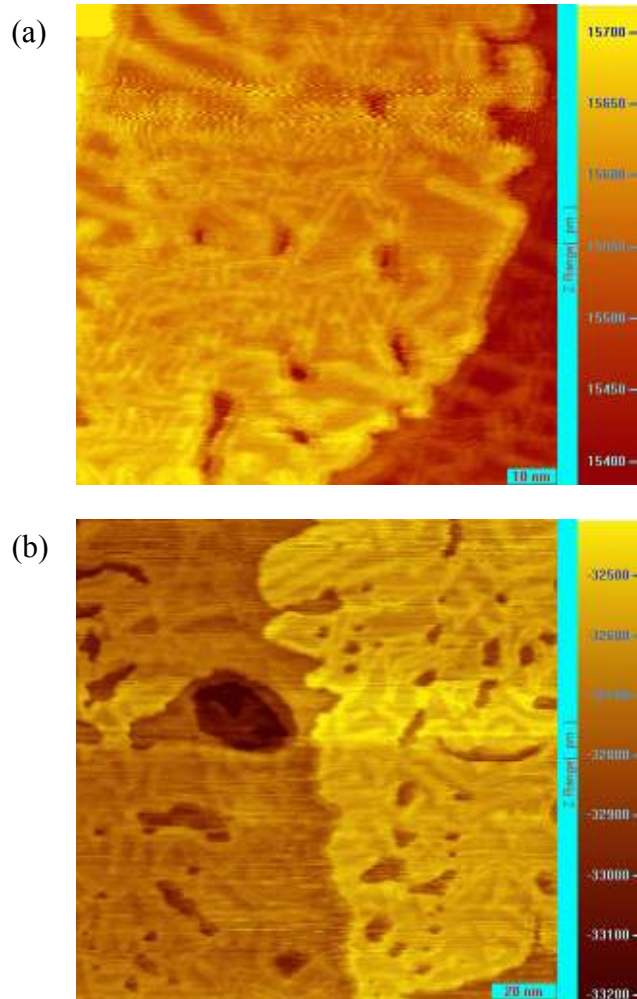


Fig. 5.9 STM images (100nm 100nm) of 1.0ML Cu/Au(111)- $(22 \times \sqrt{3})$ obtained at two different locations (in the same way as Fig. 5.8) of (a) the original location and (b) a different location.

The Cu coverages for Figs. 5.8 and 5.9 are approximately 0.3ML and 1.0ML, respectively. Each figure set shows almost the same Cu coverage in its two STM images (Fig. 5.8 (a) and (b), and Fig. 5.9 (a) and (b)), implying that the “shadowing” effect was minimized.

5.2.5 Stress Measurements

The deflection of the substrate is detected by the probe tip through the height displacement associated with the change in applied voltage on the z piezoelement of the piezoelectric tube that holds the probe tip. The ratio between the height displacement and the change in applied voltage is a piezo constant [53]. The piezo constant was experimentally determined by comparing the probe tip height and the applied voltage that were monitored during STM imaging and stress measurement.

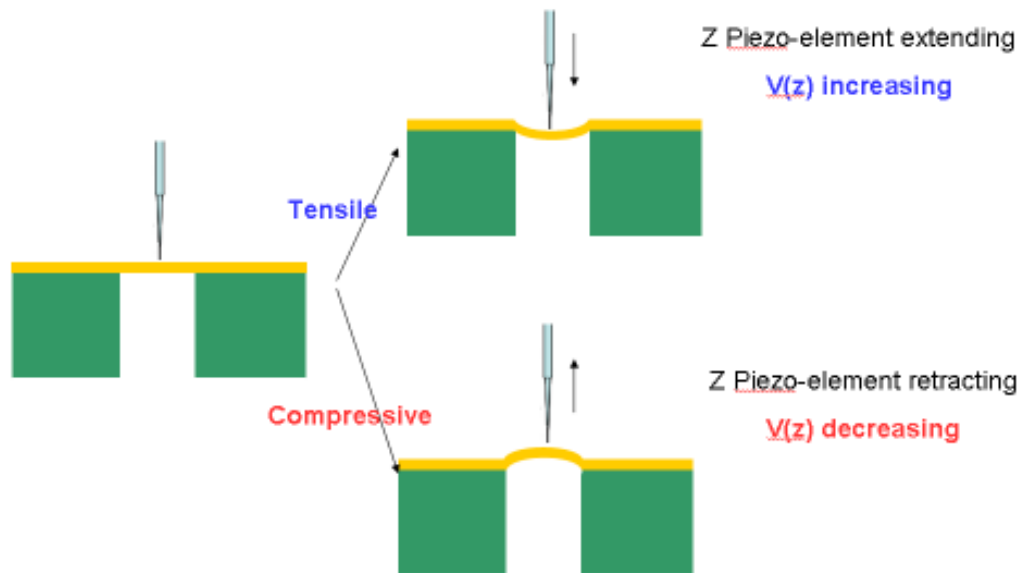


Fig. 5.10 Change of STM probe tip height in response to the stress in the film on the membrane substrate. The probe tip extends (retracts) for the tensile (compressive) stress.

The piezoelements extend (retract), when the applied voltage increases negatively (positively) according to the system setting of RHK STM. In the case of cantilever substrates, the tensile stress is associated with retraction of the z piezoelement. For example, if the deflection of the cantilever raises the probe tip due to generation of the tensile stress, this results in a positive increase of the corresponding applied voltage. However, the tensile stress on the membrane substrates is associated with extension of the z piezoelement. As the film on the membrane tends to contract under conditions of tensile stress, the membrane should deflect in a “convex down” manner, as shown in Fig. 5.10. This membrane deflection induces the extension of the probe tip in order to maintain the designated tunneling current between the tip and the membrane substrate.

5.2.6 Verification of *in-situ* Cu deposition for STM imaging and Stress measurements

In order to verify the ability of the *in-situ* deposition source to provide a consistent Cu deposition rate for experiments, three independent sets of experiments were designed. The first set comprised STM imaging only, without monitoring stress evolution using a bulk mica substrate. The second set consisted of stress measurements without scanning the surface while the probe tip was stationary. The final set involved simultaneous STM imaging during stress evolution monitoring. The electrical power applied to the deposition source was equally maintained for all three sets of experiments in order to keep the deposition rate as constant as possible.

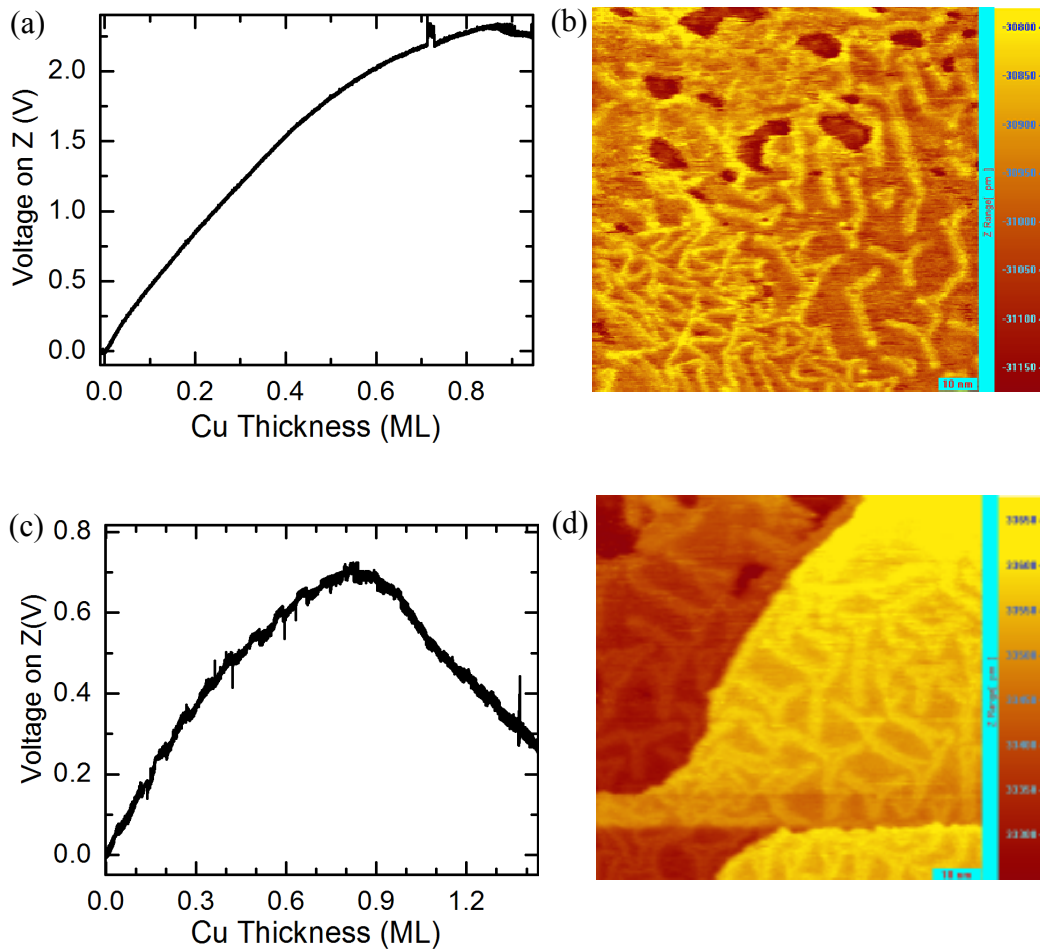


Fig. 5.11 (a) Stress evolution during Cu deposition with a stationary STM probe tip, no surface imaging. (b) STM image of 0.9ML Cu obtained with a bulk mica substrate (100nm×100nm). (c) The stress evolution during Cu deposition while STM imaging. (d) One of the STM images (Cu coverage: 0.9ML) obtained during in-situ stress measurement and imaging of (c) (80nm×80nm).

While the first set of experiments used a bulk mica substrate, the other two sets used mica cantilevers. The surface of Au(111)-($22 \times \sqrt{3}$) on mica cantilever (Fig. 5.11(d)) generated smaller terrace sizes compared to Au(111)-($22 \times \sqrt{3}$) on bulk mica substrates (Fig. 5.11(b)). This difference may be attributed to mica cantilever preparation by the press cutting method (Chapter 5.2.2.3) which produces deformation at the edge of the mica cantilever. Because the width of cantilever is only ~ 1 mm, the center of the mica cantilever is close enough to the deformed edge to produce the variation. Therefore, STM scanning with a bulk mica substrate provided better and more stable surface images. The second independent set of experiments measured stress without scanning the surface in order to avoid artifacts. If the probe tip remains stationary during *in-situ* deposition, the change in the probe tip height mainly results from stress-induced cantilever deflection. However, if the tip is scanning the surface, “noisier” plot of stress evolution are produced (Fig. 5.11(c)) due to artifacts from the imaging process. The combined results of these two independent sets of experiments (Fig. 5.11 (a) and (b)) were in agreement with the *in-situ* stress and structure evolution experiments (Fig. 5.11 (c) and (d)). Both cases showed a peak near 0.9ML in the stress plots as shown in Fig. 5.11 (a) and (c). STM images of Cu at coverage of about 0.9ML are shown in Fig. 5.11 (b) and (d). However, the change in probe tip height of Fig. 5.11(a) is larger than that of Fig. 5.11(c). This may be attributed to a difference in the length of the W tip for each experiment set.

5.2.7 Problems with SiN Membrane Substrates

Unfortunately, several attempts to obtain stress measurements with the membrane substrates did not give consistent results of stress evolution associated with Cu film growth. The stress evolution results did not show a clear sign of the stress relaxation associated with surface structure formation. For example, Fig. 5.12 shows the tensile increase in stress evolution and STM images of Cu adlayers. The stress evolution was obtained simultaneously with STM imaging of the surface during *in-situ* Cu deposition. While Cu coverage increases, the tensile stress in Cu films is expected to relax, resulting in corresponding surface structure formation. However, the stress evolution did not show any considerable slope change in the plot of Fig. 5.12(a) which might indicate the stress relaxation. In order to determine if this was a result of membrane buckling due to Au film growth, another Au film was grown on the back side of the membrane using the same growth recipe. The back side growth was expected to compensate for the growth stress effect of the Au film on the front side of the membrane. After repeating the experiment using the membrane with this modification, the results did not exhibit the expected behavior and the stress-structure relation remained unclear.

The second method of solving this problem was the use of a SiN cantilever fabricated from a SiN membrane by means of focused ion beam (FIB) milling. Fig. 5.13(a) shows the result of the FIB cut on a SiN membrane for cantilever fabrication.

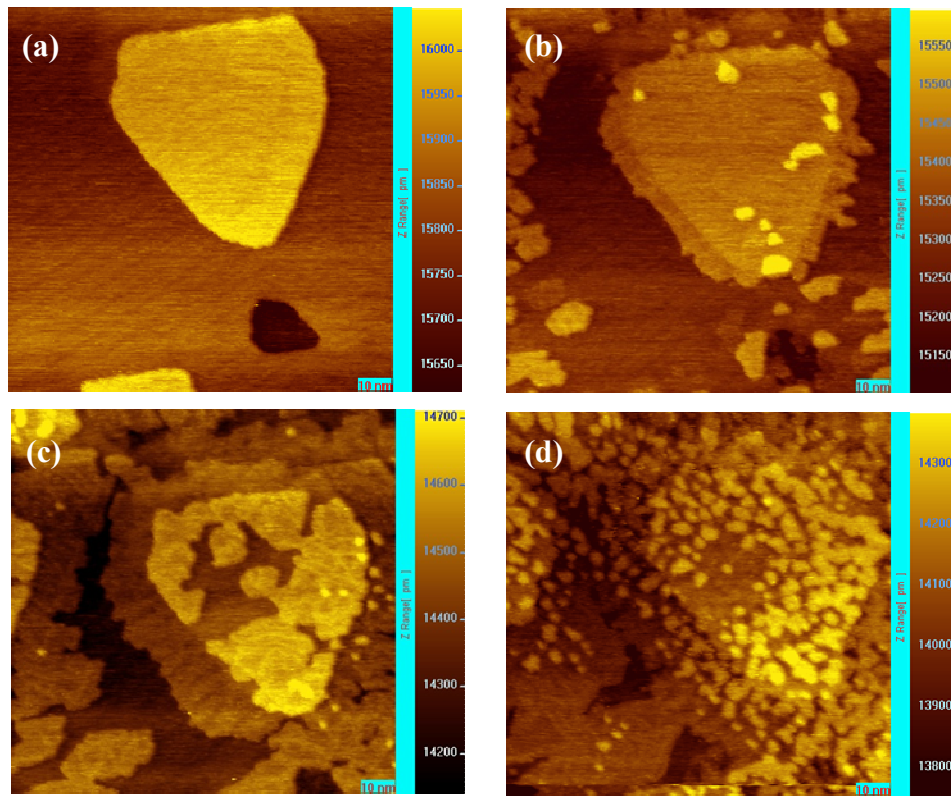
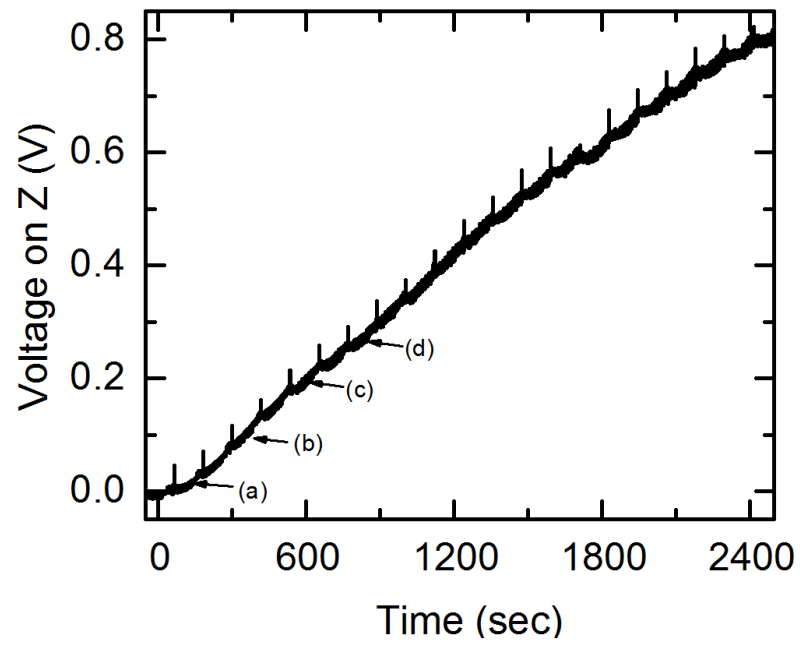


Fig. 5.12 Stress and structure evolution with SiN membrane substrate. The stress measurements were conducted during STM imaging. The repeating segment in the plot corresponds to each STM image (100nm×100nm).

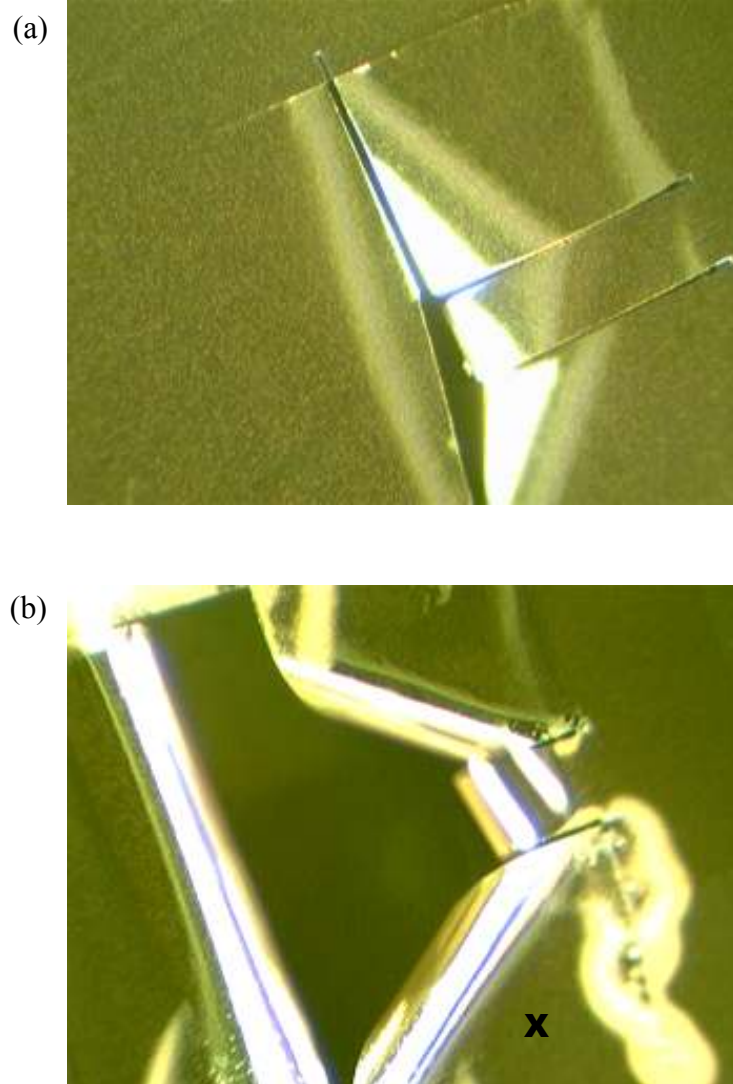


Fig. 5.13 Optical microscope images ($\times 80$) of Au(111) on SiN membrane. (a) The cantilever ($0.14\text{mm}\times 0.45\text{mm}$) is shown on the right hand side of the picture. (b) The cantilever and the two other rectangles were curled up due to the subsequent Au(111) growth.

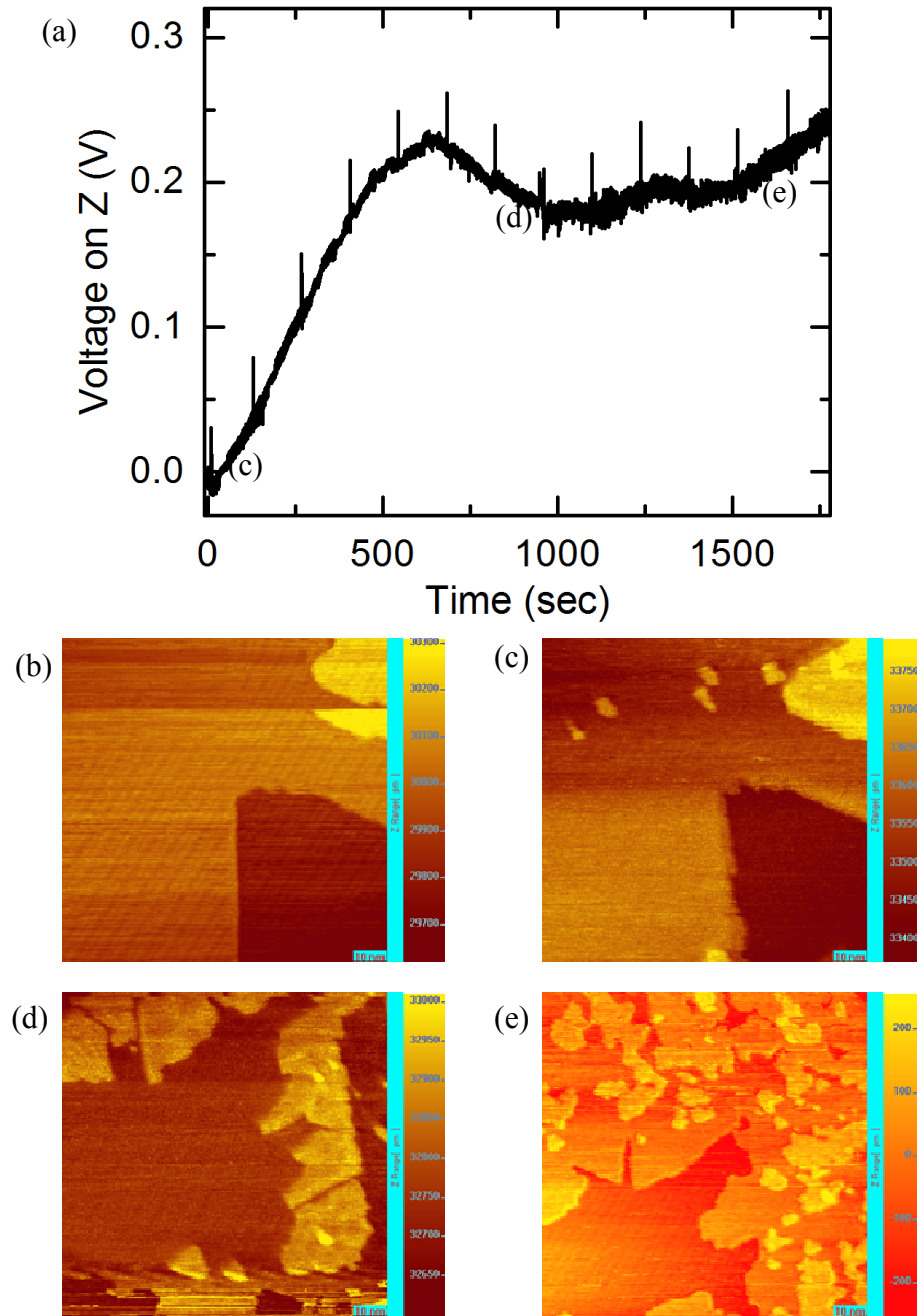


Fig. 5.14 (a) Stress evolution during Cu deposition with simultaneous STM imaging. (b) Bare surface of Au(111)- $(22 \times \sqrt{3})$ (100nm \times 100nm). (c)~(e) Cu coverages for each image are 0.1ML, 0.5ML and 1.1ML, respectively.

After FIB processing of the membrane, another Au(111) layer was grown on the fabricated cantilever to provide a fresh reconstructed surface for the experiments. However, the Au(111) growth caused the cantilever to curl up as shown in Fig. 5.13(b). Because the fabricated cantilever was unusable, an experiment was conducted on the relatively flat area marked with the “X” in Fig. 5.13(b). As a result of this experiment, Fig. 5.14 shows a stress evolution with a tensile stress increase, followed by a stress relaxation and another tensile stress increase during the Cu growth. This result, which was consistent with our expectations, had not been attained in previous experiments with membrane substrates. Unfortunately, because the geometry of the area corresponding to this stress was not well defined (owing to the “curling up”), a specific calculation of the amount of stress was not possible. It was hypothesized that the lack of well defined results with the membrane substrate may have been due to a small signal to noise ratio. Specifically, the height signal of the probe tip associated with membrane deflection might not have been large enough to resolve during the Cu growth on the reconstructed Au(111)/SiN membrane.

5.2.8 Thermal Effects

Because the deposition flux is generated from thermal evaporation of the source material, it is possible that heat from the deposition source could induce thermal expansion of the STM sample system, i.e. the probe tip, substrate, and piezoelements that compose STM legs and the center scanning tube. In that case, the probe tip response would represent stress evolution due to both deposition and

thermal expansion. Thus, three types of experiments were performed to investigate thermal effects on the stress measurements on a SiN membrane. The first experiment to explore the thermal effect was performed with the probe tip location on the SiN substrate away from the membrane window, monitoring the change of the probe tip height during Cu deposition.

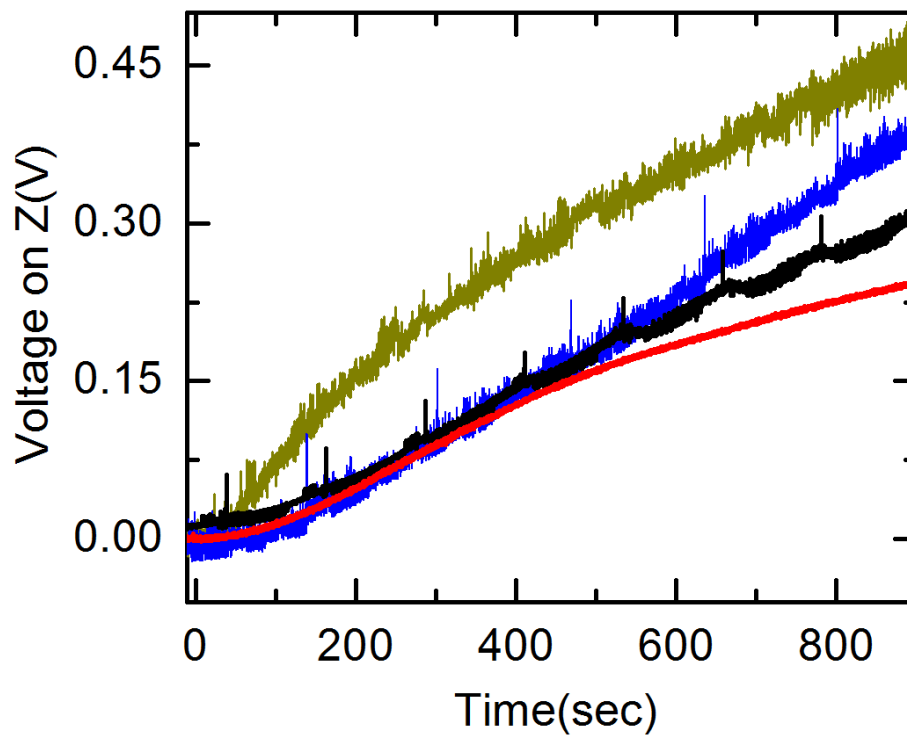


Fig. 5.15 The change in the probe tip height according to Cu deposition out of the membrane (blue), resistive heat of filament only (red), external light (orange) and Cu deposition on the membrane (black).

Second, an experiment was executed by measuring the deflection of the membrane due only to resistive heating of the filament without source material. The third experiment was performed using an external light source to increase the temperature in the STM system, while the change of the probe tip height was monitored. For the last two experiments, the tip was located in the center of the membrane. The results were compared with the stress evolution plot obtained during Cu deposition. According to the results as shown in Fig 5.15, there was no significant difference between in the changes in the height of the probe tip due to thermal effects and due to membrane deflection by Cu deposition. The plot for membrane deflection due to Cu deposition (black curve) is aligned, in the early stage (~400sec), with the other two plots which correspond to Cu deposition away from the membrane window (blue curve) and to resistive heating only (red curve), respectively. Therefore, it was more likely for heat to affect a change in probe tip height than for stress evolution to do so.

In the case of the cantilever, it was expected that the cantilever might deflect enough to overcome the heat effect. In order to extract the stress signal due to possible thermal effects, a set of experiments with cantilevers, similar to those performed on the membrane substrate, were carried out. Fig. 5.16 shows schematics of the experiments in two sets, where (1) the height of the probe tip changes due to heat only (Fig. 5.16(a)) and (2) the combination effect of the Cu deposition and the heat (Fig. 5.16(b)) were recorded. The electrical power on the deposition source in both cases was equivalent. Thus, the stress evolution

associated with Cu deposition was obtained from the difference in the change of probe tip height ($U_z' - U_z$).

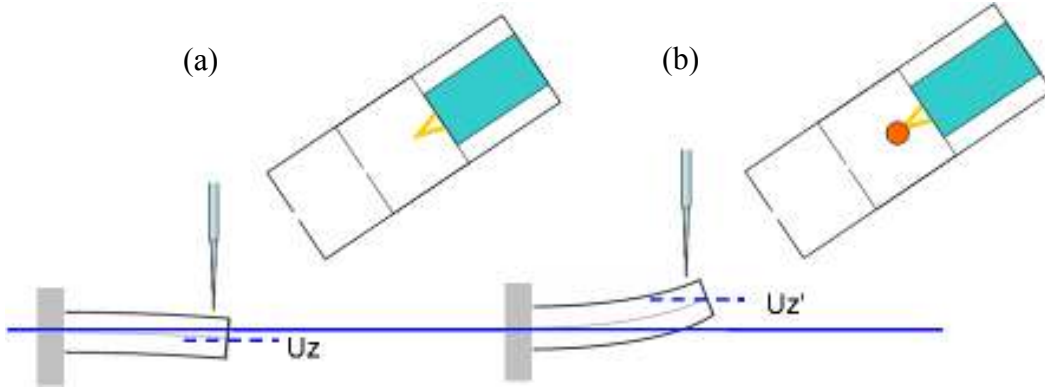


Fig. 5.16 Schematics of experiments to screen the thermal effect on glass cantilever. (a) The cantilever deflects due to heat only without deposition source. (b) The cantilever deflects by stress evolution associated with Cu deposition from the deposition source and the heat effect.

5.2.9 Validity of the Glass Cantilever for Stress Measurements

The thickness of Au (111) on the glass cantilever is 460nm, which may be too thick to use the Stoney relation for stress measurements. The glass substrate that is used in the experiments has the thickness of 30 μ m, the density of 2.51g/cm³ and the biaxial modulus of 92GPa. The thickness of Au(111) is more than 1% of the glass thickness. Also, the biaxial modulus of Au is 139GPa, which is larger than that of the glass. The Stoney relation for stress measurement is limited by both the thickness and the stiffness of the film, unless the thickness of the substrate is much larger than the film [8].

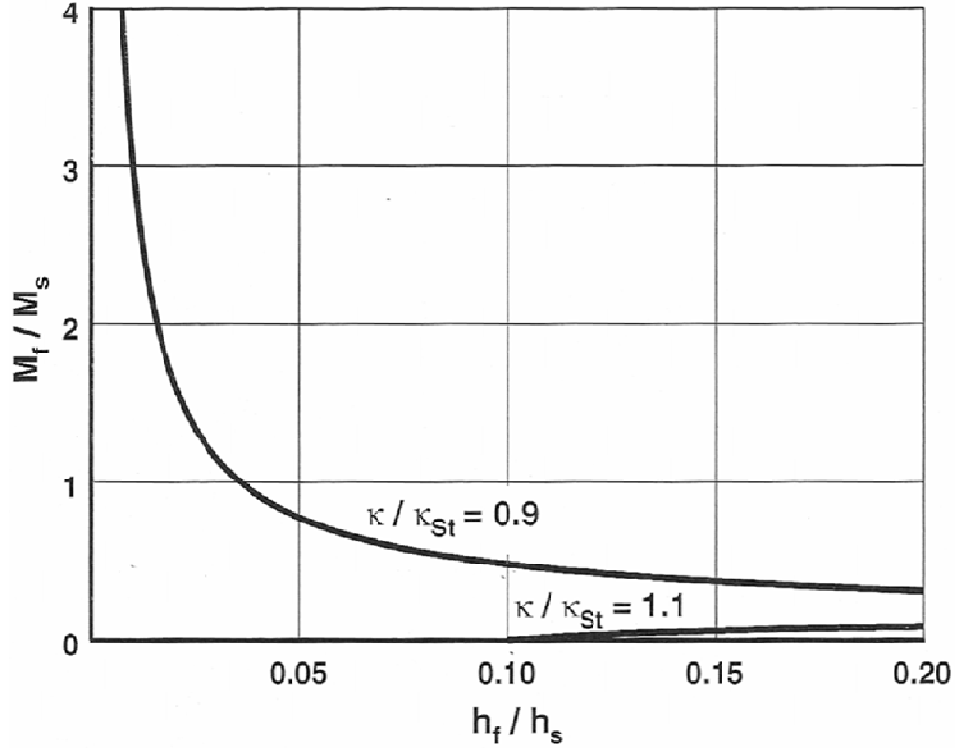


Fig. 5.17 The two curves, corresponding to Eq. 5.3, represent 10% error boundaries in substrate curvature calculation with the Stoney relation for any values of h_f/h_s and M_f/M_s . The region bounded by the two curves and the coordinate axes, therefore, has less than 10% error in the Stoney relation [7].

Eq. 5.3 was used to check the range of the error in the stress measurement using the glass substrate with the Au(111) film [8],

$$\frac{\kappa}{\kappa_{St}} = \left(1 + \frac{h_f}{h_s} \right) \left[1 + 4 \frac{h_f}{h_s} \frac{M_f}{M_s} + 6 \frac{h_f^2}{h_s^2} \frac{M_f}{M_s} + 4 \frac{h_f^3}{h_s^3} \frac{M_f}{M_s} + \frac{h_f^4}{h_s^4} \frac{M_f^2}{M_s^2} \right]^{-1}, \quad \text{Eq. 5.3}$$

where κ is the curvature of the cantilever considering the film thickness effect, κ_{St} is the curvature by the Stoney relation, h_f is the thickness of the film, h_s is the

thickness of the substrate (or cantilever), M_f is the biaxial modulus of the film, and M_s is the biaxial modulus of the substrate. After plugging in the parameters,

$$\frac{\kappa}{\kappa_{st}} = 0.930. \quad \text{Eq. 5.4}$$

The curvature of the cantilever with the 460nm thick Au(111) film is 93% of the curvature calculated by the Stoney relation. Also, Fig. 5.17 shows that the range of error in stress measurements with Au(111) film/glass substrate is within the boundaries of 10% error, as h_f/h_s and M_f/M_s for Au film/glass substrate are 0.015 and 1.513, respectively. Therefore, the range of error in the stress measurement on the Au(111) film on the glass substrate using the Stoney relation is estimated to be less than 10%.

5.2.10 Resonance Frequency of Mica Cantilevers

The mica cantilever was expected to provide a proper deflection for stress measurements as well as flat surfaces for better STM imaging. The thickness of the mica cantilever, fabricated by cleaving and “press cutting”, was measured with an optical microscope ($\sim 500\times$). In order to confirm the validity of the thickness measurements, the results were compared with the thickness calculation based on the resonance frequency measurements of the cantilever. The STM system was used to measure the resonance frequency, which was monitored with the STM probe tip engaged near the end of cantilever. The thickness of the cantilever used for the comparison was $35.1 \pm 3.5\mu\text{m}$. The expected resonance frequency (f) with the thickness was calculated with Eq. 5.5 [66] to be

$$f = \frac{1}{2\pi} \left[\frac{3.5156}{L^2} \right] \sqrt{\frac{EI}{\rho A}} \quad , \quad \text{Eq. 5.5}$$

where L, E, I, ρ and A are the length, Young's modulus, area moment of inertia, density and cross-sectional area of the cantilever, respectively. Considering the

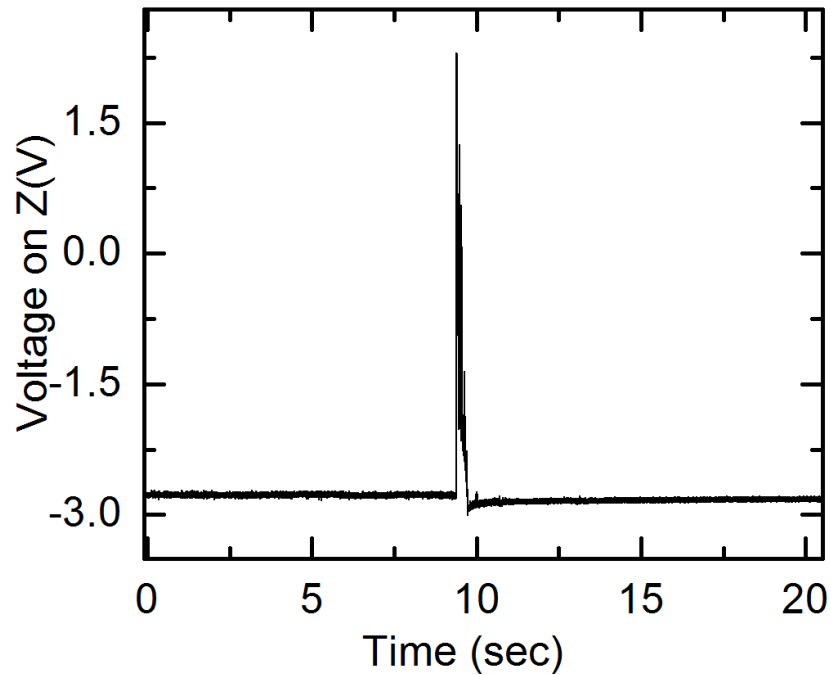


Fig. 5.18 The height of the probe tip vs. time for resonance frequency measurements. The peak at 10 sec corresponds to the physical impact on the STM system to enhance the resonance frequency of the cantilever. The time scale for every data point is 10 nano-seconds.

estimated error range for the mica cantilever's thickness and Young's modulus [67], the calculated frequency was 4.1 ± 0.6 kHz. During the frequency

measurement, the STM system was struck with a physical impact so that the peak corresponding to the resonance frequency could be enhanced. Fig. 5.18 shows the change in STM probe tip height (V) vs. time (sec) with the corresponding spike associated with the physical impact in the middle of the curve. The results of Fourier transform and a subsequent adjacent averaging at every 100 data points on the plot are shown in Fig. 5.19, which contains 4kHz.

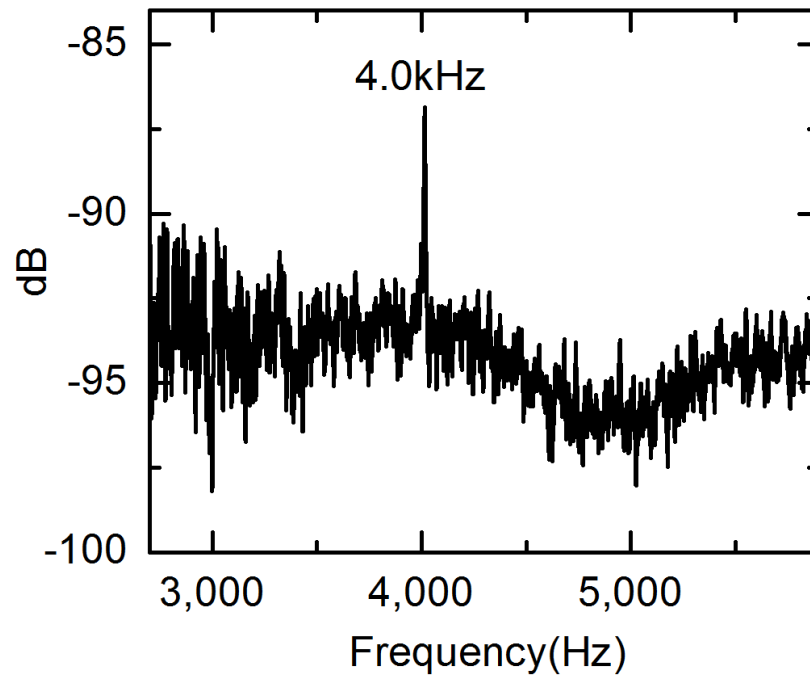


Fig. 5.19 The peak at 4kHz may correspond to the resonance frequency of the mica cantilever.

This is within the estimated range of the frequency calculation. Plugging the measured 4kHz frequency into Eq. 5.5 resulted in a thickness of 33.5 μm . However, because the peak at 4kHz is not significantly larger than other unknown peaks existing out of the frequency range of Fig. 5.19, the results of the resonance frequency measurements are less valid than those obtained with the optical microscope method to measure the thickness of the mica cantilever.

CHAPTER 6: RESULTS AND DISCUSSION

6.1 Surface Structure Evolution

The clean Au(111)-($22 \times \sqrt{3}$) surfaces are shown in the STM images in Fig. 6.1, obtained in the current work with RHK-STM system. Fig. 6.1(a) shows the characteristic herringbone structure. Shockley partial dislocations form

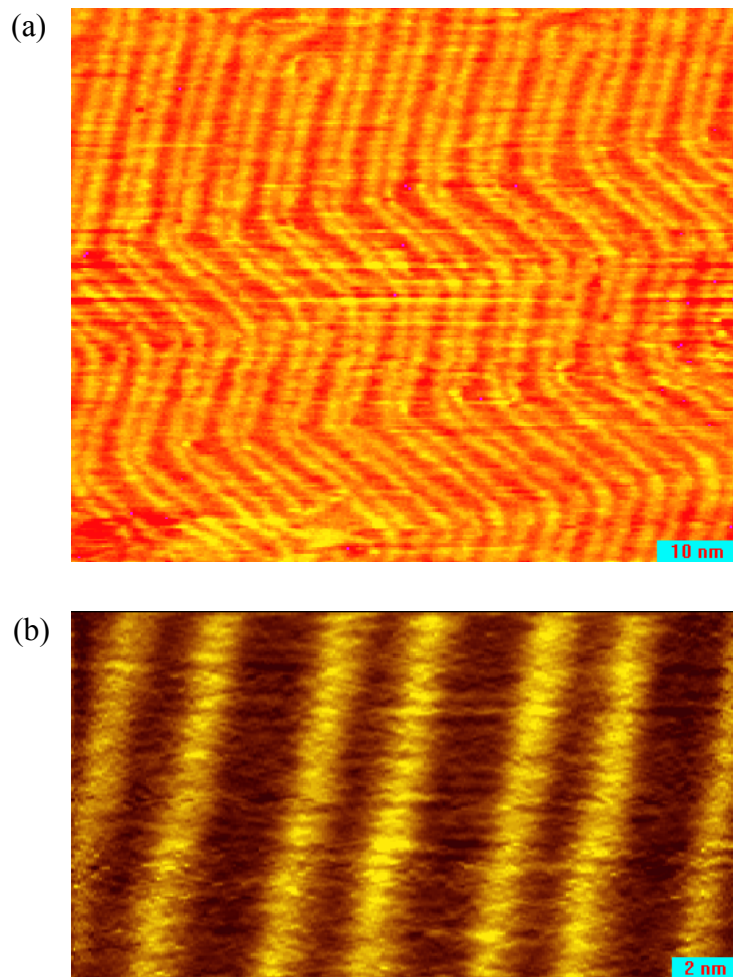


Fig. 6.1 STM images of clean Au(111)-($22 \times \sqrt{3}$) surfaces with magnifications (a) 85nm \times 70nm and (b) 20nm \times 11nm.

corrugation lines along the $\langle 1\bar{2}1 \rangle$ directions, which evenly divide the dihedral angle between the two closed packed directions of $\langle \bar{1}10 \rangle$ on (111) surface of the FCC structure. Leonard et. al. explained in their calculation based on anisotropic elastic theory that the anisotropy of the elastic properties of the substrate determines the periodicity and orientation of striped stress domain patterns [68]. According to the calculation, the lowest elastic energy is achieved when the stripe pattern is oriented along $\langle 1\bar{2}1 \rangle$ directions of the (111) surface of cubic materials. Fig. 6.1(b) clearly shows the corrugation lines separating two distinct regions, the wide unfaulted (FCC) and the narrow faulted (HCP).

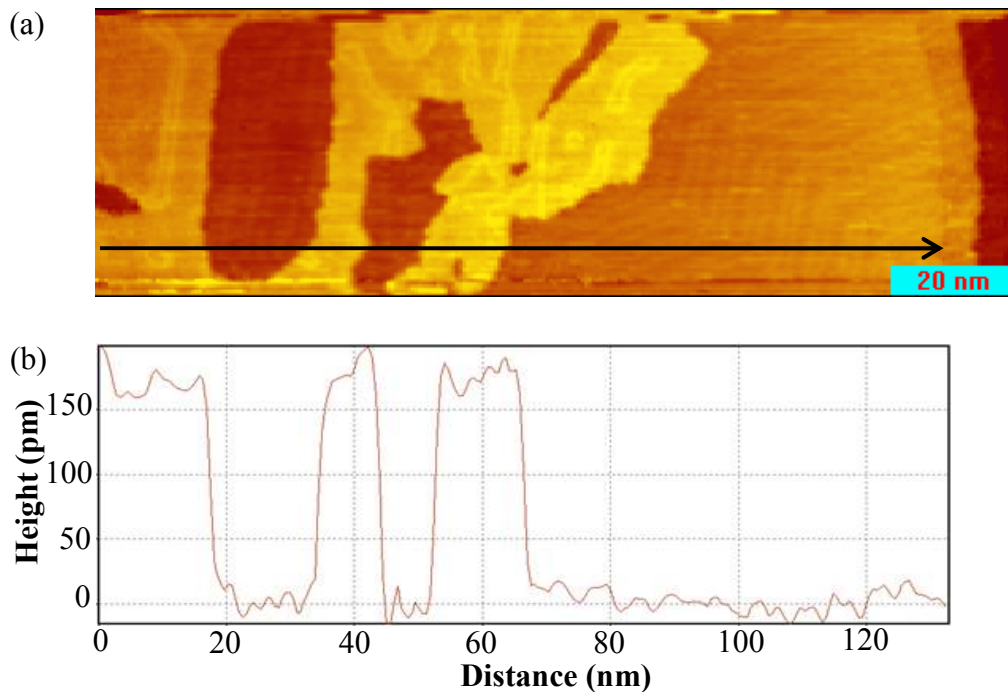


Fig. 6.2 (a) STM image of 0.4 ML of Cu on Au(111)- $(22 \times \sqrt{3})$ (140nm \times 45nm). (b) Line profile along the black arrow (The step height is about 0.15nm).

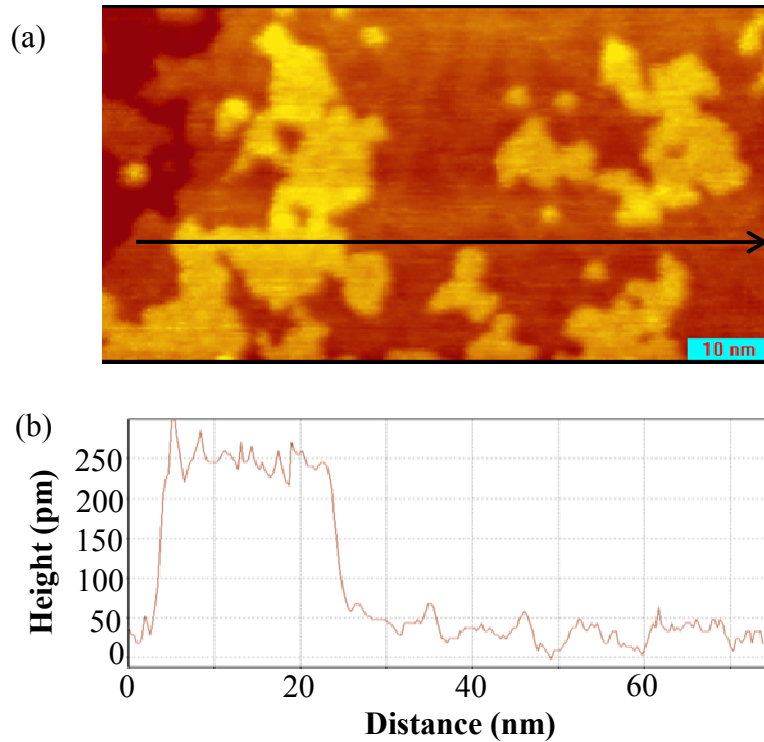


Fig. 6.3 (a) STM image of 0.4 ML of Cu on Au(111)- $(22 \times \sqrt{3})$ (80nm \times 40nm). (b) Line profile along the black arrow (The step height is about 0.20nm).

The separation distance between the pairs of corrugation lines was estimated to be about 6.1nm along the $\langle \bar{1}10 \rangle$ directions.

The monatomic step height of a Cu adlayer on the substrate is about 0.15nm as shown in Fig. 6.2(b), which is smaller than the interlayer distances of Cu(111) (0.21nm) and Au(111) (0.24nm). Grillo et. al. reported a similar result, arguing that the Cu adlayer may partially incorporate into the topmost Au layer, resulting in a reduced monatomic step height [69]. Also, this may result from

the effect of density state of Au surface. In the case of the second Cu adlayer, where the Au surface is less effective, the atomic step height is about 0.20nm, as shown in Fig. 6.3(b).

Fig. 6.4(a) shows the nucleation of Cu islands that occurred on the corrugation lines as well as on the step edges. Cu islands were found to contain a corrugation pattern similar to the pairwise arranged lines of the reconstructed Au(111) surface. However, the Cu corrugation pattern has different periodicities that are not well defined and lacks the herringbone structure.

Barth et. al.[40] showed a “U-shaped” ending of the pairwise arranged lines in Au(111)- $(22 \times \sqrt{3})$, where a short dislocation line connects two corrugation lines. The authors explained that either the FCC region or the HCP region can be terminated by the connection. In our experiments, an example of “U-shaped” termination is indicated by the arrow in Fig. 6.4(b) for the case of Cu/Au(111)- $(22 \times \sqrt{3})$. However, we observed termination of only the HCP region in this system. In addition to the stripe pattern, other styles of corrugation were also observed in several areas of the Cu adlayer. The diversity in pattern shape can be categorized into three different types: stripe, disordered stripe and trigonal patterns. At low coverage, the stripe pattern is formed in the small islands and is parallel to the substrate corrugation lines. The stripe pattern extends further in the same direction along the pairwise arranged lines of Au(111)- $(22 \times \sqrt{3})$, as the coverage increases. This alignment is generally observed where the Cu adlayers attach on the large terraces of Au(111)- $(22 \times \sqrt{3})$, as Fig. 6.4(c) shows

a relatively long stripe pattern. The pattern extension continues until the stripe pattern encounters neighboring corrugation lines, resulting in a disordered or bent stripe pattern as shown in Fig. 6.4(b).

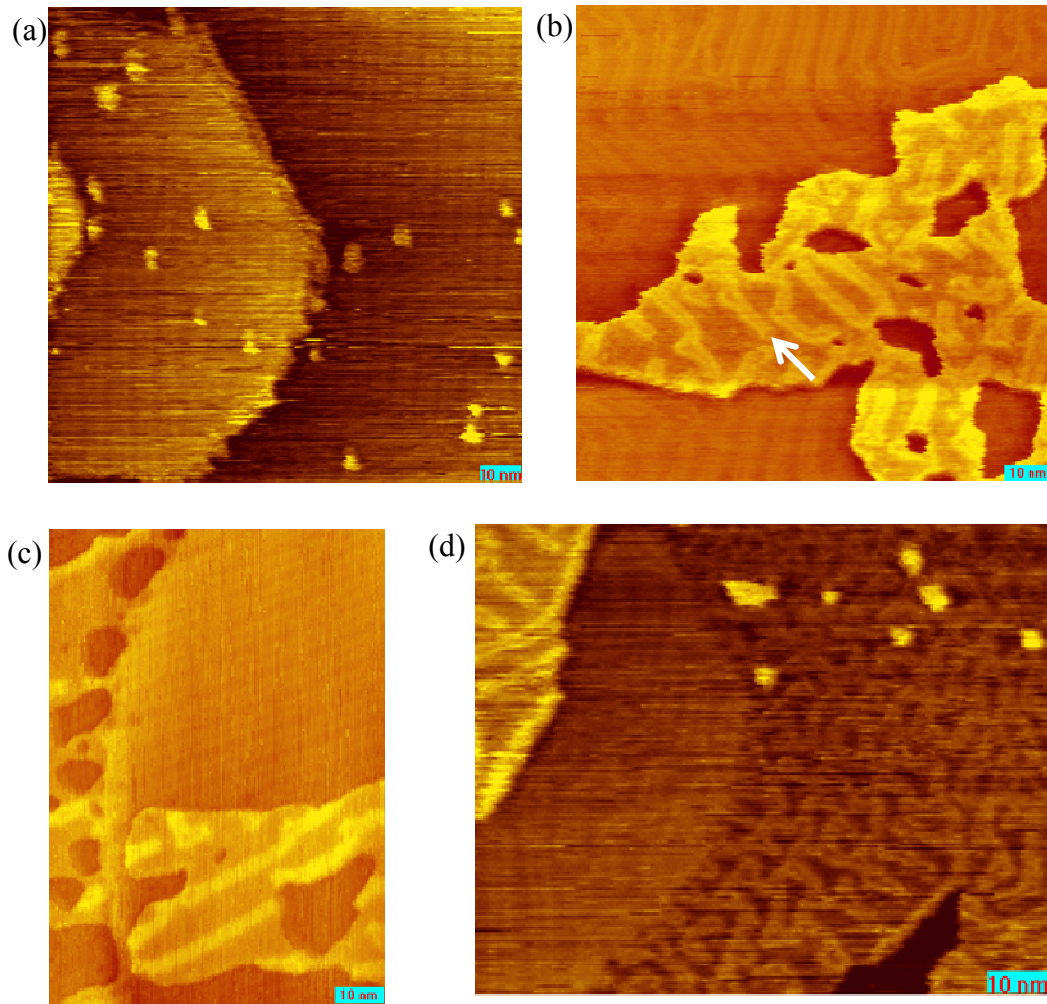


Fig. 6.4 STM images, focused on image quality, (a) 0.1ML Cu on Au(111)- $(22 \times \sqrt{3})$ (100nm \times 100nm). (b) 0.5ML Cu on Au(111)- $(22 \times \sqrt{3})$ (100nm \times 100nm). (c) The stripe pattern in Cu adlayer on Au (111))- $(\sqrt{3} \times 22)$ with long corrugation lines. (d) 0.8ML Cu on Au(111)- $(\sqrt{3} \times 22)$ (60nm \times 80nm).

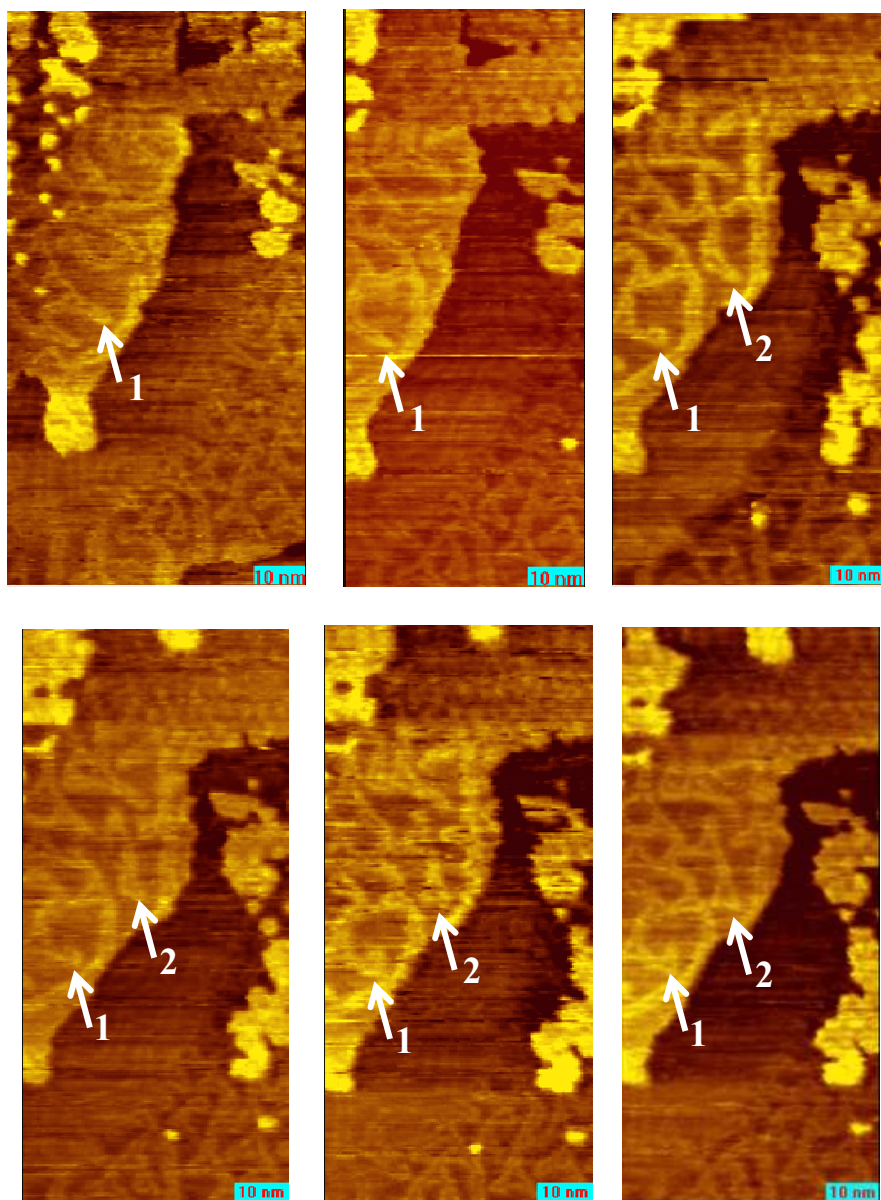


Fig. 6.5 The series STM images (100nm×50nm) of Cu on Au(111)- $(22 \times \sqrt{3})$ showing the process of trigon pattern formation from stripe pattern. The pattern alteration process is shown at two locations in the Cu adlayer indicated by the white arrows.

As the stripe pattern becomes more dense, the interaction among the corrugation lines increases. When the extension of the pairwise line is restricted by its neighbors, the “U-shaped” ending of the pairwise line alters its shape. This results in a trigon pattern that is triangular in shape as shown in Fig. 6.4(d). The transformation process from stripe to trigon pattern is shown by the series of STM images in Fig. 6.5. As “trigon” density increases, the trigonal pattern can form interconnected networks of trigons. At a total coverage of Cu more than 0.5ML, the nucleation of the second layer of Cu on top of the existing first layer is observed. Fig. 6.4(d) and Fig. 6.5 show the formation of second layer Cu islands on the first Cu layer with a dense trigon pattern. None of the previously described patterns continue in the second layer. Instead, a moiré pattern is observed as shown in the upper right part of each image in Fig. 6.5.

6.2 Discussion of Surface Structure Evolution

The surface structures in this work were often found to be more dense in Cu islands that extend to a border area of merging Cu islands or grow near the step edges of upper terraces of Au(111) as shown in Fig. 6.4(d) and Fig. 6.5. The Cu islands on the upper terrace of Au (Fig. 6.5), near the step, has a densely formed trigon pattern, while the Cu island on the upper terrace of Au (Fig. 6.4(d)), which is relatively far from the step, exhibits the stripe pattern only. Also, Fig 6.4(d) shows two Cu islands, one extending from the Au step edge toward to the left and the other extending from the right side, merging at the lower right corner of the figure. The dense trigon pattern is formed along the merging area. The

extension of Cu islands near those regions is restricted toward the step edge or the border, while the Cu islands located in the middle of the terrace and far away from their neighbors can freely extend. In the Cu islands whose extension is restricted, the interaction among the corrugation lines substantially increases. This results in an effective transition from stripe to trigon patterns with a locally dense surface structure formation. Moreover, the adatom concentration near step edge is higher than in the middle of terrace due to the Ehrlich-Schwoebel barrier [7, 70-72]. The higher concentration of adatoms can assist in formation of disordered stripe and trigon patterns, reducing the activation barrier for the dense structure formation.

The Cu/Au(111)-($22 \times \sqrt{3}$) system in this work did not form a Cu monolayer with a pseudomorphic structure. The pseudomorphic structure was observed in other epitaxial systems such as Cu/Ru(0001) and Ag/Pt(111), where strong interaction between adlayer and substrate atoms exists at the interface [42, 43]. For pseudomorphic structure formation in the Cu/Au(111)-($22 \times \sqrt{3}$) system, the anisotropic pattern of reconstructed Au(111) with two fold symmetry would tend to be transferred to the Cu adlayer with the similar periodicity of the corrugation lines. As described previously, the stripe pattern of the Cu adlayer does not have a constant periodicity and becomes disordered with increasing coverage. This is different from other systems that show evenly formed stripe patterns in the whole layer [42, 43, 45]. Cu/Ru(0001) and Ag/Pt(111) have three types of rotational stripe domains, but do not exhibit the herringbone structure.

Ag/Ru(0001) and Au/Ru(0001) both exhibit the herringbone structure as well as the rotational stripe domains, which are observed in Au(111)- $(22 \times \sqrt{3})$ [45].

Triangular networks of dislocations, which are similar to the trigon patterns in the current work, exist in ~ 1 -3 monolayers in other systems, including Ag/Pt(111), Ag/Ru(0001), Au/Ru(0001), Cu/Ru(0001) and alkali metals/Au(111)- $(22 \times \sqrt{3})$ [42, 43, 45, 73]. The trigonal pattern during alkali metal adsorption on Au(111) is formed by adsorbate induced bond weakening between the topmost layer and the next layer of Au producing an isotropic stress relaxation [73]. In the case of Ag/Pt(111), domain wall intersection produces a trigonal pattern, which was transformed from the stripe pattern by annealing at 800K [42]. The trigonal pattern in the 3ML Cu/Ru(0001) shows an interesting structure resembling a protruded “star” at intersected boundaries of three triangular domains [43]. Another interesting trigonal pattern is seen in both Ag/Ru(0001) and Au/Ru(0001) systems, formed by three independent equivalent and interwoven dislocation networks. The dislocation networks link each trigon in both the first and second layer with threading edge dislocations that build vertical segments without extending to the topmost surface [44, 45]. Ling et al. explained that the increase in atomic density in the interface with respect to the films makes the interwoven dislocation structure through layers energetically favorable in those systems[44]. However, trigonal pattern formation in Cu/Au(111)- $(22 \times \sqrt{3})$ does not appear to involve intersection of domain walls or formation of interwoven dislocation networks between layers. Rather, it results from

transformation of the “U- shaped” ending of the stripe pattern and subsequent connection with neighboring trigonal nodes. Furthermore, while only one type of pattern can be seen in each layer of the other systems described above, the Cu adlayer on reconstructed Au(111) maintains three distinct patterns together in one layer. This is likely due to kinetic limitations as the system in this work was not annealed after Cu deposition. It is important to notice that pattern transformation does not involve registry changes in the topmost layer only, but also involves all layers as addressed by Gunther et al.[43]. In the heteroepitaxial system of Cu/Ru(0001), the authors pointed out that the third layer (with three fold symmetry) cannot attach to the second layer (with two fold symmetry) without additional registry changes in layers below. Therefore, the pattern transformation (stripe-disordered stripe-trigon) in Cu adlayer on Au(111)- ($22 \times \sqrt{3}$) should be accompanied by a registry change between the reconstructed topmost layer and the next layer of Au. This could require an additional energy cost for a uniform pattern formation in the Cu adlayer on reconstructed Au(111).

6.3 Stress Evolution

6.3.1 Thermal Effect Removal

Fig. 6.6 shows the results of the thermal calibration experiments completed on three different locations of the probe tip on the glass cantilever. While Fig. 6.6(a) resulted from heat radiation only (no Cu deposition), the *in-situ*

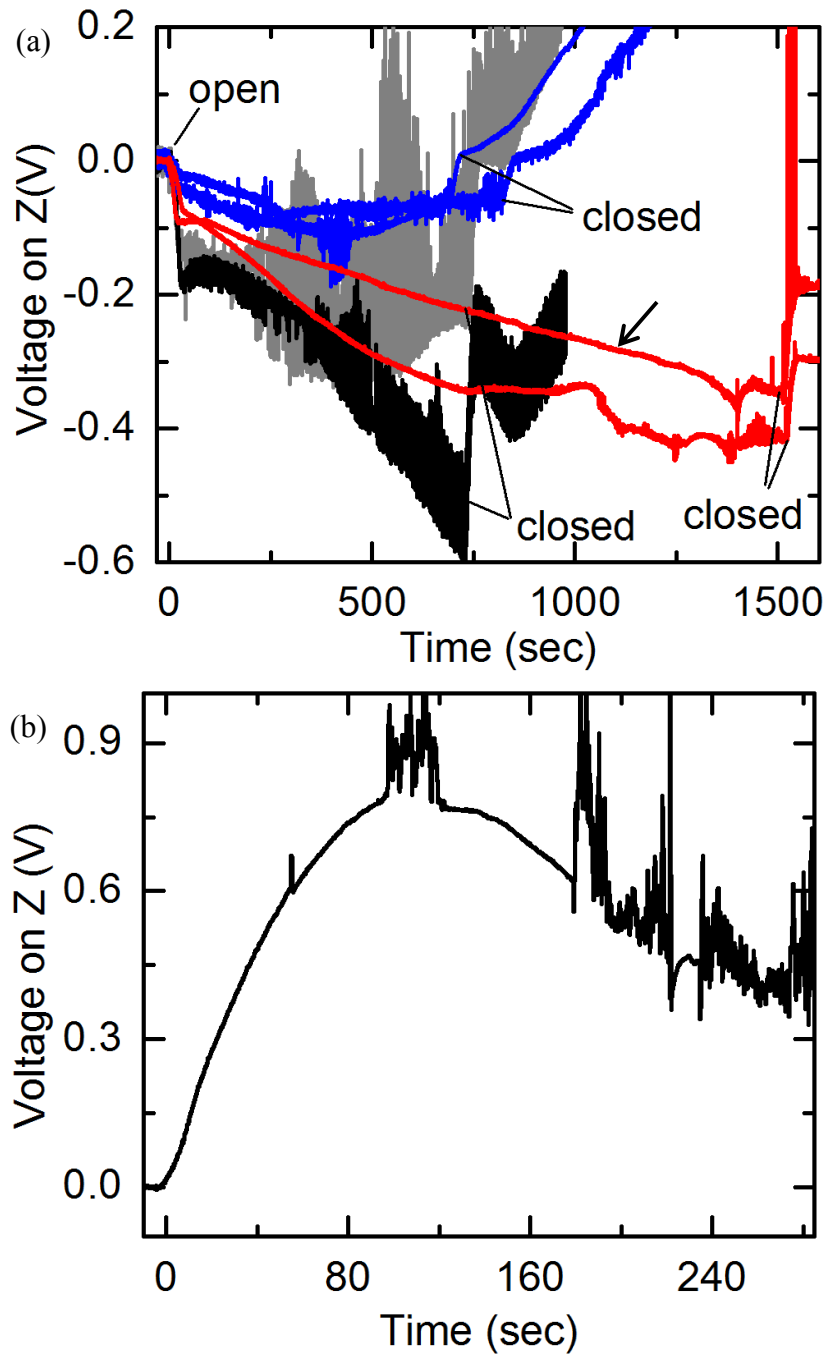


Fig. 6.6 (a) Results of thermal calibration on three different locations (two curves in a group per the probe tip location, blue 1.7mm, red 2.2mm and gray & black 3.0mm from the clamp). (b) Stress evolution plot on the corresponding location of 2.2mm from the clamp.

deposition source provided Cu deposition flux for Fig. 6.6(b). The distances between each tip location and the clamped edge of the cantilever were 1.7, 2.2 and 3.0 mm respectively, and the total cantilever length was 3.4mm. The three groups of plots in Fig. 6.6(a) correspond to the three locations and initially demonstrate a large negative slope followed by a transition to less negative slope in the long term.

The group of curves corresponding to the “3.0mm” location (gray and black) in Fig. 6.6(a) has the largest decrease after opening the shutter. This demonstrates that thermal effects on the STM system depend considerably on tip engagement locations on the cantilever.

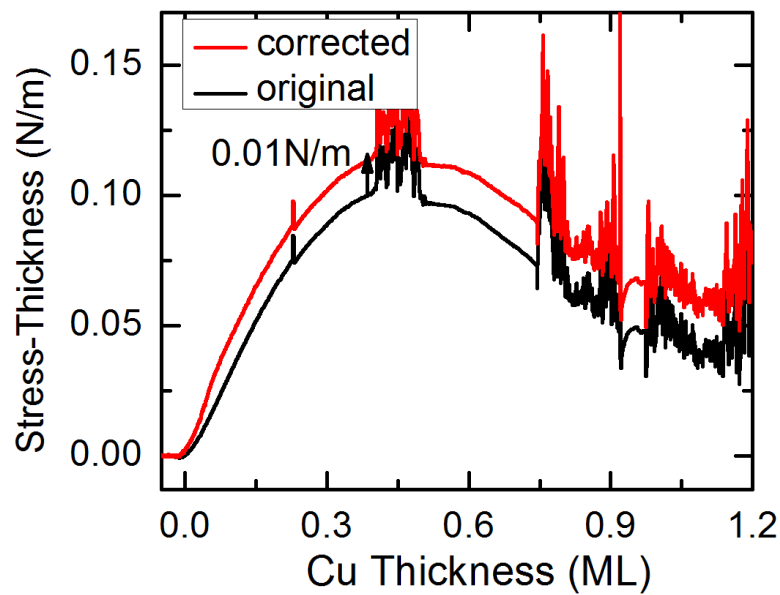


Fig. 6.7 Stress-thickness (N/m) vs. thickness plots after thermal effect correction.

The probe tip location for stress evolution during *in-situ* Cu deposition (Fig. 6.6(b)) was 2.2mm from the clamp edge. For the tip location of 2.2mm, the maximum value from Fig. 6.6(b) is 0.8V, which is significantly larger than the thermally induced amount from Fig. 6.6(a) of -0.1V (red) at the same time period of ~150 seconds.

The plot was corrected by subtraction of the thermal calibration slope of one of the red curves (marked with the black arrow) in Fig. 6.6(a), raising the peak about 0.01N/m as shown in Fig. 6.7. This results in the stress-thickness value of 0.1N/m after the unit conversion from the applied potential (V) on the piezoelement of the z direction.

6.3.2 Stress Evolution in Cu/Au(111)- $(22 \times \sqrt{3})$

Utilizing the method of subtraction of the thermally induced deflect, the plot in Fig. 6.8(a) was obtained for stress evolution of Cu growth on a Au(111)- $(22 \times \sqrt{3})$ /glass cantilever. The length of the cantilever was 3.4mm.

Here the stress was measured during simultaneous surface imaging by STM. Each segment between two spikes in the plot corresponds to an individual STM topographical image. The stress evolution plot in Fig. 6.7 appears to be more smooth than Fig. 6.8(a) because of the probe tip's stationary state (the tip was imaging during the capture of Fig. 6.8(a)). The stress evolution during deposition demonstrates an initial tensile shift and a subsequent compressive drop. The difference in maximum values seen in Fig. 6.7 and Fig. 6.8(a) can be attributed

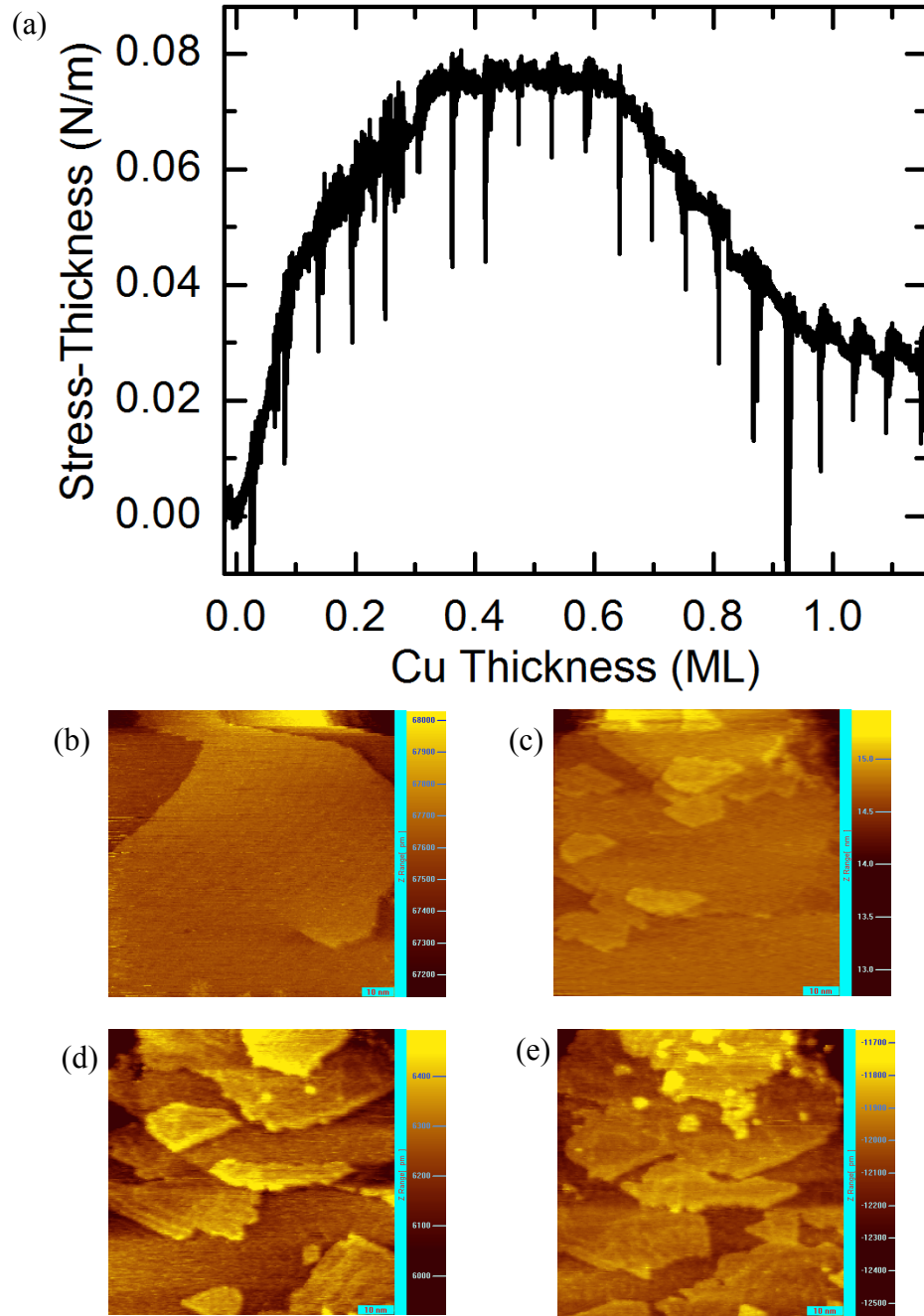


Fig. 6.8 (a) Stress evolution plot according to Cu thickness after thermal effect correction. This work was done with glass cantilever. (b) STM image of Au(111)- $(22 \times \sqrt{3})$, $100\text{nm} \times 100\text{nm}$, (c)~(e) STM images of Cu on Au(111)- $(22 \times \sqrt{3})$ ($80\text{nm} \times 80\text{nm}$). Cu coverage: (c) 0.2ML, (d) 0.5ML, (e) 1.0ML

to a slower deposition rate (0.03ML/min for Fig. 6.8(a) vs. 0.25ML/min for Fig. 6.7) that may provide a lower stress-thickness value in Fig. 6.8(a). Additionally, the tip for Fig. 6.8(a) was engaged at 1.7nm from the clamp, which is shorter than the tip engagement location of Fig. 6.7, thereby reducing the stress resolution. The difference in distance between the tip and the clamped edge results in a change in stress resolution. As indicated by the cantilever deflection equation (Eq. 4.8), the z height variation (U_z) increases by the square of the length between the tip and the clamped edge. As the length increases, the sensitivity of the technique to stress evolution in films is enhanced.

6.4 Stress and Structure Evolution

The results of stress evolution while simultaneously imaging the surface during *in-situ* Cu deposition are shown in Fig. 6.9. This work was done with a mica cantilever, which provided both appropriate stress measurements and STM imaging to investigate the stress-structure relation. The misfit strain of the heteroepitaxial system, Cu/ Au(111)-($22 \times \sqrt{3}$), is approximately 8~9%, imposing a tensile stress in the Cu film. As the Cu islands grow, the misfit strain considerably outweighs the tendency of Cu and Au atoms to maintain registry at the interface. The atomic registry change resulted in the formation of misfit dislocations, relieving the tensile stress. The misfit dislocations and their networks consist of the surface structures developed in the monolayer of Cu on Au(111)-($22 \times \sqrt{3}$). Table 6.1 summarized the stress relaxation and the development of the corresponding strain relief surface structure.

Table 6.1 Summary for stress relaxation and corresponding surface structure development

Cu coverage	Stress relaxation	Surface Structure
0ML	Partial	Stripe Pattern along $\langle 1\bar{2}1 \rangle$
0.5ML		Disordered Stripe + Trigon
1ML		Trigon Networks

Possible sites for introduction and growth of misfit dislocations are island ledges, the top of the Cu adlayer, and threading dislocations from elbows of each chevron in the herringbone structure of Au(111)- $(22 \times \sqrt{3})$ [48, 74]. This dislocation growth is believed to cause the change in slope of the stress behavior in Fig. 6.9(a).

The stress evolution of Fig. 6.9(a) is shown with two units of stress-thickness (N/m) and the applied voltage on the z piezo-element (V). The stress evolution during Cu deposition demonstrated an initial tensile shift and a small compressive drop at the peak. The repeating segment in the plot corresponds to an individual STM topographical image.

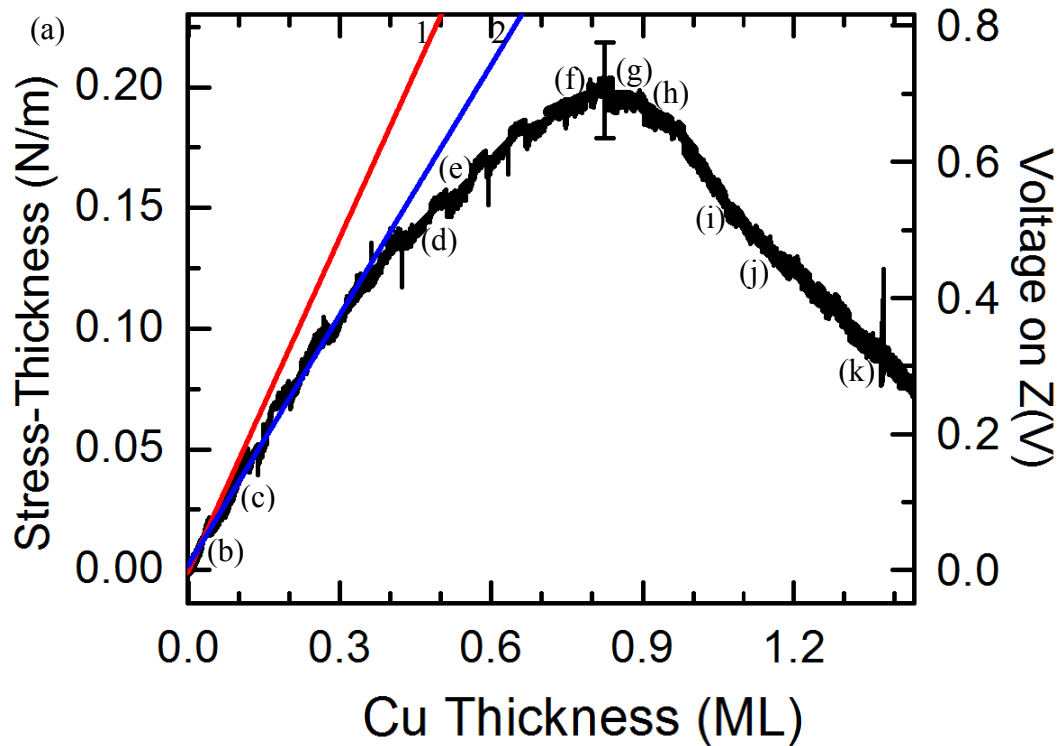


Fig. 6.9 Results of simultaneous stress measurement and surface imaging. The abrupt transition in the STM images resulted from shifting the position of the STM probe tip during imaging process. For instance, the STM image “(f)” has a repeating area because the STM probe tip scanned again the same area after the position shifting. (a) Stress-Thickness (N/m) vs. thickness plot. Line 1 and Line 2 correspond to the slopes of the first segment and the second through the fourth repeating segments, respectively. 10% error bar is located at the peak.

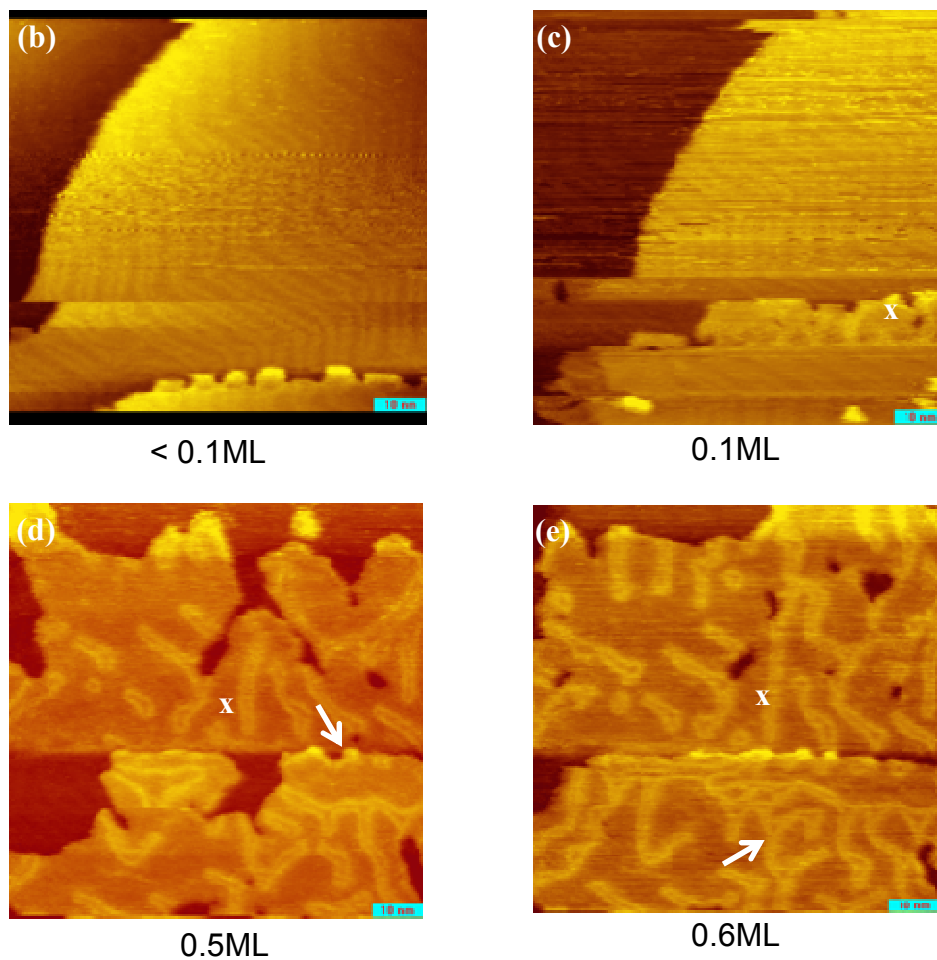


Fig. 6.9 con't, (b) Cu island nucleation at the step edge of Au surface. (c) Stripe pattern starts to form. (d) "U" shape ending of stripe pattern is observed. Some of stripe pattern are bent. (e) Disordered lines (marked by the white arrow) and trigon pattern are observed.

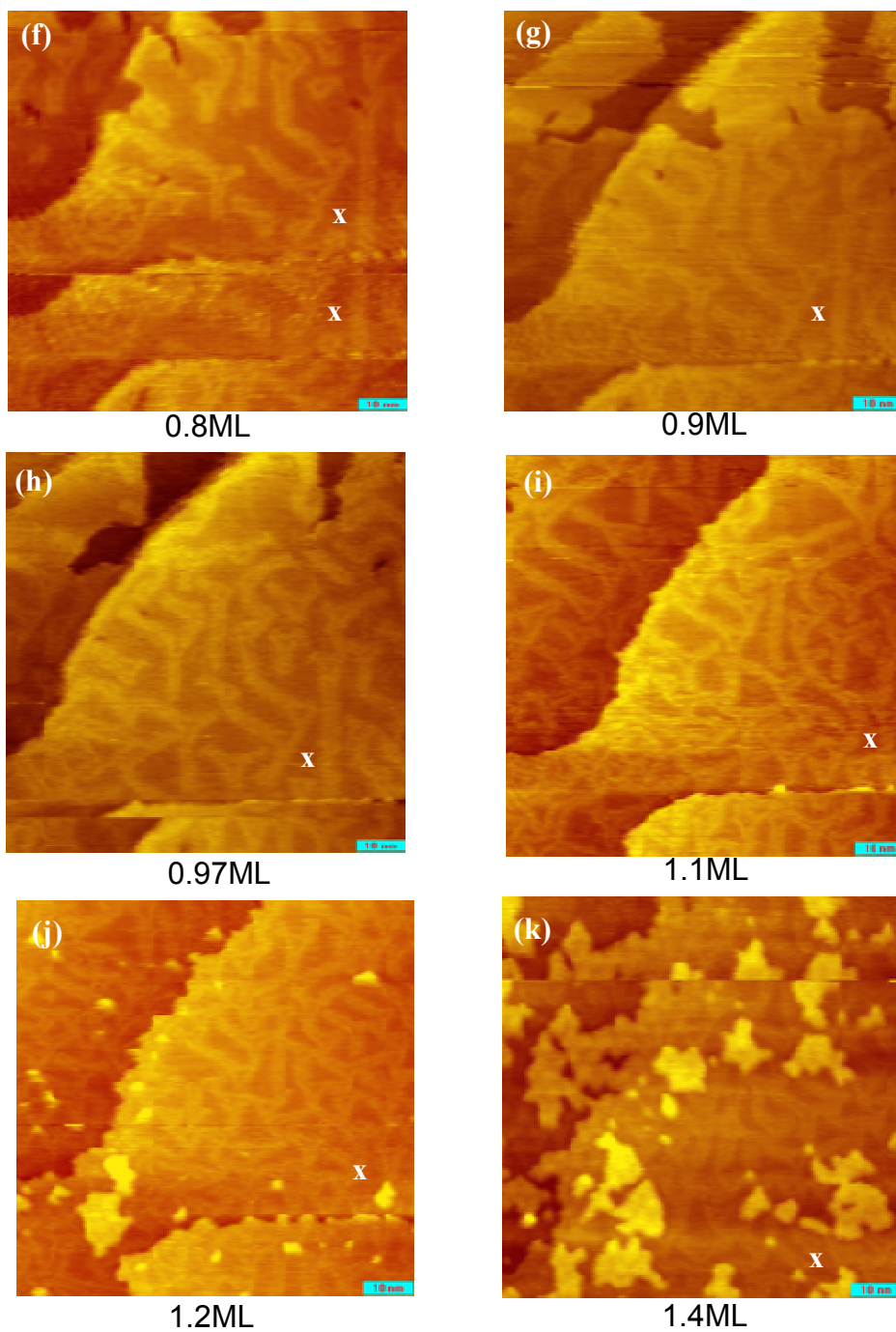


Fig. 6.9 con't, (f) ~ (k) Trigon pattern becomes dominant as Cu coverage increases. The stable second layer islands are clearly observed in (j) and (k). The size of all STM images is 80nm \times 80nm, and the scale bar located at the right bottom is 10nm.

The scanning time for each STM image and the total deposition time for 1.4 ML of Cu were two and a half minutes and 45 minutes, respectively. As shown in Fig. 6.9(a), the piezo voltage change for each STM image is about 17mV, which is significantly smaller than the total change of piezo voltage for stress evolution, 700mV. Therefore, the stress-induced changes in piezo voltage are on a substantially longer time scale and larger piezo scale than used for imaging. This allows for the deconvolution of the two sources of piezo voltage change, which are STM imaging and stress evolution during Cu growth.

STM images according to Cu coverage increase on Au(111)-($22 \times \sqrt{3}$) are shown in Fig. 6.9 (b) ~ (k). The white “x” marks the same spot on each STM image. The stripe pattern starts to form at 0.1ML of Cu (Fig. 6.9(c)) and extends as the Cu coverage increases. The slope of the first segment (line 1) in the plot of Fig. 6.9(a) is approximately 30% larger than the other slope (line 2) that covers the next three segments. This slope change is likely associated with the stripe pattern formation at 0.1ML of Cu. The slope changes from positive to negative near 0.8 ML of Cu, resulting from the substantial increase in dislocation density as the trigon pattern becomes dominant and disordered patterns are densely formed. Fig. 6.9 (f) ~ (k) show that as the Cu coverage increases, the network of trigon pattern spreads.

The stress-thickness at the peak is 0.19N/m. The stress-thickness divided by the corresponding film thickness results in the “average film stress”. The Cu thickness at the peak is 0.8ML, which is approximately equivalent to 0.18nm,

considering 1ML of Cu thickness to be the average interlayer spacing of Cu(111) and Au(111). Thus, the average Cu film stress is estimated to be 1.0GPa.

6.5 Discussion of Stress and Structure Evolution

The slope change in the stress evolution plot is associated with stress relaxation in the film. In the case of pseudomorphic small Cu islands in this work, which nucleate less than 0.1ML of Cu, the stress-thickness would be 0.22N/m based on the mean stress calculation for coherent film using bulk values of the elastic constants of Cu (mean stress \times thickness). This is substantially larger than the corresponding stress-thickness in Fig.6.9(a), which is 0.02N/m. As explained by Trimble et. al.[48], the initial tensile stress increase, corresponding to line 1 in Fig. 6.9(a), may be associated with the island edge relaxation stabilizing the coherency of the pseudomorphic islands.

In the case of the slope change from line 1 to line 2, as explained in Chapter 6.4, stripe pattern formation may result in the corresponding partial stress relaxation, introducing misfit dislocations at the interface. Furthermore stress relaxation at 0.8ML is likely attributed to trigon pattern formation because the dislocation density of trigon pattern is greater than stripe pattern. As trigon pattern forms, the misfit dislocation density increases more effectively, resulting in significant decrease in misfit strain at the interface. In this stage, the force exerted in the film (stress-thickness) becomes the maximum and starts to reduce (at the peak in Fig. 6.9(a)). This is possibly attributed to strain energy increase in the film with Cu coverage increase, which significantly outweighs the tendency of the

interface to maintain atomic registry. As a result, the misfit dislocation density as shown in STM images in Fig 6.9 (f) ~ (k) considerably increases with the slope change in the compressive direction as shown in Fig. 6.9(a).

The calculation of Frank and van der Merwe based on the Frenkel-Kontorova model supports the stripe pattern formation with a periodicity, which is favorable for the system where two commensurate phases coexist and individual surface stresses are dissimilar [75, 76]. The stress relaxation involved in the formation of the stripe pattern occurs in a uniaxial mode along the $\langle \bar{1} 10 \rangle$ direction, and in the case of surface reconstruction of Au(111), a further relaxation is achieved by forming a long range order of superstructure, the so called “herringbone” structure. Within the individual domains, the stress is only uniaxially relaxed. Overall isotropic stress relaxation is achieved via the combination of multiple domains rotated 120° relative to one another [40].

The Cu stripe pattern involves the uniaxial tensile stress relaxation, following the underlying direction of the pairwise lines according to the orientation of each domain in Au(111)- $(22 \times \sqrt{3})$. As the stripe pattern extends at low Cu coverages, the stress relaxation continues in the uniaxial mode along the $\langle \bar{1} 10 \rangle$ directions. However, the large slope change at the peak in Fig. 6.9(a) may indicate a transition in the stress relaxation mode. The isotropic stress relaxation is achieved when the trigon pattern is formed, owing to the three fold symmetry of the trigon pattern.

The increase of dimensionality of the stress relaxation mode from uniaxial to isotropic results in a significant decrease of the strain energy, reducing the

misfit strain at the interface [43]. However, the introduction of additional misfit dislocation increases the interfacial free energy, which is associated with an energy cost to change registry at interface [77]. The increased strain energy in enlarged islands, therefore, causes strain relief surface structures to form at the expense of the interfacial free energy. The energetic competition between strain energy and the interfacial free energy is summarized in Table 6.2 for the surface structure change process, which is associated with the increase of dimensionality of the stress relaxation mode.

Table 6.2 Summary for strain energy vs. surface free energy for strain relief surface structure change.

PATTERN	STRAIN ENERGY	INTERFACIAL FREE ENERGY
Stripe	High	Low
Disordered	Middle	Middle
Trigon	Low	High

Trimble et. al., who investigated the Cu on Au(111) system [48], observed the rapid slope change and the corresponding formation of dense surface structure

in the molecular dynamics (MD) simulation results, as explained in Chapter 2. In what is termed “funneling,” the authors argued that the second layer acts as a source for interlayer transport, which rapidly increases the misfit dislocation density in the first adlayer. This is associated with the slope change from positive to negative in their stress evolution results. Similar to Trimble et. al.’s results, we observed the nucleation of the second layer before the first layer completion. Fig. 6.9(d) shows the nucleated island at the step edge of the first layer (marked with the white arrow). The island did not grow until the coverage became 1ML of Cu (Fig. 6.9(i)). Some of the nucleated islands were observed to be metastable and disappeared in the following STM imaging during in-situ Cu deposition. In the current work of Cu on Au(111)- $(22 \times \sqrt{3})$, the funneling process may decrease the adatom lifetime [7], providing insufficient surface diffusion for the second layer growth. This reduces the probability that Cu adatoms will encounter each other at nucleation sites for the formation of the second layer islands, because they may undergo the funneling process before reaching nucleation sites. Even the Cu atoms in the second layer island, which is nucleated by chance, may funnel into the first adlayer before the nucleated islands grow. However, when surface structures with higher misfit dislocation densities in the first layer are formed, the funneling process is less favorable, and the nucleated second layer islands can grow as shown in Fig. 6.9(j). Also, stable second layer islands were observed on the local area with the dense surface structure in the first Cu layer as shown in Figs. 6.4(d) and 6.5. Therefore, when strain energy reduction is accompanied by the funneling process, the activation barrier for formation of dense misfit

dislocations can be effectively reduced, resulting in the large stress relaxation at the peak in Fig. 6.9(a).

CHAPTER 7: SUMMARY AND FUTURE WORK

The surface structures in ultrathin films of heteroepitaxial systems are developed with the relaxation of misfit strain at the interface. The examples of strain relief structures on the surfaces of ultrathin films, which are pseudomorphic, stripe, trigonal and moiré patterns have been introduced. These structures were found in existing literature of heteroepitaxial systems such as Cu/Ru(0001), Ag/Ru(0001), Ag/Pt(111) and Cu/Au(111) [34, 35, 37, 55]. In order to investigate the stress evolution that is associated with the strain relief structures, an STM system has been modified so that it can perform stress measurements. The modifications include adjusting the STM sample holder to contain a membrane or a cantilever substrate and designing a small deposition source to fit in the limited area of the STM stage.

The 1ML of Cu film on Au(111)-($22 \times \sqrt{3}$) exhibited stripe, disordered stripe and trigonal patterns. The moiré pattern was also found in the 2ML thick Cu film. At lower Cu coverages, less than 0.8ML, the stripe pattern was formed as the tensile stress increased. Around 0.8ML of Cu, the tensile stress rapidly relaxed, changing the slope of stress evolution into a compressive direction. The surface structure became complicated as the pairwise misfit dislocations interacted with each other and some became disordered. At this Cu coverage, Cu islands were nucleated on top of the existing Cu adlayer, which provided a source of atoms for interlayer transport between the top and bottom layers. This effectively caused relaxation of the tensile stress and formation of complicated

surface structures in the strained layer. The trigon structure also started to form at this stage.

The comparison of this work with other systems described above revealed that the surface structures of Cu/Au(111)- $(22 \times \sqrt{3})$ for these experimental conditions were different from other systems, Cu/Ru(0001), Ag/Ru(0001), Ag/Pt(111) and Cu/Au(111), where a uniform pattern was formed in the single layer. A possible reason for this is that the Cu film was grown at room temperature and did not go through an annealing process, which could induce kinetic limitations. Another possible cause for the lack of uniform surface structure in the top Cu layer is the registry change required in the lower layer. The under-layer registry change could also be kinetically limiting the uniformity in the surface structure.

Future work could study the further analysis for strigon pattern formation in the current system. Trigon pattern formation in this work results from the interaction among the stripe pattern as shown in Fig. 6.5. Also, depending on surface structure of Au(111)- $(22 \times \sqrt{3})$, either long corrugation lines or herringbone structure, it was observed the trigon shape and its density were different. Moreover, the elbow at each chevron containing edge dislocation may provide threading dislocation source. The comparison of surface structure in Cu adlayer attached on those two distinct Au surface regions may reveal the herringbone structure effect on trigon pattern formation.

Additionally, Cu growth (or annealing) temperature could be another factor to control surface structure formation. The temperature increase in the substrate

reduces kinetic limitations to uniform structure formation in the monolayer of Cu. The *in-situ* stress monitoring and surface imaging experiments may show structure change from non-uniform to uniform surface structure and the corresponding stress evolution.

Furthermore, future work with the current system could investigate stress and structure evolution in thicker Cu films, i.e. more than one monolayer on Au(111)- $(22 \times \sqrt{3})$. Stress measurements with the STM probe tip in a stationary mode showed another tensile stress increase at around 1.5ML of Cu. This result must be confirmed with simultaneous stress measurements and STM imaging during Cu deposition. A moiré pattern was observed in the second Cu layer, which implies that the Cu layer potential becomes dominant over the Au(111) substrate potential according to the Frenkel-Kontorova (FK) model. The mechanism of the second tensile stress increase may be related to the moiré pattern formation. *In-situ* experiments for stress and structure are expected to verify the mechanism.

Other heteroepitaxial systems of X/Au(111)- $(22 \times \sqrt{3})$ could be investigated as future works. Several transition metals with low melting points (such as Cu) could be used as deposition materials. The source material should not require excessive resistive heating for evaporation so that the accompanying heat effect will not disrupt proper operation of the STM system for both stress measurements and imaging. The herringbone structure of Au(111)- $(22 \times \sqrt{3})$ provides a preferential nucleation on the elbow for growth of some transition

metals such as Fe, Co, Ni and Mn [78-80]. However, the preferential nucleation was not observed for other metals including Al, Ag Au and Cu [78]. We also noted that Cu was not preferentially nucleated on elbow sites. Meyer et. al.[78] suggested in their works with Ni/Au(111)- $(22 \times \sqrt{3})$ that preferential nucleation occurs in two steps. First, Ni atoms replace Au atoms on the elbow sites. Second, the subsequent growth takes place on top of the substituted Ni. Future work with early stage metal growth involving preferential nucleation may reveal a differing stress evolution behavior than the current work of Cu/Au(111)- $(22 \times \sqrt{3})$.

Furthermore, the results may verify the two step mechanism for the preferential nucleation with surface structure change and the corresponding stress evolution.

Finally, the modified STM system could be used to examine other heteroepitaxial systems without using Au(111)- $(22 \times \sqrt{3})$, such as graphene film on crystalline substrates. As explained in Chapter 1, SiC and Ru can provide heteroepitaxial growth for graphene [23, 24]. A graphite filament that can be installed in the current *in-situ* deposition system can provide a carbon source for graphene growth. It is possible to investigate the stress evolution during *in-situ* growth of graphene using the carbon source. This may result in valuable contributions to fabrication and research for graphene based devices.

Additionally, if the current STM system is equipped with four point probe technology with a multiple probe tip technique [81], it will be possible to study electronic properties of continuous graphene films over a single layer, leading to

potentially effective research into the stress-structure-property relations in heteroepitaxial systems.

REFERENCES

- [1] J. V. Barth, G. Costantini, and K. Kern, *Nature* **437** (2005).
- [2] H. Brune *et al.*, *Nature* **394** (1998).
- [3] K. S. Kim *et al.*, *Nature* **457** (2009).
- [4] H. Ko *et al.*, *Nature* **468** (2010).
- [5] H. J. Freund, and G. Pacchioni, *Chemical Society Reviews* **37** (2008).
- [6] F. Sedona *et al.*, *Journal of Physical Chemistry C* **111** (2007).
- [7] J. A. Venables, *Introduction to Surface and Thin Film Processes* (Cambridge University Press, New York, 2000), 1st Ed. edn.
- [8] L. B. Freund, and S. Suresh, *Thin Film Materials* (Cambridge University Press, New York, 2003), 1st edn.
- [9] C. Friesen, and C. V. Thompson, *Physical Review Letters* **89** (2002).
- [10] C. Friesen, S. C. Seel, and C. V. Thompson, *Journal of Applied Physics* **95** (2004).
- [11] R. Koch, *Journal of Physics-Condensed Matter* **6** (1994).
- [12] R. Koch, *Applied Physics a-Materials Science & Processing* **69** (1999).
- [13] D. Sander *et al.*, *Physical Review B* **57** (1998).
- [14] S. C. Seel *et al.*, *Journal of Applied Physics* **88** (2000).
- [15] J. A. Floro *et al.*, *Journal of Applied Physics* **89** (2001).
- [16] C. S. Smith, *Physical Review* **94** (1954).
- [17] B. Wong *et al.*, *Nano-CMOS Design for Manufacturability: Robust Circuit and Physical Design for Sub-65nm Technology Nodes* (John Wiley & Sons, Hoboken, NJ, 2009), 1st Ed. edn.
- [18] M. Bohr, and K. Mistry, (Intel, 2011).
- [19] L. Washington *et al.*, *Ieee Electron Device Letters* **27** (2006).

- [20] J. D. Plummer, M. D. Deal, and P. B. Griffin, *Silicon VLSI Technology, Fundamentals, Practice and Modeling* (Prentice Hall, Upper Saddle River, 2000), 1st Ed. edn.
- [21] K. N. Tu, *Journal of Applied Physics* **94** (2003).
- [22] K. S. Novoselov *et al.*, *Science* **306** (2004).
- [23] C. Berger *et al.*, *Science* **312** (2006).
- [24] D. Martoccia *et al.*, *Physical Review Letters* **101** (2008).
- [25] M. Wuttig, and X. Liu, *Ultrathin Metal Films, Magnetic and Structural Properties* (Springer, Berlin, 2004), 1st Ed. edn., Springer Tracts in Modern Physics.
- [26] D. Sander, A. Enders, and J. Kirschner, *Journal of Magnetism and Magnetic Materials* **200** (1999).
- [27] J. Buschbeck *et al.*, *Physical Review Letters* **103** (2009).
- [28] C. Friesen, and C. V. Thompson, *Physical Review Letters* **93** (2004).
- [29] B. Fu, and G. B. Thompson, *Journal of Applied Physics* **108** (2010).
- [30] B. Fu, and G. B. Thompson, *Applied Surface Science* **257** (2010).
- [31] T. M. Trimble, R. C. Cammarata, and K. Sieradzki, *Surface Science* **531** (2003).
- [32] K. Oura *et al.*, *Surface Science, An Introduction* (Springer, Berlin, 2003), 1st Ed. edn.
- [33] R. Singh, in *STM Gallery* (Prof. Michael Trenary Group, Chicago).
- [34] G. Dujardin *et al.*, *Physical Review Letters* **76** (1996).
- [35] K. W. Hipps, *Scanning Tunneling Spectroscopy (STS)* (Springer, New York, 2006), *Handbook of Applied Solid State Science Spectroscopy*.
- [36] M. Itoh. Dimer Adatom Stacking-Fault Structure of Si(111)-(7x7). (<http://www.geocities.jp/mitoh6/index.html>)
- [37] G. Ritz *et al.*, *Physical Review B* **56** (1997).

- [38] G. E. Poirier, *Langmuir* **13** (1997).
- [39] O. Schaff *et al.*, *Materials Science and Engineering a-Structural Materials Properties Microstructure and Processing* **319** (2001).
- [40] J. V. Barth *et al.*, *Physical Review B* **42** (1990).
- [41] H. Roder *et al.*, *Nature* **366** (1993).
- [42] H. Brune *et al.*, *Physical Review B* **49** (1994).
- [43] C. Gunther *et al.*, *Physical Review Letters* **74** (1995).
- [44] W. L. Ling *et al.*, *Physical Review Letters* **92** (2004).
- [45] W. L. Ling *et al.*, *Surface Science* **600** (2006).
- [46] O. M. Braun, and Y. S. Kivshar, *The Frenkel-Kontorova Model, Concepts, Methods and Applications* (Springer, Berlin, 2004).
- [47] R. Pushpa, J. Rodriguez-Laguna, and S. N. Santalla, *Physical Review B* **79** (2009).
- [48] T. Trimble *et al.*, *Physical Review Letters* **95** (2005).
- [49] R. C. Cammarata, K. Sieradzki, and F. Spaepen, *Journal of Applied Physics* **87** (2000).
- [50] R. Shuttleworth, *Proceedings of the Physical Society of London Section A* **63** (1950).
- [51] J. W. Matthews, *Epitaxial Growth* (Academic Press, New York, 1975).
- [52] G. Binnig *et al.*, *Physical Review Letters* **50** (1983).
- [53] C. J. Chen, *Introduction to Scanning Tunneling Microscopy* (Oxford University Press, New York, 2008), 2nd Ed. edn.
- [54] J. Frenken, (Interface Physics Group, 2004).
- [55] G. Binnig, and H. Rohrer, *Reviews of Modern Physics* **59** (1987).
- [56] R. Wiesendanger, *Scanning Probe Microscopy and Spectroscopy, Methods and Applications* (Cambridge University Press, New York, 1994).

- [57] J. Bardeen, *Physical Review Letters* **6** (1961).
- [58] J. Tersoff, and D. R. Hamann, *Physical Review B* **31** (1985).
- [59] D. A. Bonnell, *Scanning Probe Microscopy and Spectroscopy-Theory, Technique, and Applications* (Wiley-VCH, Inc., New York, 2001), 2nd edn.
- [60] W. D. Nix, (Stanford University, Stanford, 2005).
- [61] S. Timoshenko, and S. Woinowsky-Krieger, *Theory of Plates and Shells* (McGraw-Hill Book Company, New York, 1959), 2nd Ed. edn.
- [62] T. Narushima, N. T. Kinahan, and J. J. Boland, *Review of Scientific Instruments* **78** (2007).
- [63] L. Mickelson, T. Heaton, and C. Friesen, *Journal of Physical Chemistry C* **112** (2008).
- [64] N. T. Kinahan *et al.*, *Physical Review Letters* **104** (2010).
- [65] B. Voigtlander, and M. Kastner, *Journal of Vacuum Science & Technology B* **17** (1999).
- [66] T. Irvine, Madison, Alabama, 2010).
- [67] C. Friesen *et al.*, *Langmuir* **17** (2001).
- [68] F. Leonard, N. C. Bartelt, and G. L. Kellogg, *Physical Review B* **71** (2005).
- [69] F. Grillo *et al.*, *New Journal of Physics* **13** (2011).
- [70] K. Morgenstern *et al.*, *Physical Review Letters* **80** (1998).
- [71] G. Ehrlich, and F. G. Hudda, *Journal of Chemical Physics* **44** (1966).
- [72] Schwoebe.RI, and E. J. Shipsey, *Journal of Applied Physics* **37** (1966).
- [73] J. V. Barth, R. J. Behm, and G. Ertl, *Surface Science* **302** (1994).
- [74] J. S. Wu *et al.*, *Journal of Crystal Growth* **234** (2002).
- [75] K. Bromann *et al.*, *Surface Science* **388** (1997).

- [76] F. C. Frank, and J. H. Vandermerwe, Proceedings of the Royal Society of London Series a-Mathematical and Physical Sciences **198** (1949).
- [77] R. C. Cammarata, and K. Sieradzki, Annual Review of Materials Science **24** (1994).
- [78] J. A. Meyer *et al.*, Surface Science **365** (1996).
- [79] M. Fonin *et al.*, Surface Science **529** (2003).
- [80] W. G. Cullen, and P. N. First, Surface Science **420** (1999).
- [81] S. Yoshimoto *et al.*, Nano Letters **7** (2007).

APPENDIX A

ORIGINAL STRESS-THICKNESS PLOT WITH THE FULL SET OF STM

IMAGES FOR FIG.6.9

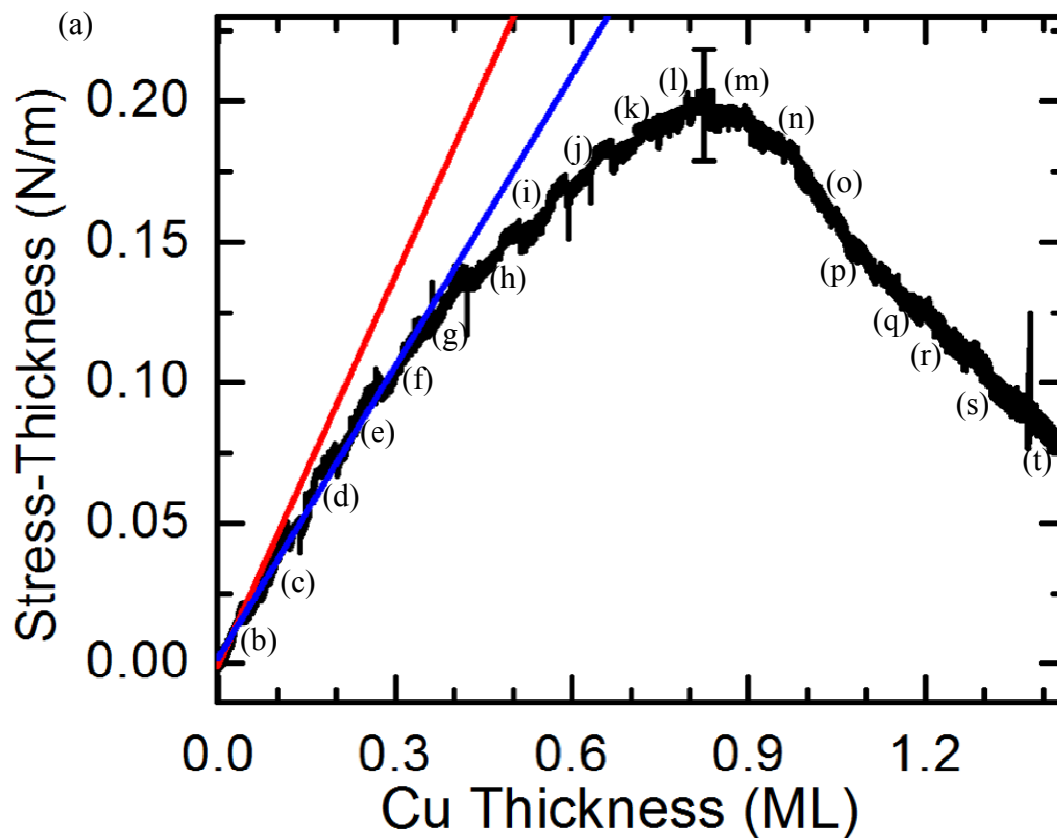
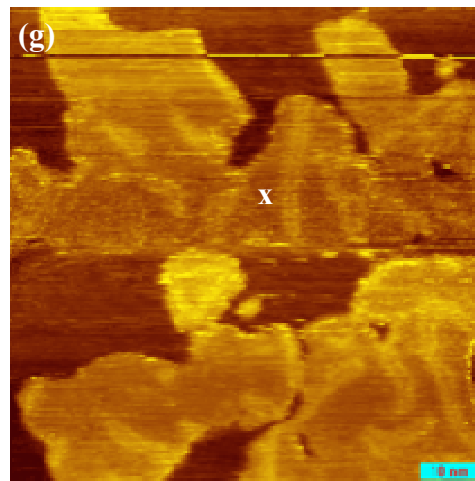
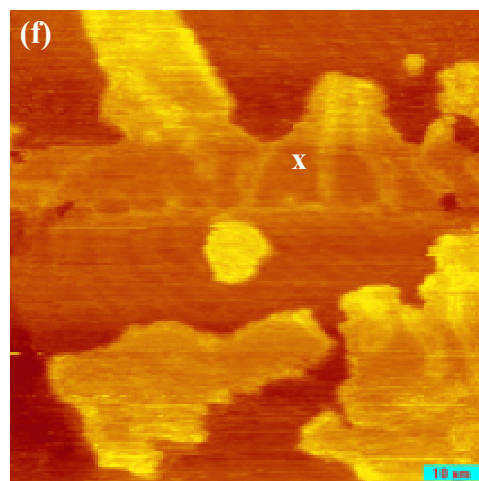
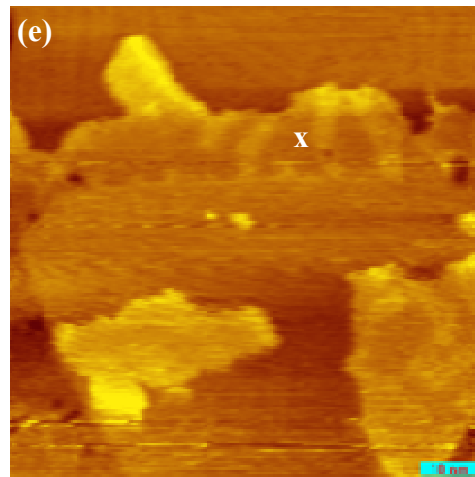
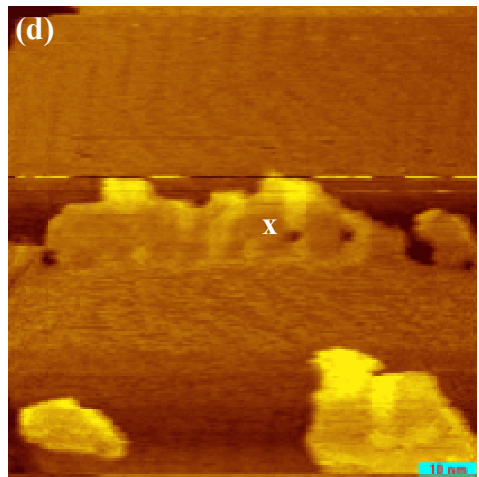
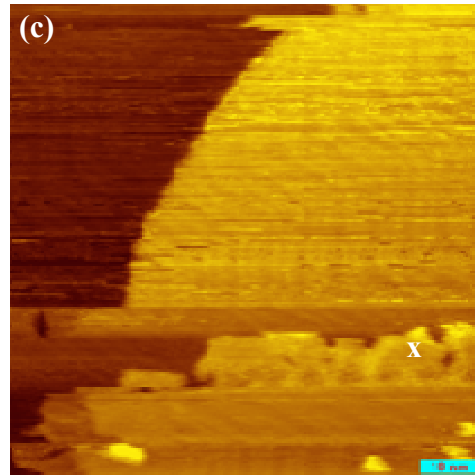
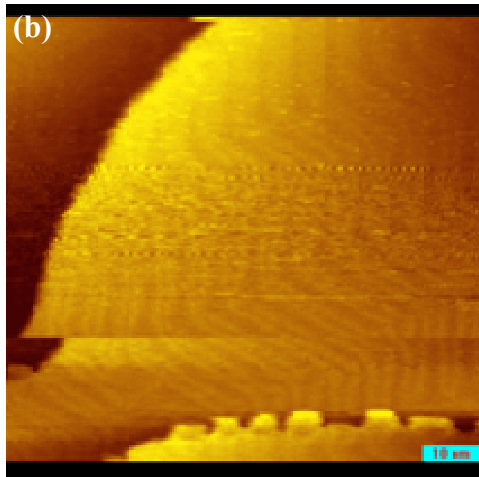
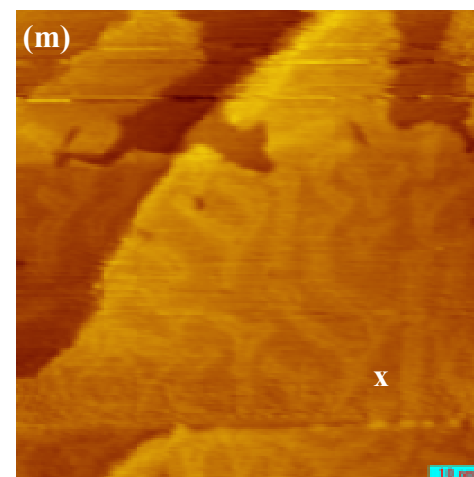
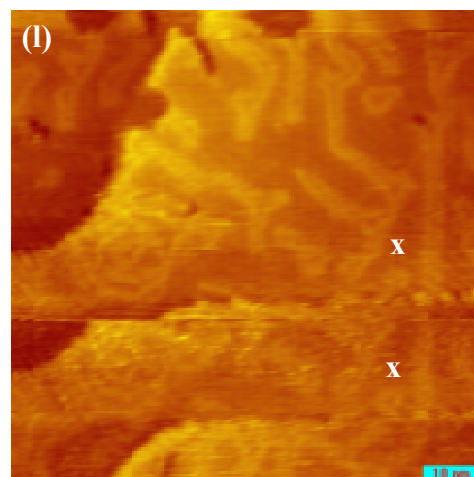
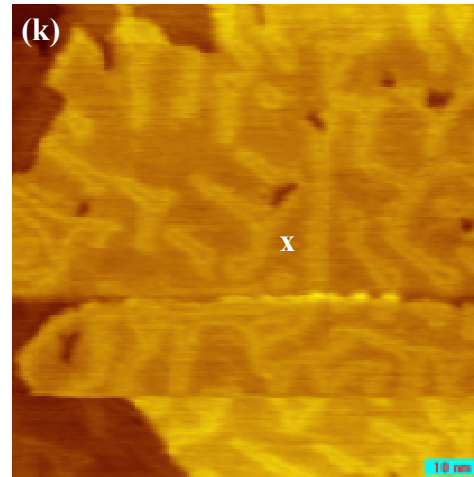
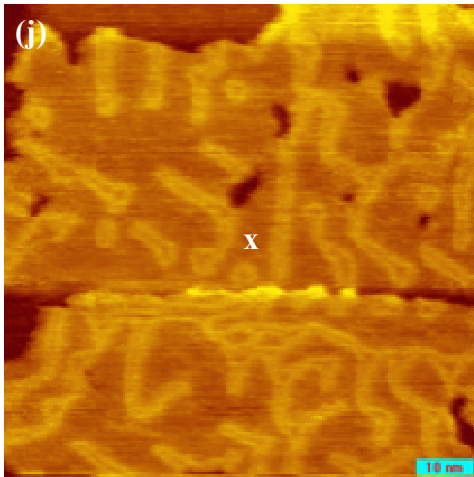
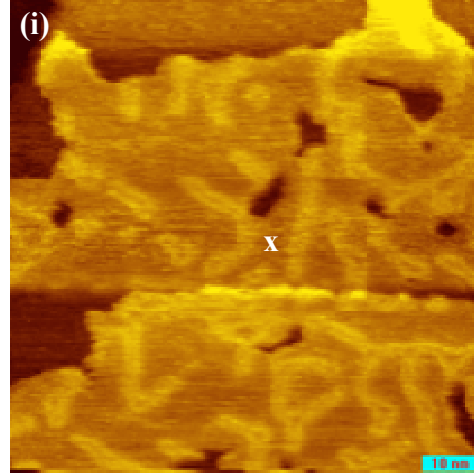
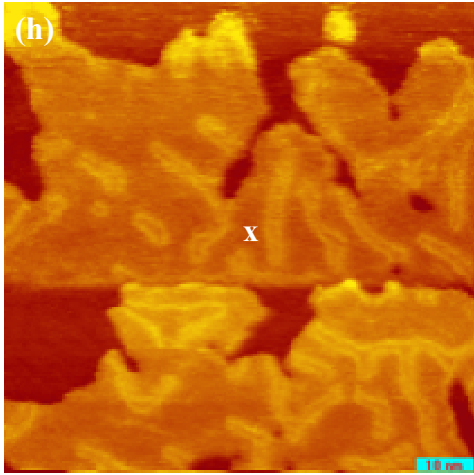
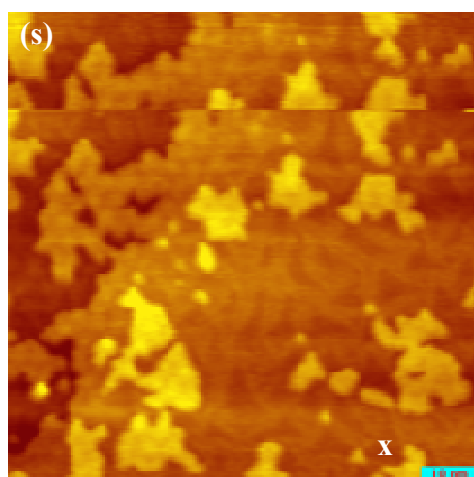
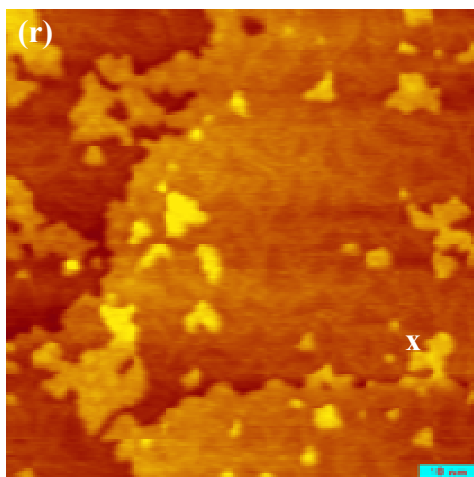
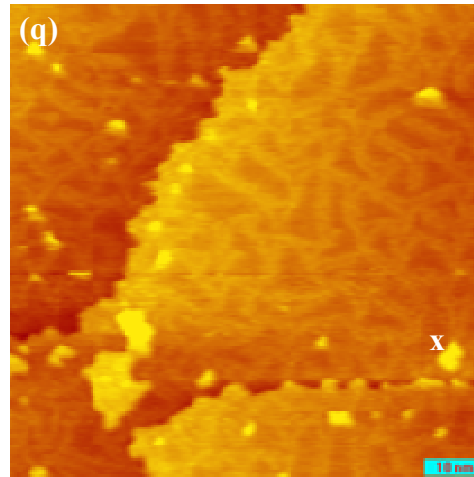
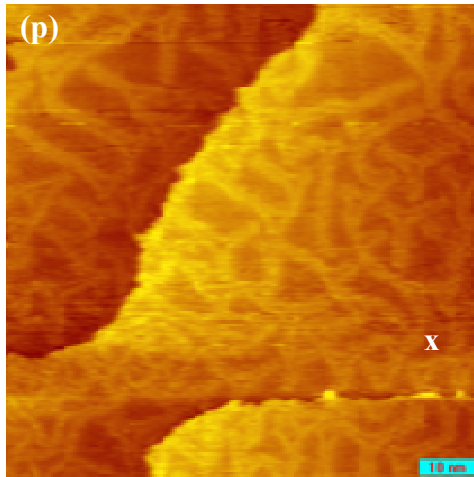
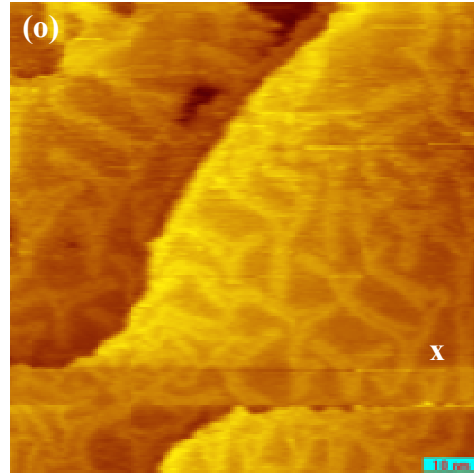
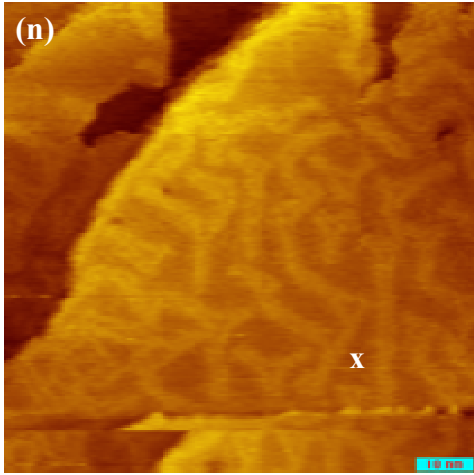
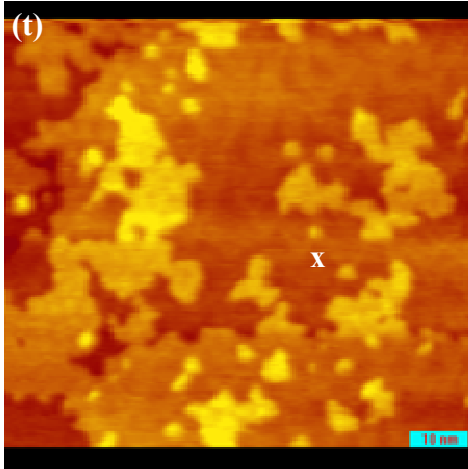


Fig. A.1 (a) Stress-Thickness (N/m) vs. thickness plot. Line 1 and Line 2 correspond to the slopes of the first segment and the second through the fourth repeating segments, respectively. 10% error bar is located at the peak. (b)~(t) corresponding STM images showing Cu coverage increase and surface structure development.









APPENDIX B
COPYRIGHT PERMISSIONS

PERMISSION INVOICE

Inv. # P03B 20964

January 18, 2012

Jungwoo Nah
8948 E Dahlia Dr.
Scottsdale, AZ 85260



**CAMBRIDGE
UNIVERSITY PRESS**

32 Avenue of the Americas
New York, NY 10013-2473, USA

www.cambridge.org

Telephone 212 924 3900
Fax 212 691 3239

REFERENCE

ISBN: HB 9780521822817 PB Other
Author: L. B. Freund and S. Suresh
Title: THIN FILM MATERIALS: STRESS, DEFECT FORMATION AND SURFACE EVOLUTION
Selection/pp.: Fig. 2. 4 in Page 107

Additional: Copyright © 2003 L. B. Freund and S. Suresh. Reprinted with the permission of Cambridge University Press.

USE

Reprint Title: Stress and Structure Evolution during Cu/Au(111) - (22x√3) Heteroepitaxy: An In-Situ Study
Publisher: Arizona State University
Format: dissertation / thesis
Quantity (Limit*): 100
Avail. Date: 2012

RIGHTS/ACKNOWLEDGEMENT

Permission is granted for nonexclusive rights throughout the World in the English language for interior text editorial use in the format described above only, including non-profit editions for the blind and handicapped. Please fully acknowledge our material and indicate the copyright notice as it appears in our publication, followed by the phrase "Reprinted with the permission of Cambridge University Press."
All requests from third parties to reproduce this material must be forwarded to Cambridge University Press.

FEES/RESTRICTIONS

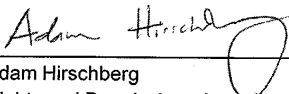
\$0.00

*You must re-apply for permission if this print run is exceeded. This permission is restricted to the indicated format and excludes reproduction in any other medium; for additional use, you must apply for permission separately. This permission does not allow reprinting of any material copyrighted by or credited in our publication to another source; Cambridge disclaims all liability in connection with the use of such material without proper consent. A COPY OF THIS INVOICE MUST ACCOMPANY PAYMENT. Payment is due upon publication or within 12 months, whichever is sooner. Make check payable to Cambridge University Press, Attn: Rights and Permissions. (CUP Fed. I.D. #: 13-1599108.)

This permission does not supersede permission that may be required from the original source indicated in our publication.

This permission requires that you send zero (0) copies of your publication directly to our author and zero (0) copy of your publication to this office upon availability.

Authorization:


Adam Hirschberg
Rights and Permissions Associate
ahirschberg@cambridge.org



Jungwoo Nah <jnah1@asu.edu>

copyright permission

2 messages

Jungwoo Nah <jnah1@asu.edu>

Fri, Jan 13, 2012 at 12:25 AM

To: mitoh6@yahoo.co.jp

Dear Dr. Makoto Itoh,

I am completing a doctoral dissertation at Arizona State University entitled "Stress and Structure Evolution during Cu/Au(111) - (22x\3) Heteroepitaxy: An In-Situ Study with UHV-STM."

I would like to obtain your permission to reprint in my dissertation the figure of DAS model of Si(111)-(7x7) at your website <http://www.geocities.jp/mitoh6/index.html>.

Also, could you allow me to add some red lines (for dimers) and letters (to show stacking sequence in the cross section figure).

If you want to see the figure with the added lines and letters, I can send it to you.

I would appreciate a response by Wednesday, January 18, 2012.

Thank you very much

Jungwoo Nah
Research Assistant
Friesen Research Group
Arizona State University

Itoh <mitoh6@yahoo.co.jp>

Fri, Jan 13, 2012 at 8:02 AM

To: Jungwoo Nah <jnah1@asu.edu>

Dear Mr./Ms. Jungwoo Nah,

Thank you very much for your inquiry.

Please use the figure as you like.

It is enough to mention the URL address from where you get the original.

After you finish your PhD, you can submit your thesis to Progress of Surface Science. It may be handy to have a reprint of a thesis in your job hunting.

Yours sincerely,
Makoto Itoh



Jungwoo Nah <jnah1@asu.edu>

copyright permission

4 messages

Jungwoo Nah <jnah1@asu.edu>

Thu, Jan 12, 2012 at 11:32 PM

To: rijsewijk@physics.leidenuniv.nl

Dear Sir or Madam,

I am completing a doctoral dissertation at Arizona State University entitled "Stress and Structure Evolution during Cu/Au(111) - (22x√3) Heteroepitaxy: An In-Situ Study with UHV-STM."

I would like to obtain your permission to reprint in my dissertation one figure (showing the exponential relation between tunneling current, I and distance, d)

at your website <http://www.physics.leidenuniv.nl/sections/cm/tp/>.

I would appreciate a response by Wednesday, January 18, 2011,

Jungwoo Nah
Research Assistant
Friesen Research Group
Arizona State University
Phone: [480-965-1061](tel:480-965-1061)
e-mail: jungwoo.nah@asu.edu

Rijsewijk, E. van <Rijsewijk@physics.leidenuniv.nl>

Thu, Jan 19, 2012 at 6:09 AM

To: Jungwoo Nah <jnah1@asu.edu>

Dear Jungwoo Nah,

Herewith we give you permission to reprint the figure (showing the exponential relation between tunneling current, I and distance, d)

from our website.

I wish you success with the doctoral dissertation.

Yours sincerely,

Ellie van Rijsewijk

Leiden University/ LION
Secretaries Office Condensed Matter (151/OORT)
P.O. Box 9504
2300 RA Leiden
The Netherlands

[+31.\(0\) 71 5275480](tel:+31715275480) (tel)

[+31.\(0\) 71 5275404](tel:+31715275404) (fax)

rijsewijk@physics.leidenuniv.nl

January 18, 2012

Jungwoo Nah
Research Assistant
Friesen Research Group
Arizona State University

Ref # 10996

Thank you for your permission request dated on January 12, 2012. We are pleased to grant you a non-exclusive, non-transferable permission, English rights, limited to **print and electronic format**, provided you meet the criteria outlined below. Permission is for a one-time use and does not include permission for future editions, updates, databases, translations, or any other matters. Permission must be sought for each additional use. This permission does not include the right to modify APS material.

Please print the required copyright credit line on the first page that the material appears: "Reprinted (abstract/excerpt/figure) with permission from [FULL REFERENCE CITATION] as follows: authors names, journal title, volume number, page number and year of publication. Copyright (YEAR) by the American Physical Society."

The following language must appear somewhere on the website: "Readers may view, browse, and/or download material for temporary copying purposes only, provided these uses are for noncommercial personal purposes. Except as provided by law, this material may not be further reproduced, distributed, transmitted, modified, adapted, performed, displayed, published, or sold in whole or part, without prior written permission from the American Physical Society."

Provide a hyperlink from the reprinted APS material (the hyperlink may be embedded in the copyright credit line). APS's link manager technology makes it convenient and easy to provide links to individual articles in APS journals. For information, see: <http://link.aps.org/>

You must also obtain permission from at least one of the authors for each separate work, if you haven't done so already. The author's name and address can be found on the first page of the published Article.

Use of the APS material must not imply any endorsement by the American Physical Society.

Permission is granted for use of the following APS material only

Fig. 1, PRL76, 3782 (1996)

Fig. 1, PRB56, 10518 (1997)

Fig. 1a, 2a, PRB49, 2997 (1994)

Fig. 1, PRL74, 754 (1995)

Fig. 1a, 2, PRL92, 116102 (2004)

Fig. 2, PRL95, 166106(2005)

Fig. 1, PRB31, 805 (1985)

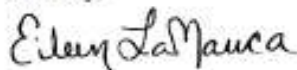
Fig. 1a, PRL104, 146101 (2010)

Permission is limited to the single title specified or single edition of the publication as follows:

A thesis entitled "Stress and Structure Evolution during Cu/Au(111) - (22x3) Heteroepitaxy: An In-Situ Study with UHV-STM." to be published by Arizona State University.

If you have any questions, please refer to the Copyright FAQ at: <http://publish.aps.org/copyrightFAQ.html> or send an email to assocpub@aps.org

Sincerely,



Eileen LaManca
Publications Marketing Coordinator

ELSEVIER LICENSE TERMS AND CONDITIONS

Jan 17, 2012

This is a License Agreement between Jungwoo Nah ("You") and Elsevier ("Elsevier") provided by Copyright Clearance Center ("CCC"). The license consists of your order details, the terms and conditions provided by Elsevier, and the payment terms and conditions.

All payments must be made in full to CCC. For payment instructions, please see information listed at the bottom of this form.

Supplier	Elsevier Limited The Boulevard, Langford Lane Kidlington, Oxford, OX5 1GB, UK
Registered Company Number	1982084
Customer name	Jungwoo Nah
Customer address	8948 E Dahlia Dr Scottsdale, AZ 85260
License number	2826781317582
License date	Jan 12, 2012
Licensed content publisher	Elsevier
Licensed content publication	Surface Science
Licensed content title	Herringbone and triangular patterns of dislocations in Ag, Au, and AgAu alloy films on Ru(0001)
Licensed content author	W.L. Ling, J.C. Hamilton, K. Thürmer, G.E. Thayer, J. de la Figuera, R.Q. Hwang, C.B. Carter, N.C. Bartelt, K.F. McCarty
Licensed content date	1 May 2006
Licensed content volume number	600
Licensed content issue number	9
Number of pages	23
Start Page	1735
End Page	1757
Type of Use	reuse in a thesis/dissertation
Portion	figures/tables/illustrations

Number of figures/tables/illustrations	3
Format	both print and electronic
Are you the author of this Elsevier article?	No
Will you be translating?	No
Order reference number	None
Title of your thesis/dissertation	Stress and Structure Evolution during Cu/Au(111) - (22x√3) Heteroepitaxy: An In-Situ Study with UHV-STM
Expected completion date	Feb 2012
Estimated size (number of pages)	130
Elsevier VAT number	GB 494 6272 12
Permissions price	0.00 USD
VAT/Local Sales Tax	0.0 USD / 0.0 GBP
Total	0.00 USD

Terms and Conditions

INTRODUCTION

1. The publisher for this copyrighted material is Elsevier. By clicking "accept" in connection with completing this licensing transaction, you agree that the following terms and conditions apply to this transaction (along with the Billing and Payment terms and conditions established by Copyright Clearance Center, Inc. ("CCC"), at the time that you opened your Rightslink account and that are available at any time at <http://myaccount.copyright.com>).

GENERAL TERMS

- Elsevier hereby grants you permission to reproduce the aforementioned material subject to the terms and conditions indicated.
- Acknowledgement: If any part of the material to be used (for example, figures) has appeared in our publication with credit or acknowledgement to another source, permission must also be sought from that source. If such permission is not obtained then that material may not be included in your publication/copies. Suitable acknowledgement to the source must be made, either as a footnote or in a reference list at the end of your publication, as follows:
 "Reprinted from Publication title, Vol /edition number, Author(s), Title of article / title of chapter, Pages No., Copyright (Year), with permission from Elsevier [OR APPLICABLE SOCIETY COPYRIGHT OWNER]." Also Lancet special credit -
 "Reprinted from The Lancet, Vol. number, Author(s), Title of article, Pages No., Copyright (Year), with permission from Elsevier."
- Reproduction of this material is confined to the purpose and/or media for which permission is hereby given.
- Altering/Modifying Material: Not Permitted. However figures and illustrations may be altered/adapted minimally to serve your work. Any other abbreviations, additions, deletions and/or any other alterations shall be made only with prior written authorization of Elsevier Ltd. (Please contact Elsevier at permissions@elsevier.com)

6. If the permission fee for the requested use of our material is waived in this instance, please be advised that your future requests for Elsevier materials may attract a fee.
7. Reservation of Rights: Publisher reserves all rights not specifically granted in the combination of (i) the license details provided by you and accepted in the course of this licensing transaction, (ii) these terms and conditions and (iii) CCC's Billing and Payment terms and conditions.
8. License Contingent Upon Payment: While you may exercise the rights licensed immediately upon issuance of the license at the end of the licensing process for the transaction, provided that you have disclosed complete and accurate details of your proposed use, no license is finally effective unless and until full payment is received from you (either by publisher or by CCC) as provided in CCC's Billing and Payment terms and conditions. If full payment is not received on a timely basis, then any license preliminarily granted shall be deemed automatically revoked and shall be void as if never granted. Further, in the event that you breach any of these terms and conditions or any of CCC's Billing and Payment terms and conditions, the license is automatically revoked and shall be void as if never granted. Use of materials as described in a revoked license, as well as any use of the materials beyond the scope of an unrevoked license, may constitute copyright infringement and publisher reserves the right to take any and all action to protect its copyright in the materials.
9. Warranties: Publisher makes no representations or warranties with respect to the licensed material.
10. Indemnity: You hereby indemnify and agree to hold harmless publisher and CCC, and their respective officers, directors, employees and agents, from and against any and all claims arising out of your use of the licensed material other than as specifically authorized pursuant to this license.
11. No Transfer of License: This license is personal to you and may not be sublicensed, assigned, or transferred by you to any other person without publisher's written permission.
12. No Amendment Except in Writing: This license may not be amended except in a writing signed by both parties (or, in the case of publisher, by CCC on publisher's behalf).
13. Objection to Contrary Terms: Publisher hereby objects to any terms contained in any purchase order, acknowledgment, check endorsement or other writing prepared by you, which terms are inconsistent with these terms and conditions or CCC's Billing and Payment terms and conditions. These terms and conditions, together with CCC's Billing and Payment terms and conditions (which are incorporated herein), comprise the entire agreement between you and publisher (and CCC) concerning this licensing transaction. In the event of any conflict between your obligations established by these terms and conditions and those established by CCC's Billing and Payment terms and conditions, these terms and conditions shall control.
14. Revocation: Elsevier or Copyright Clearance Center may deny the permissions described in this License at their sole discretion, for any reason or no reason, with a full refund payable to you. Notice of such denial will be made using the contact information provided by you. Failure to receive such notice will not alter or invalidate the denial. In no event will Elsevier or Copyright Clearance Center be responsible or liable for any costs, expenses or damage incurred by you as a result of a denial of your permission request, other than a refund of the amount(s) paid by you to Elsevier and/or Copyright Clearance Center for denied permissions.

LIMITED LICENSE

The following terms and conditions apply only to specific license types:

15. **Translation:** This permission is granted for non-exclusive world **English** rights only unless your license was granted for translation rights. If you licensed translation rights you may only translate this content into the languages you requested. A professional translator must perform all translations and reproduce the content word for word preserving the integrity of the article. If this license is to re-use 1 or 2 figures then permission is granted for non-exclusive world rights in all languages.

16. **Website:** The following terms and conditions apply to electronic reserve and author websites:

Electronic reserve: If licensed material is to be posted to website, the web site is to be password-protected and made available only to bona fide students registered on a relevant course if:

This license was made in connection with a course,

This permission is granted for 1 year only. You may obtain a license for future website posting,

All content posted to the web site must maintain the copyright information line on the bottom of each image,

A hyper-text must be included to the Homepage of the journal from which you are licensing at <http://www.sciencedirect.com/science/journal/xxxxx> or the Elsevier homepage for books at <http://www.elsevier.com> , and

Central Storage: This license does not include permission for a scanned version of the material to be stored in a central repository such as that provided by Heron/XanEdu.

17. **Author website** for journals with the following additional clauses:

All content posted to the web site must maintain the copyright information line on the bottom of each image, and

the permission granted is limited to the personal version of your paper. You are not allowed to download and post the published electronic version of your article (whether PDF or HTML, proof or final version), nor may you scan the printed edition to create an electronic version,

A hyper-text must be included to the Homepage of the journal from which you are licensing at <http://www.sciencedirect.com/science/journal/xxxxx> . As part of our normal production process, you will receive an e-mail notice when your article appears on Elsevier's online service ScienceDirect (www.sciencedirect.com).

That e-mail will include the article's Digital Object Identifier (DOI). This number provides the electronic link to the published article and should be included in the posting of your personal version. We ask that you wait until you receive this e-mail and have the DOI to do any posting.

Central Storage: This license does not include permission for a scanned version of the material to be stored in a central repository such as that provided by Heron/XanEdu.

18. **Author website** for books with the following additional clauses:

Authors are permitted to place a brief summary of their work online only.

A hyper-text must be included to the Elsevier homepage at <http://www.elsevier.com>

All content posted to the web site must maintain the copyright information line on the bottom of each image

You are not allowed to download and post the published electronic version of your chapter, nor may you scan the printed edition to create an electronic version.

Central Storage: This license does not include permission for a scanned version of the material to be stored in a central repository such as that provided by

Heron/XanEdu.

19. **Website** (regular and for author): A hyper-text must be included to the Homepage of the journal from which you are licensing at <http://www.sciencedirect.com/science/journal/xxxxx>. or for books to the Elsevier homepage at <http://www.elsevier.com>

20. **Thesis/Dissertation**: If your license is for use in a thesis/dissertation your thesis may be submitted to your institution in either print or electronic form. Should your thesis be published commercially, please reapply for permission. These requirements include permission for the Library and Archives of Canada to supply single copies, on demand, of the complete thesis and include permission for UMI to supply single copies, on demand, of the complete thesis. Should your thesis be published commercially, please reapply for permission.

21. **Other Conditions**:

v1.6

If you would like to pay for this license now, please remit this license along with your payment made payable to "COPYRIGHT CLEARANCE CENTER" otherwise you will be invoiced within 48 hours of the license date. Payment should be in the form of a check or money order referencing your account number and this invoice number RLNK500698473.

Once you receive your invoice for this order, you may pay your invoice by credit card. Please follow instructions provided at that time.

Make Payment To:
Copyright Clearance Center
Dept 001
P.O. Box 843006
Boston, MA 02284-3006

For suggestions or comments regarding this order, contact RightsLink Customer Support: customercare@copyright.com or +1-877-622-5543 (toll free in the US) or +1-978-646-2777.

Gratis licenses (referencing \$0 in the Total field) are free. Please retain this printable license for your reference. No payment is required.

ELSEVIER LICENSE

TERMS AND CONDITIONS

Jan 17, 2012

This is a License Agreement between Jungwoo Nah ("You") and Elsevier ("Elsevier") provided by Copyright Clearance Center ("CCC"). The license consists of your order details, the terms and conditions provided by Elsevier, and the payment terms and conditions.

All payments must be made in full to CCC. For payment instructions, please see information listed at the bottom of this form.

Supplier	Elsevier Limited The Boulevard, Langford Lane Kidlington, Oxford, OX5 1GB, UK
Registered Company Number	1982084
Customer name	Jungwoo Nah
Customer address	8948 E Dahlia Dr Scottsdale, AZ 85260
License number	2827111407631
License date	Jan 13, 2012
Licensed content publisher	Elsevier
Licensed content publication	Surface Science
Licensed content title	Initial stages of ZrO ₂ chemical vapor deposition on Si(100)-(2×1) from zirconium tetra- <i>tert</i> -butoxide
Licensed content author	P.G. Karlsson, E. Göthelid, J.H. Richter, A. Sandell
Licensed content date	15 May 2008
Licensed content volume number	602
Licensed content issue number	10
Number of pages	7
Start Page	1803
End Page	1809
Type of Use	reuse in a thesis/dissertation
Portion	figures/tables/illustrations

Number of figures/tables/illustrations	1
Format	both print and electronic
Are you the author of this Elsevier article?	No
Will you be translating?	No
Order reference number	None
Title of your thesis/dissertation	Stress and Structure Evolution during Cu/Au(111) - (22x√3) Heteroepitaxy: An In-Situ Study with UHV-STM
Expected completion date	Feb 2012
Estimated size (number of pages)	130
Elsevier VAT number	GB 494 6272 12
Permissions price	0.00 USD
VAT/Local Sales Tax	0.0 USD / 0.0 GBP
Total	0.00 USD
Terms and Conditions	

INTRODUCTION

1. The publisher for this copyrighted material is Elsevier. By clicking "accept" in connection with completing this licensing transaction, you agree that the following terms and conditions apply to this transaction (along with the Billing and Payment terms and conditions established by Copyright Clearance Center, Inc. ("CCC"), at the time that you opened your Rightslink account and that are available at any time at <http://myaccount.copyright.com>).

GENERAL TERMS

2. Elsevier hereby grants you permission to reproduce the aforementioned material subject to the terms and conditions indicated.
3. Acknowledgement: If any part of the material to be used (for example, figures) has appeared in our publication with credit or acknowledgement to another source, permission must also be sought from that source. If such permission is not obtained then that material may not be included in your publication/copies. Suitable acknowledgement to the source must be made, either as a footnote or in a reference list at the end of your publication, as follows:
 "Reprinted from Publication title, Vol /edition number, Author(s), Title of article / title of chapter, Pages No., Copyright (Year), with permission from Elsevier [OR APPLICABLE SOCIETY COPYRIGHT OWNER]." Also Lancet special credit -
 "Reprinted from The Lancet, Vol. number, Author(s), Title of article, Pages No., Copyright (Year), with permission from Elsevier."
4. Reproduction of this material is confined to the purpose and/or media for which permission is hereby given.
5. Altering/Modifying Material: Not Permitted. However figures and illustrations may be altered/adapted minimally to serve your work. Any other abbreviations, additions, deletions and/or any other alterations shall be made only with prior written authorization of Elsevier Ltd. (Please contact Elsevier at permissions@elsevier.com)

6. If the permission fee for the requested use of our material is waived in this instance, please be advised that your future requests for Elsevier materials may attract a fee.
7. Reservation of Rights: Publisher reserves all rights not specifically granted in the combination of (i) the license details provided by you and accepted in the course of this licensing transaction, (ii) these terms and conditions and (iii) CCC's Billing and Payment terms and conditions.
8. License Contingent Upon Payment: While you may exercise the rights licensed immediately upon issuance of the license at the end of the licensing process for the transaction, provided that you have disclosed complete and accurate details of your proposed use, no license is finally effective unless and until full payment is received from you (either by publisher or by CCC) as provided in CCC's Billing and Payment terms and conditions. If full payment is not received on a timely basis, then any license preliminarily granted shall be deemed automatically revoked and shall be void as if never granted. Further, in the event that you breach any of these terms and conditions or any of CCC's Billing and Payment terms and conditions, the license is automatically revoked and shall be void as if never granted. Use of materials as described in a revoked license, as well as any use of the materials beyond the scope of an unrevoked license, may constitute copyright infringement and publisher reserves the right to take any and all action to protect its copyright in the materials.
9. Warranties: Publisher makes no representations or warranties with respect to the licensed material.
10. Indemnity: You hereby indemnify and agree to hold harmless publisher and CCC, and their respective officers, directors, employees and agents, from and against any and all claims arising out of your use of the licensed material other than as specifically authorized pursuant to this license.
11. No Transfer of License: This license is personal to you and may not be sublicensed, assigned, or transferred by you to any other person without publisher's written permission.
12. No Amendment Except in Writing: This license may not be amended except in a writing signed by both parties (or, in the case of publisher, by CCC on publisher's behalf).
13. Objection to Contrary Terms: Publisher hereby objects to any terms contained in any purchase order, acknowledgment, check endorsement or other writing prepared by you, which terms are inconsistent with these terms and conditions or CCC's Billing and Payment terms and conditions. These terms and conditions, together with CCC's Billing and Payment terms and conditions (which are incorporated herein), comprise the entire agreement between you and publisher (and CCC) concerning this licensing transaction. In the event of any conflict between your obligations established by these terms and conditions and those established by CCC's Billing and Payment terms and conditions, these terms and conditions shall control.
14. Revocation: Elsevier or Copyright Clearance Center may deny the permissions described in this License at their sole discretion, for any reason or no reason, with a full refund payable to you. Notice of such denial will be made using the contact information provided by you. Failure to receive such notice will not alter or invalidate the denial. In no event will Elsevier or Copyright Clearance Center be responsible or liable for any costs, expenses or damage incurred by you as a result of a denial of your permission request, other than a refund of the amount(s) paid by you to Elsevier and/or Copyright Clearance Center for denied permissions.

LIMITED LICENSE

The following terms and conditions apply only to specific license types:

15. **Translation:** This permission is granted for non-exclusive world **English** rights only unless your license was granted for translation rights. If you licensed translation rights you may only translate this content into the languages you requested. A professional translator must perform all translations and reproduce the content word for word preserving the integrity of the article. If this license is to re-use 1 or 2 figures then permission is granted for non-exclusive world rights in all languages.

16. **Website:** The following terms and conditions apply to electronic reserve and author websites:

Electronic reserve: If licensed material is to be posted to website, the web site is to be password-protected and made available only to bona fide students registered on a relevant course if:

This license was made in connection with a course,

This permission is granted for 1 year only. You may obtain a license for future website posting,

All content posted to the web site must maintain the copyright information line on the bottom of each image,

A hyper-text must be included to the Homepage of the journal from which you are licensing at <http://www.sciencedirect.com/science/journal/xxxxx> or the Elsevier homepage for books at <http://www.elsevier.com> , and

Central Storage: This license does not include permission for a scanned version of the material to be stored in a central repository such as that provided by Heron/XanEdu.

17. **Author website** for journals with the following additional clauses:

All content posted to the web site must maintain the copyright information line on the bottom of each image, and

the permission granted is limited to the personal version of your paper. You are not allowed to download and post the published electronic version of your article (whether PDF or HTML, proof or final version), nor may you scan the printed edition to create an electronic version,

A hyper-text must be included to the Homepage of the journal from which you are licensing at <http://www.sciencedirect.com/science/journal/xxxxx> , As part of our normal production process, you will receive an e-mail notice when your article appears on Elsevier's online service ScienceDirect (www.sciencedirect.com).

That e-mail will include the article's Digital Object Identifier (DOI). This number provides the electronic link to the published article and should be included in the posting of your personal version. We ask that you wait until you receive this e-mail and have the DOI to do any posting.

Central Storage: This license does not include permission for a scanned version of the material to be stored in a central repository such as that provided by Heron/XanEdu.

18. **Author website** for books with the following additional clauses:

Authors are permitted to place a brief summary of their work online only.

A hyper-text must be included to the Elsevier homepage at <http://www.elsevier.com>

All content posted to the web site must maintain the copyright information line on the bottom of each image

You are not allowed to download and post the published electronic version of your chapter, nor may you scan the printed edition to create an electronic version.

Central Storage: This license does not include permission for a scanned version of the material to be stored in a central repository such as that provided by

Heron/XanEdu.

19. **Website** (regular and for author): A hyper-text must be included to the Homepage of the journal from which you are licensing at <http://www.sciencedirect.com/science/journal/xxxx>. or for books to the Elsevier homepage at <http://www.elsevier.com>

20. **Thesis/Dissertation**: If your license is for use in a thesis/dissertation your thesis may be submitted to your institution in either print or electronic form. Should your thesis be published commercially, please reapply for permission. These requirements include permission for the Library and Archives of Canada to supply single copies, on demand, of the complete thesis and include permission for UMI to supply single copies, on demand, of the complete thesis. Should your thesis be published commercially, please reapply for permission.

21. **Other Conditions**:

v1.6

If you would like to pay for this license now, please remit this license along with your payment made payable to "COPYRIGHT CLEARANCE CENTER" otherwise you will be invoiced within 48 hours of the license date. Payment should be in the form of a check or money order referencing your account number and this invoice number RLNK500698954.

Once you receive your invoice for this order, you may pay your invoice by credit card. Please follow instructions provided at that time.

Make Payment To:
Copyright Clearance Center
Dept 001
P.O. Box 843006
Boston, MA 02284-3006

For suggestions or comments regarding this order, contact RightsLink Customer Support: customercare@copyright.com or +1-877-622-5543 (toll free in the US) or +1-978-646-2777.

Gratis licenses (referencing \$0 in the Total field) are free. Please retain this printable license for your reference. No payment is required.

SPRINGER LICENSE TERMS AND CONDITIONS

Jan 17, 2012

This is a License Agreement between Jungwoo Nah ("You") and Springer ("Springer") provided by Copyright Clearance Center ("CCC"). The license consists of your order details, the terms and conditions provided by Springer, and the payment terms and conditions.

All payments must be made in full to CCC. For payment instructions, please see information listed at the bottom of this form.

License Number	2826930719034
License date	Jan 13, 2012
Licensed content publisher	Springer
Licensed content publication	Springer eBook
Licensed content title	SCANNING TUNNELING SPECTROSCOPY (STS)
Licensed content author	K.W. Hipps
Licensed content date	Feb 15, 2007
Type of Use	Thesis/Dissertation
Portion	Figures
Author of this Springer article	No
Order reference number	None
Title of your thesis / dissertation	Stress and Structure Evolution during Cu/Au(111) - (22x√3) Heteroepitaxy: An In-Situ Study with UHV-STM
Expected completion date	Feb 2012
Estimated size(pages)	130
Total	0.00 USD

Terms and Conditions

Introduction

The publisher for this copyrighted material is Springer Science + Business Media. By clicking "accept" in connection with completing this licensing transaction, you agree that the following terms and conditions apply to this transaction (along with the Billing and Payment terms and conditions established by Copyright Clearance Center, Inc. ("CCC"), at the time that you opened your Rightslink account and that are

available at any time at <http://myaccount.copyright.com>).

Limited License

With reference to your request to reprint in your thesis material on which Springer Science and Business Media control the copyright, permission is granted, free of charge, for the use indicated in your enquiry. Licenses are for one-time use only with a maximum distribution equal to the number that you identified in the licensing process.

This License includes use in an electronic form, provided it is password protected or on the university's intranet, destined to microfilming by UMI and University repository. For any other electronic use, please contact Springer at

(permissions.dordrecht@springer.com or permissions.heidelberg@springer.com)

The material can only be used for the purpose of defending your thesis, and with a maximum of 100 extra copies in paper.

Although Springer holds copyright to the material and is entitled to negotiate on rights, this license is only valid, provided permission is also obtained from the (co) author (address is given with the article/chapter) and provided it concerns original material which does not carry references to other sources (if material in question appears with credit to another source, authorization from that source is required as well). Permission free of charge on this occasion does not prejudice any rights we might have to charge for reproduction of our copyrighted material in the future.

Altering/Modifying Material: Not Permitted

However figures and illustrations may be altered minimally to serve your work. Any other abbreviations, additions, deletions and/or any other alterations shall be made only with prior written authorization of the author(s) and/or Springer Science + Business Media. (Please contact Springer at permissions.dordrecht@springer.com or permissions.heidelberg@springer.com)

Reservation of Rights

Springer Science + Business Media reserves all rights not specifically granted in the combination of (i) the license details provided by you and accepted in the course of this licensing transaction, (ii) these terms and conditions and (iii) CCC's Billing and Payment terms and conditions.

Copyright Notice:

Please include the following copyright citation referencing the publication in which the material was originally published. Where wording is within brackets, please include verbatim.

"With kind permission from Springer Science+Business Media: <book/journal title, chapter/article title, volume, year of publication, page, name(s) of author(s), figure number(s), and any original (first) copyright notice displayed with material>."

Warranties: Springer Science + Business Media makes no representations or warranties with respect to the licensed material.

Indemnity

You hereby indemnify and agree to hold harmless Springer Science + Business Media and CCC, and their respective officers, directors, employees and agents, from and against any and all claims arising out of your use of the licensed material other than as specifically authorized pursuant to this license.

No Transfer of License

This license is personal to you and may not be sublicensed, assigned, or transferred by you to any other person without Springer Science + Business Media's written permission.

No Amendment Except in Writing

This license may not be amended except in a writing signed by both parties (or, in the case of Springer Science + Business Media, by CCC on Springer Science + Business

Media's behalf).

Objection to Contrary Terms

Springer Science + Business Media hereby objects to any terms contained in any purchase order, acknowledgment, check endorsement or other writing prepared by you, which terms are inconsistent with these terms and conditions or CCC's Billing and Payment terms and conditions. These terms and conditions, together with CCC's Billing and Payment terms and conditions (which are incorporated herein), comprise the entire agreement between you and Springer Science + Business Media (and CCC) concerning this licensing transaction. In the event of any conflict between your obligations established by these terms and conditions and those established by CCC's Billing and Payment terms and conditions, these terms and conditions shall control.

Jurisdiction

All disputes that may arise in connection with this present License, or the breach thereof, shall be settled exclusively by the country's law in which the work was originally published.

Other terms and conditions:

v1.2

If you would like to pay for this license now, please remit this license along with your payment made payable to "COPYRIGHT CLEARANCE CENTER" otherwise you will be invoiced within 48 hours of the license date. Payment should be in the form of a check or money order referencing your account number and this invoice number RLNK500698637.

Once you receive your invoice for this order, you may pay your invoice by credit card. Please follow instructions provided at that time.

Make Payment To:

**Copyright Clearance Center
Dept 001
P.O. Box 843006
Boston, MA 02284-3006**

For suggestions or comments regarding this order, contact RightsLink Customer Support: customercare@copyright.com or +1-877-622-5543 (toll free in the US) or +1-978-646-2777.

Gratis licenses (referencing \$0 in the Total field) are free. Please retain this printable license for your reference. No payment is required.

ELSEVIER LICENSE TERMS AND CONDITIONS

Jan 17, 2012

This is a License Agreement between Jungwoo Nah ("You") and Elsevier ("Elsevier") provided by Copyright Clearance Center ("CCC"). The license consists of your order details, the terms and conditions provided by Elsevier, and the payment terms and conditions.

All payments must be made in full to CCC. For payment instructions, please see information listed at the bottom of this form.

Supplier	Elsevier Limited The Boulevard, Langford Lane Kidlington, Oxford, OX5 1GB, UK
Registered Company Number	1982084
Customer name	Jungwoo Nah
Customer address	8948 E Dahlia Dr Scottsdale, AZ 85260
License number	2826900113629
License date	Jan 13, 2012
Licensed content publisher	Elsevier
Licensed content publication	Materials Science and Engineering: A
Licensed content title	In-situ STM studies of strain-stabilized thin-film dislocation networks under applied stress
Licensed content author	Oliver Schaff, Andreas K. Schmid, Norm C. Bartelt, Juan de la Figuera, Robert Q. Hwang
Licensed content date	December 2001
Licensed content volume number	319–321
Licensed content issue number	None
Number of pages	5
Start Page	914
End Page	918
Type of Use	reuse in a thesis/dissertation
Intended publisher of new work	other
Portion	figures/tables/illustrations

Number of figures/tables/illustrations	1
Format	both print and electronic
Are you the author of this Elsevier article?	No
Will you be translating?	No
Order reference number	None
Title of your thesis/dissertation	Stress and Structure Evolution during Cu/Au(111) - (22x√3) Heteroepitaxy: An In-Situ Study with UHV-STM
Expected completion date	Feb 2012
Estimated size (number of pages)	130
Elsevier VAT number	GB 494 6272 12
Permissions price	0.00 USD
VAT/Local Sales Tax	0.0 USD / 0.0 GBP
Total	0.00 USD

Terms and Conditions

INTRODUCTION

1. The publisher for this copyrighted material is Elsevier. By clicking "accept" in connection with completing this licensing transaction, you agree that the following terms and conditions apply to this transaction (along with the Billing and Payment terms and conditions established by Copyright Clearance Center, Inc. ("CCC"), at the time that you opened your Rightslink account and that are available at any time at <http://myaccount.copyright.com>).

GENERAL TERMS

- Elsevier hereby grants you permission to reproduce the aforementioned material subject to the terms and conditions indicated.
- Acknowledgement: If any part of the material to be used (for example, figures) has appeared in our publication with credit or acknowledgement to another source, permission must also be sought from that source. If such permission is not obtained then that material may not be included in your publication/copies. Suitable acknowledgement to the source must be made, either as a footnote or in a reference list at the end of your publication, as follows:
 "Reprinted from Publication title, Vol /edition number, Author(s), Title of article / title of chapter, Pages No., Copyright (Year), with permission from Elsevier [OR APPLICABLE SOCIETY COPYRIGHT OWNER]." Also Lancet special credit -
 "Reprinted from The Lancet, Vol. number, Author(s), Title of article, Pages No., Copyright (Year), with permission from Elsevier."
- Reproduction of this material is confined to the purpose and/or media for which permission is hereby given.
- Altering/Modifying Material: Not Permitted. However figures and illustrations may be altered/adapted minimally to serve your work. Any other abbreviations, additions, deletions and/or any other alterations shall be made only with prior written authorization of Elsevier Ltd. (Please contact Elsevier at permissions@elsevier.com)
- If the permission fee for the requested use of our material is waived in this instance, please be advised that your future requests for Elsevier materials may

attract a fee.

7. **Reservation of Rights:** Publisher reserves all rights not specifically granted in the combination of (i) the license details provided by you and accepted in the course of this licensing transaction, (ii) these terms and conditions and (iii) CCC's Billing and Payment terms and conditions.

8. **License Contingent Upon Payment:** While you may exercise the rights licensed immediately upon issuance of the license at the end of the licensing process for the transaction, provided that you have disclosed complete and accurate details of your proposed use, no license is finally effective unless and until full payment is received from you (either by publisher or by CCC) as provided in CCC's Billing and Payment terms and conditions. If full payment is not received on a timely basis, then any license preliminarily granted shall be deemed automatically revoked and shall be void as if never granted. Further, in the event that you breach any of these terms and conditions or any of CCC's Billing and Payment terms and conditions, the license is automatically revoked and shall be void as if never granted. Use of materials as described in a revoked license, as well as any use of the materials beyond the scope of an unrevoked license, may constitute copyright infringement and publisher reserves the right to take any and all action to protect its copyright in the materials.

9. **Warranties:** Publisher makes no representations or warranties with respect to the licensed material.

10. **Indemnity:** You hereby indemnify and agree to hold harmless publisher and CCC, and their respective officers, directors, employees and agents, from and against any and all claims arising out of your use of the licensed material other than as specifically authorized pursuant to this license.

11. **No Transfer of License:** This license is personal to you and may not be sublicensed, assigned, or transferred by you to any other person without publisher's written permission.

12. **No Amendment Except in Writing:** This license may not be amended except in a writing signed by both parties (or, in the case of publisher, by CCC on publisher's behalf).

13. **Objection to Contrary Terms:** Publisher hereby objects to any terms contained in any purchase order, acknowledgment, check endorsement or other writing prepared by you, which terms are inconsistent with these terms and conditions or CCC's Billing and Payment terms and conditions. These terms and conditions, together with CCC's Billing and Payment terms and conditions (which are incorporated herein), comprise the entire agreement between you and publisher (and CCC) concerning this licensing transaction. In the event of any conflict between your obligations established by these terms and conditions and those established by CCC's Billing and Payment terms and conditions, these terms and conditions shall control.

14. **Revocation:** Elsevier or Copyright Clearance Center may deny the permissions described in this License at their sole discretion, for any reason or no reason, with a full refund payable to you. Notice of such denial will be made using the contact information provided by you. Failure to receive such notice will not alter or invalidate the denial. In no event will Elsevier or Copyright Clearance Center be responsible or liable for any costs, expenses or damage incurred by you as a result of a denial of your permission request, other than a refund of the amount(s) paid by you to Elsevier and/or Copyright Clearance Center for denied permissions.

LIMITED LICENSE

The following terms and conditions apply only to specific license types:

15. **Translation:** This permission is granted for non-exclusive world **English** rights only unless your license was granted for translation rights. If you licensed translation rights you may only translate this content into the languages you requested. A

professional translator must perform all translations and reproduce the content word for word preserving the integrity of the article. If this license is to re-use 1 or 2 figures then permission is granted for non-exclusive world rights in all languages.

16. **Website:** The following terms and conditions apply to electronic reserve and author websites:

Electronic reserve: If licensed material is to be posted to website, the web site is to be password-protected and made available only to bona fide students registered on a relevant course if:

This license was made in connection with a course,

This permission is granted for 1 year only. You may obtain a license for future website posting,

All content posted to the web site must maintain the copyright information line on the bottom of each image,

A hyper-text must be included to the Homepage of the journal from which you are licensing at <http://www.sciencedirect.com/science/journal/xxxxx> or the Elsevier homepage for books at <http://www.elsevier.com> , and

Central Storage: This license does not include permission for a scanned version of the material to be stored in a central repository such as that provided by Heron/XanEdu.

17. **Author website** for journals with the following additional clauses:

All content posted to the web site must maintain the copyright information line on the bottom of each image, and

the permission granted is limited to the personal version of your paper. You are not allowed to download and post the published electronic version of your article (whether PDF or HTML, proof or final version), nor may you scan the printed edition to create an electronic version,

A hyper-text must be included to the Homepage of the journal from which you are licensing at <http://www.sciencedirect.com/science/journal/xxxxx> , As part of our normal production process, you will receive an e-mail notice when your article appears on Elsevier's online service ScienceDirect (www.sciencedirect.com). That e-mail will include the article's Digital Object Identifier (DOI). This number provides the electronic link to the published article and should be included in the posting of your personal version. We ask that you wait until you receive this e-mail and have the DOI to do any posting.

Central Storage: This license does not include permission for a scanned version of the material to be stored in a central repository such as that provided by Heron/XanEdu.

18. **Author website** for books with the following additional clauses:

Authors are permitted to place a brief summary of their work online only.

A hyper-text must be included to the Elsevier homepage at <http://www.elsevier.com>

All content posted to the web site must maintain the copyright information line on the bottom of each image

You are not allowed to download and post the published electronic version of your chapter, nor may you scan the printed edition to create an electronic version.

Central Storage: This license does not include permission for a scanned version of the material to be stored in a central repository such as that provided by Heron/XanEdu.

19. **Website** (regular and for author): A hyper-text must be included to the Homepage of the journal from which you are licensing at <http://www.sciencedirect.com/science/journal/xxxxx> or for books to the Elsevier homepage at <http://www.elsevier.com>

20. **Thesis/Dissertation:** If your license is for use in a thesis/dissertation your thesis may be submitted to your institution in either print or electronic form. Should your thesis be published commercially, please reapply for permission. These requirements include permission for the Library and Archives of Canada to supply single copies, on demand, of the complete thesis and include permission for UMI to supply single copies, on demand, of the complete thesis. Should your thesis be published commercially, please reapply for permission.

21. **Other Conditions:**

v1.6

If you would like to pay for this license now, please remit this license along with your payment made payable to "COPYRIGHT CLEARANCE CENTER" otherwise you will be invoiced within 48 hours of the license date. Payment should be in the form of a check or money order referencing your account number and this invoice number RLNK500698589.

Once you receive your invoice for this order, you may pay your invoice by credit card. Please follow instructions provided at that time.

**Make Payment To:
Copyright Clearance Center
Dept 001
P.O. Box 843006
Boston, MA 02284-3006**

For suggestions or comments regarding this order, contact RightsLink Customer Support: customercare@copyright.com or +1-877-622-5543 (toll free in the US) or +1-978-646-2777.

Gratis licenses (referencing \$0 in the Total field) are free. Please retain this printable license for your reference. No payment is required.

ELSEVIER LICENSE

TERMS AND CONDITIONS

Jan 17, 2012

This is a License Agreement between Jungwoo Nah ("You") and Elsevier ("Elsevier") provided by Copyright Clearance Center ("CCC"). The license consists of your order details, the terms and conditions provided by Elsevier, and the payment terms and conditions.

All payments must be made in full to CCC. For payment instructions, please see information listed at the bottom of this form.

Supplier	Elsevier Limited The Boulevard, Langford Lane Kidlington, Oxford, OX5 1GB, UK
Registered Company Number	1982084
Customer name	Jungwoo Nah
Customer address	8948 E Dahlia Dr Scottsdale, AZ 85260
License number	2826861082693
License date	Jan 13, 2012
Licensed content publisher	Elsevier
Licensed content publication	Surface Science
Licensed content title	Step-structure dependent step-flow: models for the homoepitaxial growth at the atomic steps on Si(111)7 × 7
Licensed content author	Wataru Shimada, Hiroshi Tochiyama
Licensed content date	10 May 1994
Licensed content volume number	311
Licensed content issue number	1–2
Number of pages	19
Start Page	107
End Page	125
Type of Use	reuse in a thesis/dissertation
Portion	figures/tables/illustrations

Number of figures/tables/illustrations	1
Format	both print and electronic
Are you the author of this Elsevier article?	No
Will you be translating?	No
Order reference number	None
Title of your thesis/dissertation	Stress and Structure Evolution during Cu/Au(111) - (22x√3) Heteroepitaxy: An In-Situ Study with UHV-STM
Expected completion date	Feb 2012
Estimated size (number of pages)	130
Elsevier VAT number	GB 494 6272 12
Permissions price	0.00 USD
VAT/Local Sales Tax	0.0 USD / 0.0 GBP
Total	0.00 USD
Terms and Conditions	

INTRODUCTION

1. The publisher for this copyrighted material is Elsevier. By clicking "accept" in connection with completing this licensing transaction, you agree that the following terms and conditions apply to this transaction (along with the Billing and Payment terms and conditions established by Copyright Clearance Center, Inc. ("CCC"), at the time that you opened your Rightslink account and that are available at any time at <http://myaccount.copyright.com>).

GENERAL TERMS

- Elsevier hereby grants you permission to reproduce the aforementioned material subject to the terms and conditions indicated.
- Acknowledgement: If any part of the material to be used (for example, figures) has appeared in our publication with credit or acknowledgement to another source, permission must also be sought from that source. If such permission is not obtained then that material may not be included in your publication/copies. Suitable acknowledgement to the source must be made, either as a footnote or in a reference list at the end of your publication, as follows:
 "Reprinted from Publication title, Vol /edition number, Author(s), Title of article / title of chapter, Pages No., Copyright (Year), with permission from Elsevier [OR APPLICABLE SOCIETY COPYRIGHT OWNER]." Also Lancet special credit -
 "Reprinted from The Lancet, Vol. number, Author(s), Title of article, Pages No., Copyright (Year), with permission from Elsevier."
- Reproduction of this material is confined to the purpose and/or media for which permission is hereby given.
- Altering/Modifying Material: Not Permitted. However figures and illustrations may be altered/adapted minimally to serve your work. Any other abbreviations, additions, deletions and/or any other alterations shall be made only with prior written authorization of Elsevier Ltd. (Please contact Elsevier at permissions@elsevier.com)
- If the permission fee for the requested use of our material is waived in this

instance, please be advised that your future requests for Elsevier materials may attract a fee.

7. Reservation of Rights: Publisher reserves all rights not specifically granted in the combination of (i) the license details provided by you and accepted in the course of this licensing transaction, (ii) these terms and conditions and (iii) CCC's Billing and Payment terms and conditions.

8. License Contingent Upon Payment: While you may exercise the rights licensed immediately upon issuance of the license at the end of the licensing process for the transaction, provided that you have disclosed complete and accurate details of your proposed use, no license is finally effective unless and until full payment is received from you (either by publisher or by CCC) as provided in CCC's Billing and Payment terms and conditions. If full payment is not received on a timely basis, then any license preliminarily granted shall be deemed automatically revoked and shall be void as if never granted. Further, in the event that you breach any of these terms and conditions or any of CCC's Billing and Payment terms and conditions, the license is automatically revoked and shall be void as if never granted. Use of materials as described in a revoked license, as well as any use of the materials beyond the scope of an unrevoked license, may constitute copyright infringement and publisher reserves the right to take any and all action to protect its copyright in the materials.

9. Warranties: Publisher makes no representations or warranties with respect to the licensed material.

10. Indemnity: You hereby indemnify and agree to hold harmless publisher and CCC, and their respective officers, directors, employees and agents, from and against any and all claims arising out of your use of the licensed material other than as specifically authorized pursuant to this license.

11. No Transfer of License: This license is personal to you and may not be sublicensed, assigned, or transferred by you to any other person without publisher's written permission.

12. No Amendment Except in Writing: This license may not be amended except in a writing signed by both parties (or, in the case of publisher, by CCC on publisher's behalf).

13. Objection to Contrary Terms: Publisher hereby objects to any terms contained in any purchase order, acknowledgment, check endorsement or other writing prepared by you, which terms are inconsistent with these terms and conditions or CCC's Billing and Payment terms and conditions. These terms and conditions, together with CCC's Billing and Payment terms and conditions (which are incorporated herein), comprise the entire agreement between you and publisher (and CCC) concerning this licensing transaction. In the event of any conflict between your obligations established by these terms and conditions and those established by CCC's Billing and Payment terms and conditions, these terms and conditions shall control.

14. Revocation: Elsevier or Copyright Clearance Center may deny the permissions described in this License at their sole discretion, for any reason or no reason, with a full refund payable to you. Notice of such denial will be made using the contact information provided by you. Failure to receive such notice will not alter or invalidate the denial. In no event will Elsevier or Copyright Clearance Center be responsible or liable for any costs, expenses or damage incurred by you as a result of a denial of your permission request, other than a refund of the amount(s) paid by you to Elsevier and/or Copyright Clearance Center for denied permissions.

LIMITED LICENSE

The following terms and conditions apply only to specific license types:

15. **Translation:** This permission is granted for non-exclusive world **English** rights only unless your license was granted for translation rights. If you licensed translation

rights you may only translate this content into the languages you requested. A professional translator must perform all translations and reproduce the content word for word preserving the integrity of the article. If this license is to re-use 1 or 2 figures then permission is granted for non-exclusive world rights in all languages.

16. **Website:** The following terms and conditions apply to electronic reserve and author websites:

Electronic reserve: If licensed material is to be posted to website, the web site is to be password-protected and made available only to bona fide students registered on a relevant course if:

This license was made in connection with a course,

This permission is granted for 1 year only. You may obtain a license for future website posting,

All content posted to the web site must maintain the copyright information line on the bottom of each image,

A hyper-text must be included to the Homepage of the journal from which you are licensing at <http://www.sciencedirect.com/science/journal/xxxxx> or the Elsevier homepage for books at <http://www.elsevier.com> , and

Central Storage: This license does not include permission for a scanned version of the material to be stored in a central repository such as that provided by Heron/XanEdu.

17. **Author website** for journals with the following additional clauses:

All content posted to the web site must maintain the copyright information line on the bottom of each image, and

the permission granted is limited to the personal version of your paper. You are not allowed to download and post the published electronic version of your article (whether PDF or HTML, proof or final version), nor may you scan the printed edition to create an electronic version,

A hyper-text must be included to the Homepage of the journal from which you are licensing at <http://www.sciencedirect.com/science/journal/xxxxx> , As part of our normal production process, you will receive an e-mail notice when your article appears on Elsevier's online service ScienceDirect (www.sciencedirect.com). That e-mail will include the article's Digital Object Identifier (DOI). This number provides the electronic link to the published article and should be included in the posting of your personal version. We ask that you wait until you receive this e-mail and have the DOI to do any posting.

Central Storage: This license does not include permission for a scanned version of the material to be stored in a central repository such as that provided by Heron/XanEdu.

18. **Author website** for books with the following additional clauses:

Authors are permitted to place a brief summary of their work online only.

A hyper-text must be included to the Elsevier homepage at <http://www.elsevier.com>

All content posted to the web site must maintain the copyright information line on the bottom of each image

You are not allowed to download and post the published electronic version of your chapter, nor may you scan the printed edition to create an electronic version.

Central Storage: This license does not include permission for a scanned version of the material to be stored in a central repository such as that provided by Heron/XanEdu.

19. **Website** (regular and for author): A hyper-text must be included to the Homepage of the journal from which you are licensing at <http://www.sciencedirect.com/science/journal/xxxxx> or for books to the Elsevier

homepage at <http://www.elsevier.com>

20. **Thesis/Dissertation:** If your license is for use in a thesis/dissertation your thesis may be submitted to your institution in either print or electronic form. Should your thesis be published commercially, please reapply for permission. These requirements include permission for the Library and Archives of Canada to supply single copies, on demand, of the complete thesis and include permission for UMI to supply single copies, on demand, of the complete thesis. Should your thesis be published commercially, please reapply for permission.

21. **Other Conditions:**

v1.6

If you would like to pay for this license now, please remit this license along with your payment made payable to "COPYRIGHT CLEARANCE CENTER" otherwise you will be invoiced within 48 hours of the license date. Payment should be in the form of a check or money order referencing your account number and this invoice number RLNK500698547.

Once you receive your invoice for this order, you may pay your invoice by credit card. Please follow instructions provided at that time.

**Make Payment To:
Copyright Clearance Center
Dept 001
P.O. Box 843006
Boston, MA 02284-3006**

For suggestions or comments regarding this order, contact RightsLink Customer Support: customercare@copyright.com or +1-877-622-5543 (toll free in the US) or +1-978-646-2777.

Gratis licenses (referencing \$0 in the Total field) are free. Please retain this printable license for your reference. No payment is required.



RightsLink®

[Home](#)[Account Info](#)[Help](#)

ACS Publications Title:

Mechanism of Formation of Au Vacancy Islands in Alkanethiol Monolayers on Au(111)

Logged in as:

Jungwoo Nah

Account #:

3000486771

Author: G. E. Poirier

Publication: Langmuir

Publisher: American Chemical Society

Date: Apr 1, 1997

Copyright © 1997, American Chemical Society

[LOGOUT](#)**PERMISSION/LICENSE IS GRANTED FOR YOUR ORDER AT NO CHARGE**

This type of permission/license, instead of the standard Terms & Conditions, is sent to you because no fee is being charged for your order. Please note the following:

- Permission is granted for your request in both print and electronic formats.
- If figures and/or tables were requested, they may be adapted or used in part.
- Please print this page for your records and send a copy of it to your publisher/graduate school.
- Appropriate credit for the requested material should be given as follows: "Reprinted (adapted) with permission from (COMPLETE REFERENCE CITATION). Copyright (YEAR) American Chemical Society." Insert appropriate information in place of the capitalized words.
- One-time permission is granted only for the use specified in your request. No additional uses are granted (such as derivative works or other editions). For any other uses, please submit a new request.

[BACK](#)[CLOSE WINDOW](#)